

Magnetism, Structure and Their Interactions

DISSERTATION

zur Erlangung des akademischen Grades

Doktor rerum naturalium
(Dr. rer. nat.)

vorgelegt
der Fakultät für Mathematik und Naturwissenschaften
der Technischen Universität Dresden

von

Wenxu Zhang

geb. am 26. 06. 1977 in Sichuan, P. R. China

TECHNISCHE UNIVERSITÄT DRESDEN

2007

1. Gutachter: Prof. Dr. Helmut Eschrig
2. Gutachter: Prof. Dr. Peter Fulde
2. Gutachter: Prof. Dr. Jürgen Hafner

Eingereicht am 14. Nov. 2007

Contents

1	Introduction	1
2	Theoretical Background	3
2.1	Electronic Hamiltonian in a solid	3
2.2	Density functional theory and the Kohn-Sham scheme	4
2.3	The Kohn-Sham equations	7
2.4	Basics of FPLO code	9
2.5	Model considerations	12
2.5.1	Free electron gas in Hartree Fock approximation	12
2.5.2	The Stoner model	13
2.5.3	An application in FCC iron	15
2.6	The band Jahn-Teller effect	16
2.6.1	A one dimensional case—the Peierls distortion	17
2.6.2	A two dimensional case—the square lattice model	18
3	Band Jahn-Teller effects in Rh₂MnGe	21
3.1	Introduction to Heusler alloys and related experiments	21
3.2	Calculation details	22
3.3	Main results of the calculations	23
3.3.1	The lattice constant and the magnetic moment of the cubic phase	23
3.3.2	Crystal structures at the ground state	24
3.3.3	Experimental evidences for the tetragonal phase at low temperature	28
3.3.4	An interpretation as the band Jahn-Teller effect	29
3.3.5	Relativistic effects	34
4	Magnetic transitions of AFe₂ under pressure	37
4.1	Introduction	37
4.2	Calculational parameters	40
4.3	Fixed spin moment schemes	41
4.4	Ground state properties of AFe ₂	41
4.4.1	Common features of the electronic structure	41
4.4.2	Specific electronic structures and magnetic moment behavior	47
4.4.3	The order of the magnetic transition under high pressure	49
4.5	Relationship between Invar behavior and magnetic transitions	53
4.6	Doping effects	56

5	Magnetic transitions in CoO under high pressure	61
5.1	Introduction	61
5.2	A brief introduction to LSDA+ U	64
5.3	A Category of insulators	65
5.4	Computational parameters	66
5.5	LSDA pictures	68
5.6	LSDA+ U pictures	70
5.6.1	Electronic structures of the ground state	70
5.6.2	Magnetic transitions in LSDA+ U	73
5.7	The reason for the magnetic transition	77
5.8	Discussions	78
6	Summary and Outlook	81
	Appendix	91
	Acknowledgment	93

List of Figures

2.1	Variant concepts in electronic structure calculations for solids . . .	10
2.2	Different energy contributions in the free electron model	13
2.3	Density of states for FCC iron at $a_0=3.60 \text{ \AA}$	15
2.4	Plot of $Y(m) = \frac{2\partial E_b}{m\partial m}$ versus the magnetic moment (m).	16
2.5	Atoms form a linear chain.	17
2.6	Band structure of the atoms in linear chain before and after the Peierls distortion	17
2.7	Atoms form a square lattice with a lattice constant a	19
2.8	A schematic illustration of dispersion of a p_z orbital.	19
3.1	The conventional unit cell of Rh_2MnGe in a cubic and a tetragonal lattice.	23
3.2	The contour plot of the energy with respect to the relative volume and c/a	25
3.3	Energy versus c/a ratios for the tetragonal structure.	26
3.4	The magnetic moment versus relative volume of different phases.	27
3.5	Partial DOS of the Mn-3d state.	27
3.6	The total magnetic moment and the magnetic moment of Mn versus the c/a ratio.	28
3.7	Diffraction pattern collected at different temperatures from $T = 20 \text{ K}$ to 340 K around $2\theta = 42^\circ$	29
3.8	Temperature dependence of the lattice parameters in the cubic and tetragonal phases.	30
3.9	The high symmetry points in the BCT Brillouin Zone.	30
3.10	Angular and magnetic quantum number resolved bands (majority spin channel) of the cubic phase.	31
3.11	Band structure of the elongated and compressed tetragonal structure.	32
3.12	Total DOS and DOS of Rh near the Fermi level for different c/a ratios.	33
3.13	Scalar-relativistic (sr) and fully relativistic (fr) band structure of the cubic phase at $V_0=105.85 \text{ \AA}^3$	34
4.1	The unit cell of the cubic Laves phase (C15).	40
4.2	DOS of AFe_2 ($A=\text{Y, Zr, Hf, and Lu}$) at the respective equilibrium volumes.	42
4.3	The band structure and DOS of the minority spin channel of ZrFe_2	43

4.4	The corner shared tetrahedrons of Fe and its Kagomé net in $\{111\}$ plane.	44
4.5	The “fat” band and PDOS of the minority state of Fe in ZrFe_2 . .	45
4.6	PDOS of Fe resolved into the irreducible representation (A_{1g} and $E_g^{1,2}$) of the point group D_{3d}	46
4.7	Schematic representation of the covalent bonding	47
4.8	Magnetic moment behavior of AFe_2	48
4.9	DOS evolution of ZrFe_2 under pressure	49
4.10	Qualitative illustration of first and the second order quantum phase transitions.	50
4.11	The FSM energies of ZrFe_2 at the lattice constant around 6.30 Å. .	51
4.12	The DOS of nonmagnetic state and ferromagnetic state at $a=6.30$ Å.	52
4.13	The FSM energy of YFe_2 at lattice constant around 6.00 Å. . .	53
4.14	The DOS of the nonmagnetic state and ferromagnetic state of YFe_2 at $a=5.98$ Å.	53
4.15	A schematic draw of the 2γ -model.	54
4.16	The FSM energy curves of ZrFe_2 near the HS-LS transition regions. .	55
4.17	The magnetic moments of $\text{Fe}^{I, II}$ and Zr versus the atomic concentration of Fe.	58
4.18	The total DOS and the partial DOS of the doped compounds with composition $\text{Zr}_{0.9}\text{Fe}_{2.1}$ at the lattice constant $a = 6.825$ Å. .	58
4.19	The measured and calculated magnetic moments per Fe vs. the atomic concentration of Zr	59
5.1	Phase diagram of CoO under pressure summarized from experiments.	62
5.2	A schematic illustration of energy levels of two different insulators .	66
5.3	The unit cell of CoO in the calculation	67
5.4	The LSDA density of 3d states of the Co and 2p states of O. . .	68
5.5	LSDA model DOS of the 3d states of Co in CoO	69
5.6	Magnetic moment of Co and total energy versus the relative volume.	70
5.7	The results from the LSDA+ U with different value of U	71
5.8	The Co-3d and O-2p DOS at the equilibrium lattice constant with $U=5$ eV.	72
5.9	The LSDA+ U model DOS (a) and its variation under pressure (b). .	74
5.10	The LSDA+ U PDOS at a volume of 90 a.u./f.u., about 70% of the theoretical equilibrium volume.	74
5.11	The Co-3d PDOS at the equilibrium lattice constant resolved into different angular quantum number with respect to the rhombohedral lattice.	75
5.12	The Co-3d PDOS for the two possible low spin solutions.	76
5.13	The PDOS after the electron with e_g symmetry flips its spin decomposed according to the cubic symmetry.	76
5.14	The LSDA+ U model DOS after the magnetic transition (LS-II). .	77
5.15	The total energy and the magnetic moment (inset) versus the relative volume	78

5.16	The evolution of the center of gravity of the unoccupied E_g state (diamonds) and T_{2g} state (circles) under relative volumes with respect to $V_0=129.4$ a.u./f.u..	79
5.17	The enthalpy of CoO under pressure with different values of U	80

List of Tables

3.1	Comparison of the calculated lattice constant and magnetic moments of the cubic structure with experimental results and previous calculations of the cubic Rh_2MnGe compound. The chosen method and parameterization of the xc-potential is given in parenthesis.	23
4.1	The experimental values of the lattice constant (a), magnetic moment (m_s), and Curie temperature (T_c) of AFe_2 ($\text{A}=\text{Y}, \text{Zr}, \text{Hf}$, and Lu) compounds.	38
4.2	The calculated lattice constants a_{FM} in FM state and a_{NM} in NM state, total spin magnetic moments at both theoretical (m_0) and experimental (m_{exp}) lattice constants of the four compounds.	43
4.3	The spontaneous volume magnetostriction from our LSDA calculations (ω_s) and experiments (ω_s^{exp}).	56
4.4	The experimental (a_0^{exp}) and theoretical lattice constants (a_0^{LDA}) of $\text{Zr}_x\text{Fe}_{100-x}$. The experimental values are taken at room temperature.	57
5.1	Ground state properties of CoO obtained by LSDA+ U calculations with different values of U . Experimental data are given in the last row.	72

Abbreviation

a.u.	a tom i c u nits
ASA	a tom i c s phere a pproximation
ASW	a ugmented s pherical w aves
BZ	B rillouin z one
CPA	c oherent p otential a pproximation
DFT	d ensity f unctional t heory
DOS	d ensity o f s tates
EOS	e quation o f s tates
FPLO	f ull p otential nonorthogonal l ocal o rbital minimum basis band structure scheme
FSM	f ixed s pin m oment
GGA	g eneralized g radient a pproximation
HS	h igh s pin
IBZ	i rreducible B rillouin z one
IR	i rreducible r epresentation
LCAO	l inear combination of a tom i c o rbital s
LDA	l ocal d ensity a pproximation
LMTO	l inearized m uffin-tin o rbital s method
LS	l ow s pin
LSDA	l ocal s pin d ensity a pproximation
PDOS	p artial d ensity o f s tates
SIC	s elf i nteraction c orrection

Chapter 1

Introduction

Magnetism and structures are two main topics in solid state physics. These two properties are developed individually but they also interact strongly. Structural transition leads to changes of magnetism by providing different atomic environment (e.g. different coordination of atoms and different bond lengths). On the other hand, changes of magnetic moment unavoidably introduce volume variations of samples (known as volume magnetostriction). This interaction is of course technically important. One example is Invar effects, which are believed to result from the interplay between magnetism and structures, where the increase of volume due to thermal expansions is (partly) compensated by the demagnetization which causes decrease of the volume. Thus the elastic properties and/or the thermal expansion coefficient in a certain temperature range are extremely small (invariant volumes), about $10^{-6}/\text{K}$ in $\text{Fe}_{65}\text{Ni}_{35}$. Behavior of ferromagnetic shape memory alloys (FSMA) yields examples for the interplay between magnetism and the structural phase transition (the martensitic phase transition), where the shape changes due to the movement of twin boundaries is driven by the rotation of the magnetic moment.

In order to understand the structural trend and magnetism of a solid, a number of models have been proposed, such as the Stoner model to explain the itinerant magnetism, the band Jahn-Teller effect to explain some structural phase transitions, spin and orbital ordering, *etc.* These models provide us the physics underlying different phenomena. Tight binding approximations in electronic structure calculation and rigid band model provide some qualitative and semi-quantitative information about structures, magnetism, and their interactions. At the same time, understanding these phenomena in an *ab initio* way is mostly desirable.

Density functional theory (DFT), which was originally invented and developed by Kohn, Hohenberg, and Sham in the middle of the sixties, provides a modern tool to study the ground state properties of atoms, molecules, and solids. It is based on exact theorems, in particular, the Hohenberg-Kohn theorems. Kohn and Sham, later on, put this general theorem into a practical way where the problem can be solved by a single particle-like Hamiltonian with an approximated effective potential. The electronic structure calculations provide a quantitative way to discuss the phase stability at temperature $T = 0$, and are even extendable to $T \neq 0$ with certain model assumptions. They also provide the microscopic explanation of phase transitions. Bonding characters, energy

dispersions or topology of Fermi surfaces *etc.* all can play a role in the different phase transitions. Magnetic properties are natural outputs of the calculations. In the non-relativistic case, the magnetic moment is the difference between the populations of the spin up and spin down states. Electronic structure calculations also provide quantitative justification of the model considerations. For example, in the Stoner model, the density of states and the Stoner parameter are available by DFT calculations. Thus the itinerant magnetism can be discussed in a more quantitative way. It has been shown that the local spin density approximation (LSDA) and its extension the general gradient approximation (GGA) are quite successful in understanding itinerant magnetism and structure trends in metals and intermetallic compounds. The strong electron-electron interaction seems to be problematic when it is treated in a mean field way. For example, some transition metal oxides with partially filled *d* orbitals are predicted to be metallic under this local approximation, but are Mott insulators in reality. This strongly correlated state is better treated by a combination of LSDA and local Coulombic repulsion, the so-called LSDA+U method. This approach provides us a powerful tool to treat the strongly correlated systems.

On the other hand, developments of high pressure techniques and magnetic analyzing methods lead to discoveries of many new phenomena. For example, it was found that the critical temperature of superconductivity may be increased under pressure, which might be due to the enhancement of electron phonon coupling under pressure. Pressure will surely influence magnetism. As early as in 1936, Néel gave an estimation of the direct exchange interaction energy between localized moments located on two neighboring atoms with overlapping orbitals. This was the first model to show the large dependence of the molecular field on the inter-atomic distance. Taking the homogenous electron gas, which is the basis of LSDA, as another example, the spin polarized state only exists in a narrow electron density range, the electron density parameter r_s ranging between 75 and 100 Bohr radii. Experiments under pressure provide a unique tool to characterize materials. Modern experiments can reach hydrostatic pressure beyond 200 GPa. The pressure changes at least the inter-atomic interaction. The itinerancy of the electrons will be changed accordingly. This is generally included in the Stoner's model. The improving experimental facilities push us to extend our theoretical work to high pressures, to understand, and predict new phenomena.

In this thesis, magnetic and structural transitions of three categories of compounds are investigated by DFT calculations under the LSDA. The thesis is organized as follows: In Chapter 2, I present a brief introduction to the DFT and its LSDA. Some model considerations of magnetism and structural transitions are presented, including the Stoner model, the Peierls distortion, and the band Jahn-Teller effect in two dimensions. In Chapter 3, two different (tetragonal and cubic) structures of Rh_2MnGe are investigated and the band Jahn-Teller effect in this compound is discussed. Four cubic Laves phase compounds (YFe_2 , ZrFe_2 , HfFe_2 , and LuFe_2) are investigated in Chapter 4. The interplay between magnetism and pressures is emphasized. The last material investigated in this thesis is CoO in Chapter 5, where the pressure induced magnetic transition is explained by the competition between the ligand field splitting and the exchange energy. In the last chapter I give a summary and outlook of the present study.

Chapter 2

Theoretical Background

2.1 Electronic Hamiltonian in a solid [1]

We suppose that properties of a solid can be revealed by finding a wave function $\Phi = \Phi(\mathbf{R}, \mathbf{r})$ satisfying the Schrödinger equation $\hat{\mathcal{H}}\Phi = E\Phi$ with the Hamiltonian under the non-relativistic approximation defined as:

$$\hat{\mathcal{H}} = \hat{\mathcal{H}}_e + \hat{\mathcal{H}}_{ion} + \hat{\mathcal{H}}_{el-ion} + \hat{\mathcal{H}}_{ex}, \quad (2.1)$$

where

$$\begin{aligned} \hat{\mathcal{H}}_e &= \sum_k \frac{\hat{p}_k^2}{2m} + \frac{1}{8\pi\epsilon_0} \sum_{kk'}' \frac{e^2}{|\mathbf{r}_k - \mathbf{r}_{k'}|}, \\ \hat{\mathcal{H}}_{ion} &= \sum_i \frac{\hat{P}_i^2}{2M_i} + \frac{1}{2} \sum_{ii'}' \hat{V}_{ion}(\mathbf{R}_i - \mathbf{R}_{i'}) \\ &= \sum_i \frac{\hat{P}_i^2}{2M_i} + \frac{1}{8\pi\epsilon_0} \sum_{i \neq i'}' \frac{Z_i Z_{i'}}{|\mathbf{R}_i - \mathbf{R}_{i'}|} \\ \hat{\mathcal{H}}_{el-ion} &= \sum_{k,i} \hat{V}_{el-ion}(\mathbf{r}_k, \mathbf{R}_i) = -\frac{1}{4\pi\epsilon_0} \sum_{k,i} \frac{Z_i |e|}{|\mathbf{r}_k - \mathbf{R}_i|}, \end{aligned} \quad (2.2)$$

and $\hat{\mathcal{H}}_{ex}$ is due to external fields. The $\hat{\mathcal{H}}_e$, $\hat{\mathcal{H}}_{ion}$, and $\hat{\mathcal{H}}_{el-ion}$ are the electron, ion, and the electron-ion interaction Hamiltonian respectively. The variables are defined as:

- ϵ_0 , the dielectric constant in vacuum,
- M_i , the static mass of ion i , and m , the static mass of an electron,
- \hat{P}_i and \hat{p}_k , the momentum operator of ion i and electron k , respectively,
- e , the electron charge, and Z_i , the nuclear charge, respectively,
- \mathbf{R}_i , the position of ion i , and \mathbf{r}_k , the position of electron k ,
- and \hat{V}_{ion} and \hat{V}_{el-ion} , the ion-ion interaction and the electron-ion interaction, respectively.

Of course, as Dirac had commented, “The general theory of quantum mechanics is now almost complete. The underlying physical laws necessary for the mathematical theory of a large part of physics and all of chemistry are thus completely known”, but this equation is too complicate to be solved. Consider a typical solid, there are about $\sim 10^{23}$ atoms and the related number of electrons. The complexity of this problem increase exponentially with the number of the particles, and soon beyond the capability of storage and computing of any imaginable computers except for a very small number of particles (less than several tens). Simplifications should be made in order that the problem is tractable. The first approximation is the Born-Oppenheimer approximation (or adiabatic approximation). Considering the large difference of the rest mass between electrons and ions ($m/M \leq 1/1836$), we can assume that the electrons respond adiabatically to a change in positions of the ions which respond only slowly to a change in the electron configurations. In this way, the motions of the electrons and ions are decoupled. As far as we are only concerned about the motion of the electrons, it is only the instantaneous configuration ($\{\mathbf{R}_i\}$) of the ions being of interest. The motions of the electrons are governed by the following Hamiltonian \hat{H}_e^{BOA} :

$$\hat{\mathcal{H}}_e^{BOA} = \sum_k \frac{\hat{p}_k^2}{2m} + \frac{1}{8\pi\epsilon_0} \sum_{kk'}' \frac{e^2}{|\mathbf{r}_k - \mathbf{r}_{k'}|} + \sum_k \hat{V}_{el-ion}(\mathbf{r}_k, \mathbf{R}_i) + const.(\mathbf{R}_i). \quad (2.3)$$

where $const.(\mathbf{R}_i) = \sum_{i,j} Z_i Z_j / 8\pi\epsilon_0 |\mathbf{R}_i - \mathbf{R}_j|$ is needed in case of the thermodynamic limit. Thus, we can consider the electronic structure with respect to the configurations of the ions. Once we have obtained the energy $E_e(\{\mathbf{R}_i\})$ of the electronic system by solving the eigen equation:

$$\hat{\mathcal{H}}_e^{BOA} \Psi(\mathbf{r}) = E_e(\{\mathbf{R}_i\}) \Psi(\mathbf{r}), \quad (2.4)$$

we have the Hamiltonian for the ions:

$$\hat{\mathcal{H}}_{ion}^{BOA} = \sum_i \frac{\hat{P}_i^2}{2M_i} + \frac{1}{2} \sum_{i,i'}' \hat{V}_{ion}(\mathbf{R}_i - \mathbf{R}_{i'}) + E_e(\{\mathbf{R}_j\}), \quad (2.5)$$

which is decoupled from the electron coordinates.

Now we have the decoupled electronic and ionic system which can be solved separately in this adiabatic approximation, but the dimension of the system is still too large. We still have the huge number of the electrons and the ions.

2.2 The density functional theory and the Kohn-Sham scheme [2]

We have the electron wave function $\Psi(x_1, x_2, \dots, x_N)$ where $x_i = (\mathbf{r}_i, s_i)$ standing for the collection of the position \mathbf{r}_i and the spin s_i of electron i , which depends on $3N \times 2 = 6N$ coordinates. This is untractable for large electron numbers N . A plausible step to solve the problem for the ground state was realized by Hohenberg and Kohn [3], who converted the problem of searching for the electron wave function into the search for a scalar function, the electron density $n(\mathbf{r})$ in a three dimensional real space. Here we treat the extension to spin densities $n_{ss'}(\mathbf{r})$

Consider the electronic Hamiltonian in the Schrödinger representation ¹,

$$\hat{\mathcal{H}}_e[v, M] = -\frac{1}{2} \sum_{i=1}^M \nabla_i^2 + \sum_{i=1}^M v_{s_i s'_i}(\mathbf{r}_i) + \frac{1}{2} \sum_{i \neq j}^M w(|\mathbf{r}_i - \mathbf{r}_j|) \quad (2.6)$$

for any external spin dependent potential $v_{s_i s'_i}$ and integer particle number M . The function $w(|\mathbf{r}_i - \mathbf{r}_j|) = \frac{1}{|\mathbf{r}_i - \mathbf{r}_j|}$ is the electron-electron Coulombic interaction. As we are dealing with solids, we introduce periodical boundary conditions which replace the infinite position space \mathcal{R}^3 of electron coordinates by a torus \mathcal{T}^3 with a finite measure.

Defining two sets:

$$\mathcal{V}_N = \{v | v \in \mathbf{L}^p \text{ for some } p\text{'s}, \hat{\mathcal{H}}[v] \text{ has a ground state}\} \quad (2.7)$$

and

$$\mathcal{A}_N = \{n(x) | n \text{ comes from an } N\text{-particle ground state}\}, \quad (2.8)$$

where $v \in \mathbf{L}^p$ means that $\|v\|_p = [\int dx |v(x)|^p]^{1/p}$, $1 \leq p < \infty$ is finite. The basic Hohenberg and Kohn theorem reads:

Theorem 1 (H-K Theorem) $v(x) \bmod(\text{const.}) \in \mathcal{V}_N$ is a unique function of the ground state density $n(x)$.

In the original paper by Hohenberg and Kohn [3], the \mathcal{V}_N is confined to a non-degenerated ground state, and $n(x)$ also belongs to a non-degenerated ground state, but degeneracy of the ground state is more common in electronic systems. The theorem was generalized by the following argument by Lieb [4] where the non-degeneracy is not required.

We define the density operator which admits ensemble states as:

$$\hat{\gamma} = \sum_K |\Psi_K\rangle g_K \langle \Psi_K|, \quad (2.9)$$

where $g_K \geq 0$ and $\sum_K g_K = 1$ and $|\Psi_K\rangle$ is for some pure states, which may be expanded into a fixed orthonormal set of eigenstates of particle number operator \hat{N} : $\hat{N}|\phi_K^M\rangle = |\phi_K^M\rangle M$,

$$|\Psi_K\rangle = \sum_M |\phi_K^M\rangle C_M^K, \quad \sum_M |C_M^K|^2 = 1. \quad (2.10)$$

The expectation value of particle density

$$n_{ss'}(\mathbf{r}) = \text{tr}(\hat{n}\hat{\gamma}) = \sum_{K,M} p_M^K n_{K,ss'}^M(\mathbf{r}), \quad (2.11)$$

where $p_M^K \stackrel{\text{def}}{=} g_K |C_M^K|^2$ and $n_{K,ss'}^M(\mathbf{r}) = \langle \mathbf{r}, s | \phi_K^M \rangle \langle \phi_K^M | \mathbf{r}, s' \rangle$. The total particle number reads

$$\begin{aligned} N &= \text{tr}(\hat{N}\hat{\gamma}) = \sum_s \int n_{ss}(\mathbf{r}) d\mathbf{r} \\ &= \sum_{K,M} p_M^K \sum_s \int n_{K,ss}^M(\mathbf{r}) d\mathbf{r} \\ &= \sum_{K,M} p_M^K M. \end{aligned} \quad (2.12)$$

¹from now on, atomic units (a.u.) will be used, which means we put $e = m = \hbar = 1$ and $\epsilon_0 = \frac{1}{4\pi}$. The superscript *BOA* will be omitted.

The total energy is

$$\text{tr}(\hat{H}\hat{\gamma}) = \sum_{K,M} p_M^K \langle \phi_K^M | \hat{H}[v, M] | \phi_K^M \rangle, \quad (2.13)$$

where $p_M^K \geq 0$, $\sum_{K,M} p_M^K = 1$. Now, the ground state energy (E) as a functional of the external potential v , and a function of real particle number N can be defined as:

$$\begin{aligned} E[v, N] &\stackrel{\text{def}}{=} \inf_{\hat{\gamma}} \{ \text{tr}(\hat{H}\hat{\gamma}) | \text{tr}(\hat{N}\hat{\gamma}) = N \} \\ &= \inf_{p_M^K} \{ \sum_{K,M} p_M^K \langle \phi_K^M | \hat{H}[v, M] | \phi_K^M \rangle | \sum_{K,M} p_M^K M = N \}, \end{aligned} \quad (2.14)$$

where \hat{N} is the particle number operator, $\hat{N}|\phi_K^M\rangle = |\phi_K^M\rangle M$. It can be shown that $E[v, N]$ has the following properties²:

1. $E[v + \text{const}, N] = E[v] + N \cdot \text{const}$ (gauge invariance),
2. for fixed v , $E[v, N]$ is convex in N , and
3. for fixed N , $E[v, N]$ is concave in v .

Starting with the convexity of $E[v, N]$ in N , a Legendre transform $\tilde{G}[v, \mu]$ is defined with a pair of transformations:

$$\begin{aligned} \tilde{G}[v, \mu] &= \sup_N \{ \mu N - E[v, N] \}, \\ E[v, N] &= \sup_{\mu} \{ N\mu - \tilde{G}[v, \mu] \}. \end{aligned} \quad (2.15)$$

Because of the above gauge invariance (Property 1) of $E[v, N]$,

$$\tilde{G}[v, \mu] = \tilde{G}[v - \mu, 0] \stackrel{\text{def}}{=} G[v']. \quad (2.16)$$

Then the duality relations of Equ. (2.15) are simplified to

$$\begin{aligned} G[v] &= - \inf_N E[v, N], \\ E[v, N] &= \sup_{\mu} \{ N\mu - G[v - \mu] \}. \end{aligned} \quad (2.17)$$

Since $G[v]$ is convex in v , it can be back and forth Legendre transformed. If we introduce $-n$ as a dual variable to v , then

$$\begin{aligned} H[n] &= \sup_v \{ (-n|v) - G[v] \} \\ G[v] &= \sup_n \{ (v|n) - H[n] \} = - \inf_n \{ H[n] + (v|n) \} \end{aligned} \quad (2.18)$$

Insert $G[v]$ of Equ. (2.17) into $H[n]$, we have

$$\begin{aligned} H[n] &= \sup_v \{ (-n|v) + \inf_N E[v, N] \} \\ &\leq \inf_N \sup_v \{ E[v, N] - (n|v) \} \\ &= \inf_N F[n, N], \end{aligned} \quad (2.19)$$

²In this section, we just present conclusions without mathematical proofs in order to outline the logical base of this theory.

where we define (first introduced by Lieb [4])

$$F[n, N] = \sup_v \{E[v, N] - (n|v)\} \quad (2.20)$$

as a density functional. Then the inverse Legendre transformation to Equ. (2.20) leads to

$$\begin{aligned} E[v, N] &= \sup_{\mu} \{N\mu + \inf_n \{H[n] + (v - \mu|n)\}\} \\ &= \inf_n \{H[n] + (v|n)|(1|n) = N\}. \end{aligned} \quad (2.21)$$

In Lieb's definition Equ. (2.20) of the density functional, the domain of n is $\mathcal{X} = \mathcal{L}^3(\mathbf{T}^3)$, and the dual variable v is limited to $\mathcal{X}^* = \mathcal{L}^{3/2}(\mathbf{T}^3)$, where \mathcal{X} and \mathcal{X}^* are reflexive ($\mathcal{X}^{**} = \mathcal{X}$).

In the original theorem by Hohnberg and Kohn, the functional $F[n]$ is defined by

$$F_{HK}[n] = E[v[n]] - \int dx v[n]n, \quad n \in \mathcal{A}_N. \quad (2.22)$$

This raises the problem of v -representability (VR).

2.3 The Kohn-Sham equations

Since $H[n]$ as a Legendre transformation is lower semicontinuous on \mathcal{X} , it has a non-empty subdifferential for $n \in \mathcal{X}$. Moreover, a convex function on a normalized space has a derivative, if and only if the subdifferential consists of a unique element of the dual space. Hence, if $v - \mu \in \mathcal{X}^*$ is uniquely defined in the theory for some given $n \in \mathcal{X}$ for which $H[n]$ is finite, then $H[n]$ has a functional derivative equal to $\mu - v$, that is

$$-\frac{\delta H}{\delta n} = v - \mu, \quad (2.23)$$

for non-integer $N = (n|1)$. For integer N , the derivative may jump by a finite value, constant in \mathbf{r} -space.

We put

$$H[n] = K[n] + L[n], \quad (2.24)$$

where

$$K[n] = \min_{\phi_i, n_i} \{k[\phi_i, n_i] | \sum_i \phi_i n_i \phi_i^* = n, 0 \leq n_i \leq 1 \langle \phi_i | \phi_j \rangle = \delta_{ij}\} \quad (2.25)$$

is the orbital dependent functional, and

$$L[n] = \int d^3 \mathbf{r} n(\mathbf{r}) l[n_{ss'}(r), \nabla n_{ss'}(r)], \quad (2.26)$$

is the explicit density functional, where ϕ_i are the Kohn-Sham orbitals with an occupation number n_i .

With a suitable chosen orbital functional k and function l , one arrives at the Kohn-Sham equation

$$(\hat{k} + v + v_L)\phi_i = \phi_i \epsilon_i \quad (2.27)$$

with

$$\hat{k} : \frac{\delta k}{\delta \phi_i^*} = \hat{k} \phi_i n_i, \hat{k} \text{ Hermitian}, \quad (2.28)$$

and the local Kohn-Sham potential

$$v_L = \frac{\delta L}{\delta n}, \quad (2.29)$$

where ϵ_i is the energy of the Kohn-Sham orbital ϕ_i . Especially if

$$K[n] = \begin{cases} T_{DM}[n] & \text{for } n \in X, n(x) \geq 0 \\ +\infty & \text{elsewhere} \end{cases} \quad (2.30)$$

$$L[n] = \sum_{ss'} \int (v_{ss'}^H + v_{ss'}^{xc} + v_{ss'}) n_{ss'} dr,$$

where $T_{DM}[n]$ is the kinetic energy functional of noninteracting electrons:

$$T_{DM}[n] \stackrel{def}{=} \inf_{\gamma} \{tr(\hat{T}\gamma) | \gamma \mapsto n\}$$

$$= \min_{\phi_i, n_i} \left\{ \sum_i n_i \int dx \phi_i^* \left(-\frac{\nabla^2}{2}\right) \phi_i \mid \sum_i n_i |\phi_i|^2 = n, 0 \leq n_i \leq 1, \langle \phi_i | \phi_j \rangle = \delta_{ij} \right\}, \quad (2.31)$$

$v_{ss'}^H$ is the Hartree potential: $v_{ss'}^H(\mathbf{r}) = \int d^3\mathbf{r}' n_{ss'}(\mathbf{r}') w(|\mathbf{r} - \mathbf{r}'|)$, $v_{ss'}^{xc}$ is the exchange correlation potential and $v_{ss'}$ is the external potential. Then one arrives at the Kohn-Sham equation³:

$$\left(-\frac{\nabla^2}{2} + v_s^{eff}\right) \phi_i = \phi_i \epsilon_i, \quad (2.32)$$

$$v_s^{eff} = v + v^H + v_s^{xc}.$$

The v_s^{xc} is defined as:

$$v_s^{xc}(\mathbf{r}) \stackrel{def}{=} \frac{\delta}{\delta n_s(\mathbf{r})} E_{xc}[n(\mathbf{r})]. \quad (2.33)$$

The simplest successful approximation to this functional is the local spin density approximation (LSDA) [5], where the functional dependence is taken to be the same as in homogenous electron liquid:

$$E_{xc}^{LDA}[n_{+,-}(\mathbf{r})] = \int \epsilon_{xc}^{hom}(n_{+,-}(\mathbf{r})) n(\mathbf{r}) d\mathbf{r}. \quad (2.34)$$

This spin dependent xc-functional can be obtained by fitting the results from quantum Monte Carlo simulations of the homogenous electron gas [6]. The presently most precise fit is obtained by Perdew and Wang [7]. In this fitting the correlation energy has the form:

$$\epsilon_c(r_s, \zeta) = \epsilon_c(r_s, 0) + \alpha_c(r_s) \frac{f(\zeta)}{f''(0)} (1 - \zeta^4) + [\epsilon_c(r_s, 1) - \epsilon_c(r_s, 0)] f(\zeta) \zeta^4, \quad (2.35)$$

$$f(\zeta) = \frac{[(1 + \zeta)^{4/3} + (1 - \zeta)^{4/3} - 2]}{2^{4/3} - 2},$$

³Here, we deal with the collinear spin polarization which means that we can find a global unitary transformation so that the 2×2 density matrix ($n_{ss'}$) and potential matrix ($v_{ss'}$) can be simultaneously diagonalized into n_s and v_s , respectively.

and the exchange contribution is

$$\epsilon_x(r_s, \zeta) = -\frac{3}{4\pi r_s} \left[\frac{9\pi}{4} \right]^{1/3} [(1 + \zeta)^{4/3} + (1 - \zeta)^{4/3}] / 2, \quad (2.36)$$

where $\zeta = (n_+ - n_-) / (n_+ + n_-)$ is the relative spin polarization, $r_s = [3/4\pi(n_+ + n_-)]^{1/3}$ is the density parameter, and $\alpha_c(r_s) = \partial^2 \epsilon_c(r_s, \zeta = 0) / \partial \zeta^2$ is the spin stiffness. This version of exchange correlation will be used in all of our LSDA calculations in this thesis.

2.4 Basics of the Full Potential Local Orbital band structure code (FPLO)

If we choose the periodic boundary conditions for the wave function and consider an infinite crystal with periodically arranged atoms, the electrons feel a periodic potential $V(\mathbf{r}) = V(\mathbf{r} + \mathbf{R})$ where \mathbf{R} is a Bravais lattice vector. This means that the Hamiltonian of the electrons has a translational symmetry. The electron wave function in the crystal has the following property:

Theorem 2 (Bloch Theorem) *The eigenstates $\Psi_{n\mathbf{k}}(\mathbf{r})$ of the one-electron Hamiltonian $\hat{H} = -\nabla^2/2 + V(\mathbf{r})$, where $V(\mathbf{r} + \mathbf{R}) = V(\mathbf{r})$ for all \mathbf{R} in a Bravais lattice, can be chosen to have the form of a plane wave times a function with the periodicity of the Bravais lattice:*

$$\Psi_{n\mathbf{k}}(\mathbf{r}) = e^{i\mathbf{k} \cdot \mathbf{r}} u_{n\mathbf{k}}(\mathbf{r}), \quad (2.37)$$

where

$$u_{n\mathbf{k}}(\mathbf{r} + \mathbf{R}) = u_{n\mathbf{k}}(\mathbf{r}). \quad (2.38)$$

Because of the boundary condition (BC), let $\mathbf{R} = \sum_i \mathbf{a}_i L_i$,

$$\Psi_{n\mathbf{k}}(\mathbf{r} + \sum_i \mathbf{a}_i L_i) = \Psi_{n\mathbf{k}}(\mathbf{r}), \quad (2.39)$$

where \mathbf{a}_i is the i -th basis vector of the Bravais lattice and L_i is the number of the cells along \mathbf{a}_i . The allowed \mathbf{k} -points are determined by:

$$\mathbf{k} = \sum_i \left(\frac{2\pi m_i}{L_i} \bmod 2\pi \right) \mathbf{k}_i^0 \quad (2.40)$$

where $m_i \in \mathbb{Z}$, the set of integers, $0 \leq m_i < L_i$ and \mathbf{k}_i^0 is the basis vector in the reciprocal space, satisfying $\mathbf{k}_i^0 \cdot \mathbf{a}_j = 2\pi \delta_{ij}$.

By this periodic BC, we actually convert our problem domain of \mathcal{R}^3 with infinite measure to a torus \mathcal{T}^3 with finite measure. This BC simplifies our treatment of the Coulombic system. For sufficiently large L_i 's, the physical properties are not altered by this BC. We can use the mathematically closed DFT introduced before to treat the electronic structure in the crystal.

In order to solve the Kohn-Sham equations, further approximations in the DFT calculations must be made. The different parts of this set of self-consistent equations can be approximated in different ways. These different ways are summarized in a diagram as in Figure 2.1. Most of the electronic structure calculations in this thesis are performed with the Full Potential Local Orbital minimum basis band structure code *FPLO-5* [8]. This code has the following features:

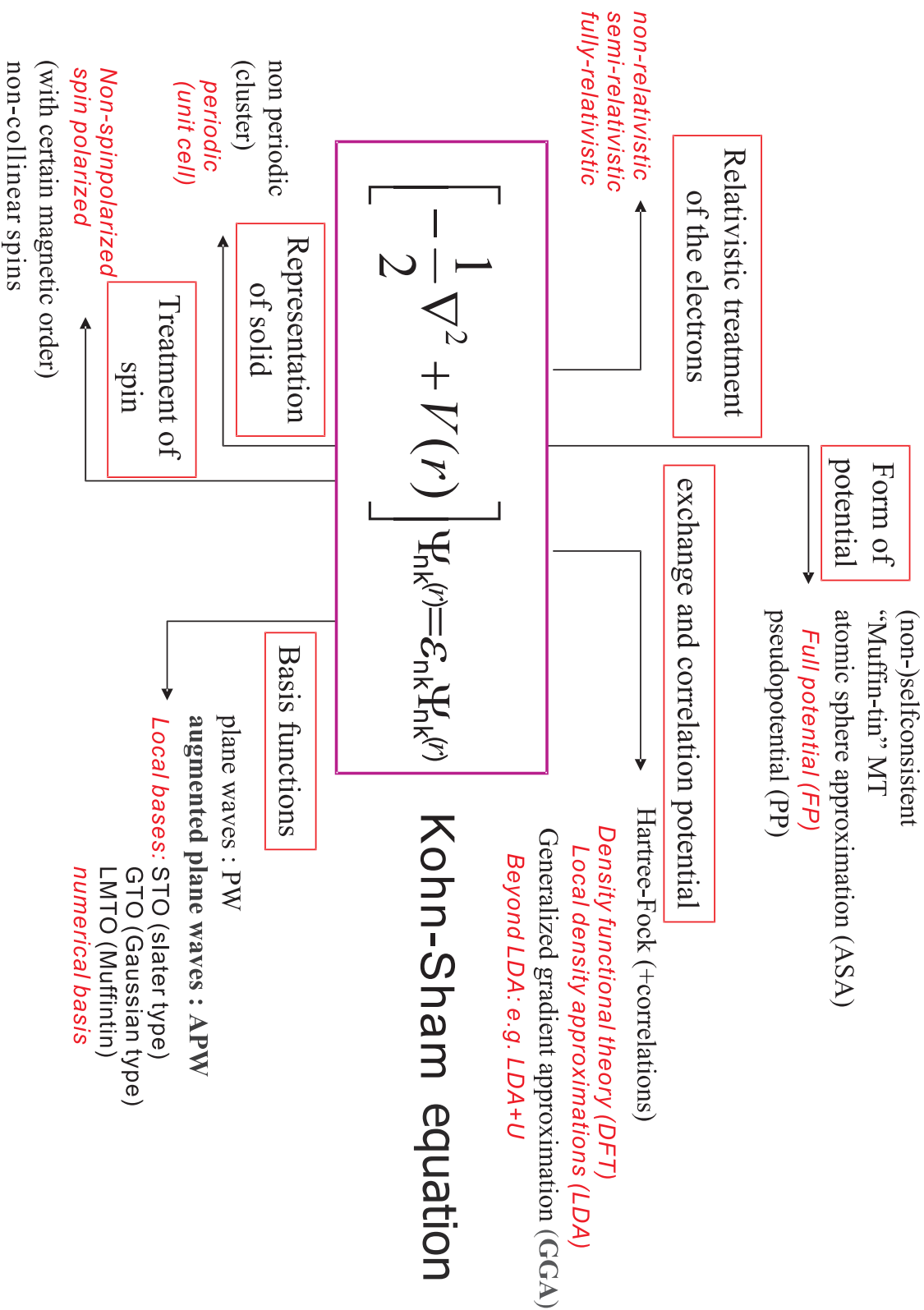


Figure 2.1: Variant concepts in electronic structure calculations for solids. The features in italics are currently implemented in FPLO-5.

- It is a full potential code, which means, no shape approximation of the potential is applied. This removes the previous inaccuracy in the results introduced by ASA, or MT approximations to the potential.
- It is an optimized local basis code⁴. Numerical atomic basis states are used as the basis to expand the Kohn-Sham orbitals. The relatively small basis set accelerates the calculation. The completeness of the relatively small number of basis (frequently the minimum basis) is improved by optimizing the basis.
- It is an all electron code, which does not use a pseudopotential.

The basic idea is as follows: The Bloch wave function indexed by (n, \mathbf{k}) is expressed by a superposition of nonorthogonal local orbitals $\langle \mathbf{r} | \mathbf{R}, \mathbf{s}L \rangle = \phi_{\mathbf{s}L}(\mathbf{r} - \mathbf{R} - \mathbf{s})$ centered at position $\mathbf{R} + \mathbf{s}$ with quantum number L ($L = (\nu, l, m)$, ν : principle quantum numbers, l : angular quantum numbers, m : magnetic quantum numbers):

$$\Psi_{\mathbf{k}n}(\mathbf{r}) = \sum_{\mathbf{R}\mathbf{s}L} \phi_{\mathbf{s}L}(\mathbf{r} - \mathbf{R} - \mathbf{s}) C_{L\mathbf{s},\mathbf{k}n} e^{i\mathbf{k} \cdot (\mathbf{R} + \mathbf{s})}. \quad (2.41)$$

Putting this trial function into the Kohn-Sham equation, multiplying $\langle 0s'L' | \mathbf{r} \rangle$ from the left on both sides and integrating, we obtain the secular equation:

$$\begin{aligned} HC &= SC\epsilon \\ \text{with} \\ H_{\mathbf{s}'L',\mathbf{s}L} &= \sum_{\mathbf{R}} \langle 0\mathbf{s}'L' | \hat{H} | \mathbf{R}\mathbf{s}L \rangle e^{i\mathbf{k} \cdot (\mathbf{R} + \mathbf{s} - \mathbf{s}')}, \\ S_{\mathbf{s}'L',\mathbf{s}L} &= \sum_{\mathbf{R}} \langle 0\mathbf{s}'L' | \mathbf{R}\mathbf{s}L \rangle e^{i\mathbf{k} \cdot (\mathbf{R} + \mathbf{s} - \mathbf{s}')}. \end{aligned} \quad (2.42)$$

The density ($n_s(\mathbf{r})$) obtained as a double lattice sum is reexpressed as a single lattice sum:

$$n(\mathbf{r}) = \sum_{\mathbf{k},n}^{occ.} \Psi_{\mathbf{k}n}^*(\mathbf{r}) \Psi_{\mathbf{k}n}(\mathbf{r}) = \sum_{\mathbf{R}\mathbf{s}} n_{\mathbf{s}}(\mathbf{r} - \mathbf{R} - \mathbf{s}) \quad (2.43)$$

and the potential ($v(\mathbf{r})$) is calculated under the LSDA and expressed into local contributions ($v_s(\mathbf{r})$):

$$v(\mathbf{r}) = \sum_{\mathbf{R}\mathbf{s}} v_{\mathbf{s}}(\mathbf{r} - \mathbf{R} - \mathbf{s}) \quad (2.44)$$

The exchange correlation potential is again reexpressed as a lattice sum in a similar way by a partition of unity on the lattice. trick is introducing a partition function The potential re-enters the Kohn-Sham equations until the self-consistency is realized.

In this thesis, the notation of the basis in the calculations are like, for example:

$$Fe : 3sp \quad / \quad 3d(4sp) \quad + \quad 4d$$

They are organized as:

$$Element : \quad semi - core \quad / \quad valence \quad + \quad polarization \ states$$

⁴The present state of the art is that this optimization is done before calculations. It is implemented in the new generation of FPLO.

The notation indicates the characters of the used basis orbitals above the core. For details see <http://www.fplo.de>.

2.5 Model considerations

It has long been recognized that magnetism and structures (the volume as well as the crystal symmetry) are related. This can be revealed by the following model considerations.

2.5.1 Free electron gas in Hartree Fock approximation

Considering free electron gas in a finite volume V , the states are described by plane waves with wave vector \mathbf{k} :

$$\Psi_{\mathbf{k}}^s(\mathbf{r}) = \left(\frac{1}{\sqrt{V}}e^{i\mathbf{k}\cdot\mathbf{r}}\right)\chi_s, \quad (2.45)$$

where χ_s is the spin eigenfunction for spin s . Because of the isotropic nature of the system, we use k instead of \mathbf{k} from now on. Using these states to form the Slater determinant and requiring double occupation of states with $k \leq k_F$, where k_F is the Fermi wave vector, we arrive at the Hartree-Fock equation for free electrons, where the energy dispersion relation [9] is:

$$\epsilon(k) = \frac{k^2}{2} - \frac{2}{\pi}k_F F\left(\frac{k}{k_F}\right) \quad (2.46)$$

and

$$F(x) = \frac{1}{2} + \frac{1-x^2}{4x} \ln \left| \frac{1+x}{1-x} \right|. \quad (2.47)$$

Then the total energy is

$$\begin{aligned} E &= \sum_{k < k_F} \epsilon(k) \\ &= N \left[\frac{3}{5} \frac{k_F^2}{2} - \frac{3}{4\pi} k_F \right]. \end{aligned} \quad (2.48)$$

The first term is the kinetic energy E_k of non-interacting electrons and the second is the exchange energy E_x . If we put in the electron density $n = \frac{k_F^3}{3\pi^2}$, then we obtain different function dependence of them on the electron density n , where $E_k \propto n^{2/3}$, and $E_x \propto -n^{1/3}$. If we allow different Fermi wave vector $k_F^{\uparrow(\downarrow)}$ for the spin up and spin down electrons, then it can be easily shown that for a completely polarized system, where all the electrons are spin up, $k_F^{\uparrow} = 2^{1/3}k_F$, the energy amounts to

$$E^P = N \left[\frac{3}{5} 2^{2/3} (k_F^{\uparrow})^2 - \frac{3}{2\pi} 2^{1/3} k_F^{\uparrow} \right]. \quad (2.49)$$

The kinetic energy is increased by $2^{2/3}$ and the magnitude of the negative exchange energy is lowered by $2^{1/3}$. A plot of kinetic energy, magnitude of the exchange energy, and total energy of the fully polarized and nonpolarized systems

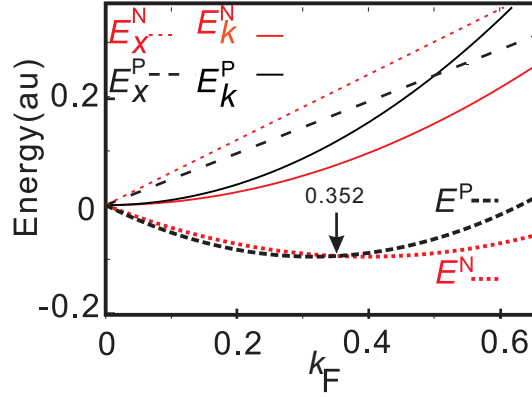


Figure 2.2: The total energy $E^{N,P}$, the kinetic energy $E_k^{N,P}$ and the magnitude of the exchange energy $E_x^{N,P}$ of the fully polarized (P) and nonpolarized (N) electron systems as a function of the Fermi vector k_F .

is shown in Figure 2.2. It can be seen that E^P can be smaller than the nonpolarized case E^N . This happens for small k_F , i.e. $k_F \leq k_F^0 = \frac{5}{2\pi} \frac{1}{2^{1/3}+1} \approx 0.352$. Thus, for a low electron density it is expected that the system is spin polarized. This simple model shows that if the volume is shrunk the electron density will be higher, and the system loses its magnetization. The correlation energy reduces the tendency to itinerant ferromagnetism. A more exact treatment of the homogenous electron gas was done by Ceperley and Alder [6] by quantum Monte Carlo simulations. It was found that the polarized (ferromagnetic) Fermi liquid is stable between $r_s = 75$ and $r_s = 100$ where $r_s \cong 1.92/k_F$ is the electron density parameter. Below that it is normal paramagnetic Fermi fluid, and above that, the electrons crystalize into a Wigner crystal.

2.5.2 The Stoner model

In the original proposal by E. C. Stoner [10], this model accounts for the itinerant magnetism both at $T = 0$, and $T \neq 0$. Here we concentrated on the model at $T = 0$, because it provides a criterion for the existence of ferromagnetism in the ground state. If we have the density of states $D(E)$ by a non-polarized calculation, we can produce a ferromagnetic state by a rigid shift of the spin-up and spin-down states [11] as

$$\begin{aligned} D_{\uparrow}(E) &= D(E + \Delta E_{\uparrow}), \\ D_{\downarrow}(E) &= D(E + \Delta E_{\downarrow}). \end{aligned} \quad (2.50)$$

where $\Delta E_{\uparrow} > 0$ and $\Delta E_{\downarrow} < 0$. Here, $D_{\uparrow}(E)$ and $D_{\downarrow}(E)$ are the densities of states for spin-up and spin-down electron subbands, respectively. The energy shifts ΔE_{\uparrow} and ΔE_{\downarrow} of $D_{\uparrow}(E)$ and $D_{\downarrow}(E)$ with respect to $D(E)$ are constrained by the charge conservation

$$\int_{\Delta E_{\downarrow}}^0 dE D(E) = \int_0^{\Delta E_{\uparrow}} dE D(E), \quad (2.51)$$

where the Fermi level E_F is put at $E = 0$. The spin magnetic moment is given by $\mu = \frac{1}{2}m\mu_B$, where m is the number of unpaired electrons and μ_B is the Bohr

magneton. The m can be obtained by counting the electrons in the spin-up and spin-down subbands, taking care of the charge neutrality given by Equ. (2.51), as

$$\begin{aligned} m &= \int_{-\infty}^0 [D_{\uparrow}(E) - D_{\downarrow}(E)] dE \\ &= 2 \int_0^{\Delta E_{\uparrow}} D(E) dE \end{aligned} \quad (2.52)$$

The energy difference between a nonmagnetic and a ferromagnetic state consists of two parts. The first part is the increase of band energy ΔE_b due to the reoccupation of states near the Fermi level. The second part is the decrease of the exchange energy contribution ΔE_{ex} which depends on the Stoner parameter I . This energy should only have even order terms of m because of symmetry. In the lowest order approximation, it is proportional to m^2 . Hence, we can write the total energy difference as

$$\begin{aligned} E_{mag} &= \Delta E_b + \Delta E_{ex} \\ &= \int_{\Delta E_{\downarrow}}^{\Delta E_{\uparrow}} E D(E) dE - \frac{1}{4} I m^2. \end{aligned} \quad (2.53)$$

The instability of the system with respect to onset of ferromagnetism is

$$\frac{\partial^2 E_{mag}}{\partial m^2} < 0. \quad (2.54)$$

From equation (2.51),

$$-D(\Delta E_{\downarrow}) \frac{\partial \Delta E_{\downarrow}}{\partial \Delta E_{\uparrow}} = D(\Delta E_{\uparrow}). \quad (2.55)$$

The first derivative of the band energy with respect to m reads,

$$\begin{aligned} \frac{\partial E_b}{\partial m} &= \frac{\partial E_b}{\partial \Delta E_{\uparrow}} \frac{\partial \Delta E_{\uparrow}}{\partial m} + \frac{\partial E_b}{\partial \Delta E_{\downarrow}} \frac{\partial \Delta E_{\downarrow}}{\partial m} \\ &= \frac{\Delta E_{\uparrow} - \Delta E_{\downarrow}}{2}, \end{aligned} \quad (2.56)$$

and the second derivative is

$$\begin{aligned} \frac{\partial^2 E_b}{\partial m^2} &= \frac{\partial(\Delta E_{\uparrow} - \Delta E_{\downarrow})}{2 \partial m} \\ &= \frac{1}{4} \left(\frac{1}{D(\Delta E_{\uparrow})} + \frac{1}{D(\Delta E_{\downarrow})} \right). \end{aligned} \quad (2.57)$$

If we define an average density of state by

$$\frac{1}{\bar{D}(m)} = \frac{1}{2} \left(\frac{1}{D(\Delta E_{\uparrow})} + \frac{1}{D(\Delta E_{\downarrow})} \right), \quad (2.58)$$

the instability of the nonmagnetic state according to Equ. (2.54) is given by

$$I \bar{D}(0) > 0, \quad (2.59)$$

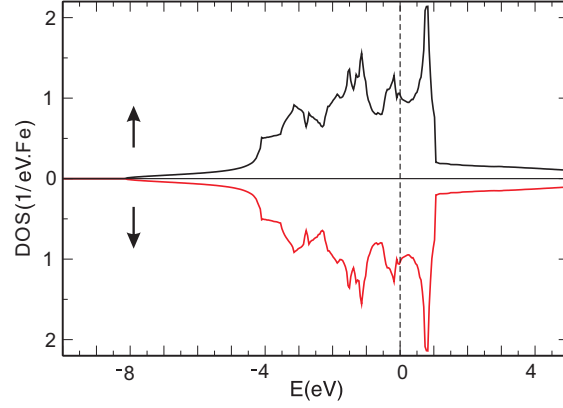


Figure 2.3: Density of states for FCC iron at $a_0=3.60$ Å. The Fermi level is indicated by the vertical dashed line.

where $\bar{D}(0)$ is the averaged nonmagnetic DOS at the Fermi level. This is the famous Stoner criterion for ferromagnetism at $T = 0$.

The requirement of stationarity of E_{mag} ,

$$\partial E_{mag} / \partial m = 0, \quad (2.60)$$

gives, apart from the “trivial” solution $m = 0$, a possible magnetic solution. It is stable if $\partial^2 E_{mag} / \partial m^2 > 0$. Substituting Equation (2.53) into (2.60), Equ. (2.60) can be rewritten as

$$Y(m) \stackrel{def}{=} \frac{2\partial E_b}{m\partial m} = I = \bar{D}^{-1}(m), \quad (2.61)$$

and the stationarity requires $Y'(m) > 0$.

From Equ. (2.58), we can see that if $D(\Delta E_\uparrow)$ and $D(\Delta E_\downarrow)$ are both high for several m 's, we can have several magnetic solutions satisfying Equ. (2.61) [11]. In fact, for each magnetic solution, the Fermi level situating in the “valley” of the DOS is mostly favorable for multiple magnetic solutions as will be discussed in details in Chapter 4.

2.5.3 An application in FCC iron

Here we show an application of the above consideration to face centered cubic (FCC) iron. It was already shown from fixed spin moment calculations by Moruzzi [12] that there are multiple solutions with different magnetic moments. Here we use the flavor of equations in the above section to discuss the solutions. In Figure 2.3, the density of states for the nonmagnetic solution at a lattice constant of $a_0 = 3.60$ Å is shown. In order to find the magnetic solution, we plot $Y(m) = \frac{2\partial E_b}{m\partial m}$ in Figure 2.4, where E_b and its derivatives are calculated numerically by equations from Equ. (2.50) to the first term in the r.h.s. of Equ. (2.53). Then the magnetic solutions are obtained by the cross points of a horizontal line with coordinate equal to the Stoner parameter I and the curve. The stability of the solutions are determined by the sign of $\partial^2 E_{mag} / \partial m^2$. As mentioned above, the stable solutions are the crossing points for which $Y'(m) > 0$. For FCC iron,

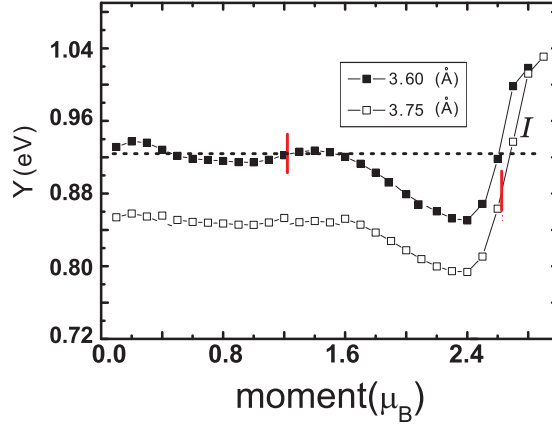


Figure 2.4: Plot of $Y(m) = \frac{2\partial E_b}{m\partial m}$ versus the magnetic moment (m). The short vertical lines indicate the magnetic solutions at these lattice constants by self-consistent spin polarized calculations.

the curve of $Y(m)$ corresponding to different lattice constant yielding magnetic solutions: $a_0=3.60$, and 3.75 Å, respectively are shown in Figure 2.4. We have also performed self-consistent calculations to find the magnetic solutions. The calculated magnetic moments for the different lattice constants are shown by the short red vertical lines on the corresponding curves. It can be seen that results from our simple model agree with the self-consistent spin polarized calculation. The horizontal line indicates the $I = 0.93$ eV [13] from the most recent results. Earlier result of shows $I = 0.92$ eV [14]. This scatter of I does not influence our discussions here. It is obvious that the nonmagnetic, low spin ($\sim 1.2\mu_B$) and high spin ($\sim 2.6\mu_B$) solutions can be obtained from the curves with the lattice constant $a_0=3.60$ Å. For the other curve where the lattice constant is expanded by $\sim 4\%$, there is only one magnetic solution with a larger magnetic moment ($\sim 2.7\mu_B$). This agrees semi-quantitatively with the results of Morruzi.

This rigid band consideration provides a bird's eye view of the multiple magnetic solutions with minor calculation efforts. This crude estimation can give us a first answer to the question whether there are several magnetic states existing in the system or not and possible magnetic moments can be estimated.

2.6 The band Jahn-Teller effect

The Jahn-Teller effect is the intrinsic instability of an electronically degenerate complex against distortions that remove the degeneracy. It was first predicted as a very general phenomenon in 1937 by Jahn and Teller [15]. In solids, there exists a phenomenon equivalent to the Jahn-Teller effect (namely, the band Jahn-Teller effect): When there are degenerated bands around the Fermi level, if we allow a slight distortion of the lattice which lowers the symmetry of the crystal, this distortion will lead to a split of the bands, but does not change their center of gravity. Thus the distortion is favored if the gain in band energy by occupation of the lower one of the split bands overcompensates the loss of elastic energy due to the distortion. We illustrate two model systems to understand

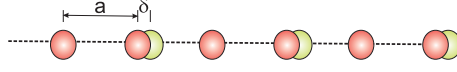


Figure 2.5: Atoms form a linear chain with a regular distance of a . If every second atom is displaced by δ , the new periodicity is $2a$.

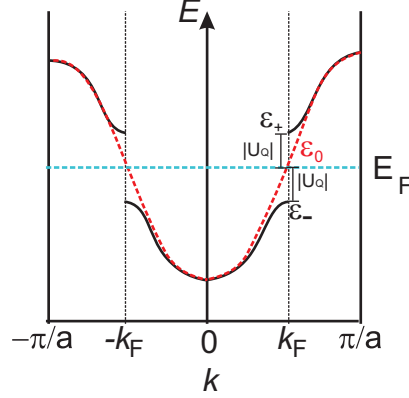


Figure 2.6: A schematic band structure of a linear chain of equidistant atoms (the red broken line curve), and that after the Peierls distortion (the solid black curves). The Fermi level is shown by a dashed horizontal line.

this effect.

2.6.1 a one dimensional case—the Peierls distortion [16]

Consider a linear chain of atoms with a large length of L , with regular spacing a as shown in Figure 2.5. For an odd number of electrons, the valence band will be half filled. The band is assumed to have a shape like the red broken line curves as in Figure 2.6. The Fermi wave number is $k_F = \pi/2a$ if there is only one electron per atom.

If every second atom is displaced by a small distance δ , this doubles the periodicity of the chain, and the potential acquires a Fourier component of wave number $Q = \pi/a$, which in this case is equal to $2k_F$. Then the states with k and $k - Q$ will be coupled by this potential. The new state can be assumed to be a linear combination of them. According to the nearly free electron model, the secular equation is written as:

$$\begin{vmatrix} \epsilon - \epsilon_k^0 & -U_Q \\ -U_Q^* & \epsilon - \epsilon_{k-Q}^0 \end{vmatrix} = 0, \quad (2.62)$$

where ϵ_k^0 is the undisturbed dispersion, and U_Q is the Fourier component of the crystal potential with wave vector $Q = \frac{\pi}{a}$. The two roots of the secular equation are

$$\epsilon_{\pm}(k) = \frac{1}{2}(\epsilon_k^0 + \epsilon_{k-Q}^0) \pm [(\frac{\epsilon_k^0 - \epsilon_{k-Q}^0}{2})^2 + |U_Q|^2]^{1/2}, \quad (2.63)$$

as displayed by the solid curves in Figure 2.6.

Taking the free electron dispersions:

$$\epsilon_k^0 = \frac{1}{2}k^2, \epsilon_{k-Q}^0 = \frac{1}{2}(k-Q)^2, \quad (2.64)$$

At $k = \frac{\pi}{2a}$, $\epsilon_k^0 = \epsilon_{k-Q}^0$, then $\epsilon_{\pm} = \epsilon_k^0 \pm |U_Q|$. Namely, at this point, the eigen energy is split by an amount of $2|U_Q|$ as shown in the figure.

The band energy per unit volume (E_b) of the distorted system can be evaluated by integration from $-\pi/2a$ to $+\pi/2a$, multiplied by $L/2\pi$, the number of electron states per unit volume in k-space:

$$\begin{aligned} E_b &= \frac{1}{L} \frac{L}{2\pi} 2 \int_0^{k_F} dk \epsilon_{-}(k) \\ &= \frac{1}{\pi} \int_0^{k_F} dk \epsilon_{-}(k) \\ &= \frac{1}{\pi} \int_0^{k_F} dk \left\{ \frac{1}{4}[k^2 + (k-Q)^2] - \frac{k_F}{2} \sqrt{(k - \frac{Q}{2})^2 + (\frac{2U_Q}{Q})^2} \right\} \\ &= \frac{1}{6\pi} k_F^3 - \frac{1}{\pi} \left\{ z \frac{k_F^2}{4} + \frac{U_Q^2}{k_F} \ln \frac{z + k_F/2}{z - k_F/2} \right\} \end{aligned} \quad (2.65)$$

where $z = \sqrt{k_F^2/4 + 4U_Q^2/k_F^2}$. When the displacement of the atoms (δ) is small, we can expect that U_Q is small and proportional to δ . Then we have a term in the reduction of the band energy like

$$\Delta E_b \sim -U_Q^2 \ln U_Q \sim -\delta^2 \ln \delta. \quad (2.66)$$

The tiny displacement δ will increase the elastic energy by ΔE_{el} which is only proportional to δ^2 . Thus we can see that if the distortion is small, the logarithmic term in the reduction of the band energy ΔE_b dominates. The distortion is then favorable for the system. This means that the one dimensional atomic chain with half occupied bands exhibits a spontaneous distortion which introduces a new periodicity, frequently called a charge density wave (CDW).

2.6.2 A two dimensional case—the square lattice model

The second model system we consider is a square atomic lattice as shown in Figure 2.7. For simplicity, only the p_z orbitals with a nearest neighbor interaction is included. The dispersion of the related Bloch states is schematically illustrated in Figure 2.8(a).

In the undistorted square net, a 90° rotation around z axis is a symmetry operation. The wave vectors $\mathbf{k} = \frac{\pi}{a}[1, 0]$ and $\mathbf{k} = \frac{\pi}{a}[0, 1]$ transform into each other by this operation. The p_z based crystal orbitals at these two k-points belong to the same irreducible representation, and are degenerate as shown in Figure 2.8(a). But for a rectangular net, a 90° rotation is not a symmetry operation any longer. Thus these two orbitals, at $\mathbf{k} = \frac{\pi}{a}[1, 0]$ and $\mathbf{k} = \frac{\pi}{a}[0, 1]$, are no longer degenerate as shown in Figure 2.8(b). The state at $[0, 1]$ has lower energy in our example. The difference of the eigenvalues is Δ . If we assume that each orbital at $[1, 0]$ and $[0, 1]$ is half filled, in the square lattice the electron equally occupies these states, as in Figure 2.8(a). In the rectangle lattice the

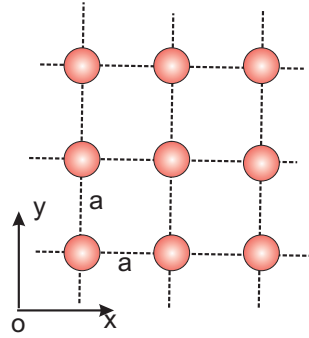
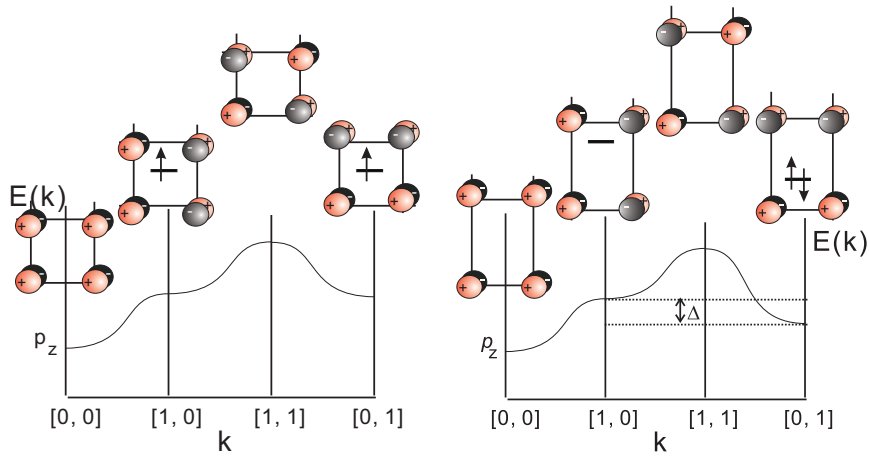


Figure 2.7: Atoms form a square lattice with a lattice constant a .



(a) A cartoon band structure of the p_z band in a square lattice. The states at $[1,0]$ and $[0,1]$ are degenerate.

(b) A cartoon band structure of the p_z band in a rectangle lattice. The degeneracy of the orbital at $[1,0]$ and $[0,1]$ is lifted by an amount of Δ after the distortion.

Figure 2.8: A schematic illustration of the dispersion of the p_z band along the high symmetric lines in the reciprocal space of the square and rectangle lattices. The “+” and “-” indicate the phase of the orbitals. Electrons are denoted by the up arrows.

degeneracy at $[1,0]$ and $[0,1]$ is removed. Thus, the state at $[0,1]$ will be double occupied and the orbital at $[1,0]$ will be empty, as denoted in Figure 2.8(b). This reduces the energy by $\Delta \ln \Delta$ per electron. Thus the half filling of the p_z orbital will produce the rectangle lattice distortion stabilized by the band Jahn-Teller effect. The stability of body centered cubic and face centered cubic structural phases in some transitional metals and their alloys were recently analyzed from this perspective [17].

From the previous two pedagogical examples, we see that the band Jahn-Teller effect happens in high symmetric phases. A lot of interesting phenomena are proposed to be connected with the band Jahn-Teller effect, such as the charge density wave, orbital ordering or some structural phase transitions. In this thesis, stabilization of tetragonal phases of Rh_2MnGe against cubic phases is proposed to result from the band Jahn-Teller effect as we will discuss in Chapter 3.

Chapter 3

Band Jahn-Teller effects in Rh_2MnGe

3.1 Introduction to Heusler alloys and related experiments

Magnetic compounds with a Heusler structure receive a lot of research interests because of their unique characteristics. For example, Ni_2MnGa is a typical magnetic shape memory (MSM) alloy which exhibits large changes in shape and size in an applied magnetic field. This deformation can be as large as 10%. It can find its applications in actuators and sensors. A martensitic transformation from a high symmetry cubic (austenitic) phase at higher temperatures to a lower symmetry phase, for example, a tetragonal (martensitic) phase at lower temperatures is thought to be a precondition for this large shape or volume change. Both experimental and theoretical works were conducted to study this effect [18]. The reason for the phase transition was proposed to be phonon softening, which in turn originates from Fermi surface nesting [19]. Another important characteristic of some ferromagnetic Heusler alloys is half-metallicity, which means that the density of states (DOS) of one spin channel is zero while the DOS of the other channel is finite. Co_2MnX ($X=\text{Ge, Si, Sn, etc.}$) are such compounds. They have the potential to be used as spin injection materials in spintronics, although at present, the experimental results are not so promising: the spin injection efficiency is much lower than the theoretical prediction [20]. The reason is that the local density of states at the Fermi level close to the interface is quite susceptible to defects such as atomic disorders, interfaces and surface segregation, *etc.*

As a member in the family of Heusler alloy, Rh_2MnGe with an $L2_1$ structure was first reported, as far as I know, by Hames *et al.* [21] some thirty years ago. Later on, extended and systematic experimental works on Rh_2MnX (X is Al, Ga, In, Tl, Sn, Pb, and Sb) were reported by Suits [22]. It was found that for most X in group IV B they are ordered in the $L2_1$ phase, but for X in group III B they are crystallized in the disordered $B2$ phase. The former compounds are ferromagnetic with a higher Curie temperature above room temperature and exhibit larger magnetic moments at low temperatures compared with the latter

ones. The Sn hyperfine field in $\text{Rh}_2\text{MnGe}_{0.98}^{119}\text{Sn}_{0.02}$ and Rh_2MnSn measured by Dunlap *et al.* [23] suggested that it is more closely related to the Co based alloy than those with Ni, Pd or Cu at the Rh site in the sense that Rh atoms do carry magnetic moments comparable with the Co moments in the Co_2YZ Heusler alloys.

Density functional theory (DFT) calculations of this material were reported by Pugacheva [24], concentrating on the effects of atom substitutions and atomic disorders. It was shown that the magnetic moment deteriorates by disorder which may be tuned by the heat treatment. Recently, electronic structures of a number of Heusler alloys were calculated by Galanakis *et al.* [25], where the Slater-Pauling behavior of the magnetic moment in most of these materials was shown. The Rh_2MnGe compound does not fall on the Slater-Pauling curve, because of the nonvanishing DOS of the down spin channel, namely, it is not a half-metal. All of the electronic structure calculations published, hitherto, were devoted to the cubic phase of Rh_2MnGe . Recent experiments by Adachi *et al.* [26] showed some indications of a phase transition in Rh_2MnGe under hydrostatic pressure of about 0.6 GPa, but the structure of the high pressure phase was not identified. The density of states of the cubic structure obtained by Pugacheva [24] and Galanakis [25] shows that the Fermi level is situated at a peak (van Hove singularity) of the DOS, which implies that the cubic phase may not be stable at zero temperature. Although the martensitic transition is widely reported in the Heusler compounds by DFT calculations, not all of the compounds have the tetragonal structure in the ground state [18]. As reported by Ayuela *et al.* [18], among Co_2MnGa , Ni_2MnAl , Ni_2MnGa , Ni_2MnSn , Ni_2CoGa , and Fe_2CoGa , the cubic structure is stable in all Mn alloys except Ni_2MnGa . This is related to the MSM effect in this compound. The phonon dispersions of $\text{Ni}_2\text{MnGa}(\text{Ge}, \text{Al})$ and $\text{Co}_2\text{MnGa}(\text{Ge})$ were calculated by Zayak *et al.* [27]. The softening of the TA_2 mode is proposed to be the reason for the structure instability. An interesting question is whether the temperature induced structural phase transition in Ni_2MnGa also takes place in Rh_2MnGe ? A first trial to answer this question is to conduct DFT calculations and probe some possible phases at $T=0$. Intrigued by the experimental results of Ni_2MnGa , the first non-cubic structure that comes to our mind is the tetragonal phase, which is obtained by extension or compression of the cubic lattice in one direction while the other two respond accordingly. We thus carried out density functional calculations of Rh_2MnGe in order to study the ground state properties, including possible distorted phases, their magnetic moments, and their relations to electronic structures.

3.2 Calculation details

The Rh_2MnGe compound crystallizes at room-temperature in the $L2_1$ structure which consists of four face centered cubic (FCC) sublattices. The space group is $Fm\bar{3}m$ (No. 225) with the following Wyckoff positions: Rh: $8c(1/4, 1/4, 1/4)$, Mn: $4b(1/2, 1/2, 1/2)$, and Ge: $4a(0, 0, 0)$. The tetragonal distortion that results in a change of the space group to $I/4mmm$ (No. 139) with Wyckoff positions: Rh: $4d(0, 1/2, 1/4)$, Mn: $2b(0, 0, 1/2)$, and Ge: $2a(0, 0, 0)$. The results for the cubic structure were also obtained by using the symmetry of the tetragonal structure, and the consistency of the calculations has been checked.

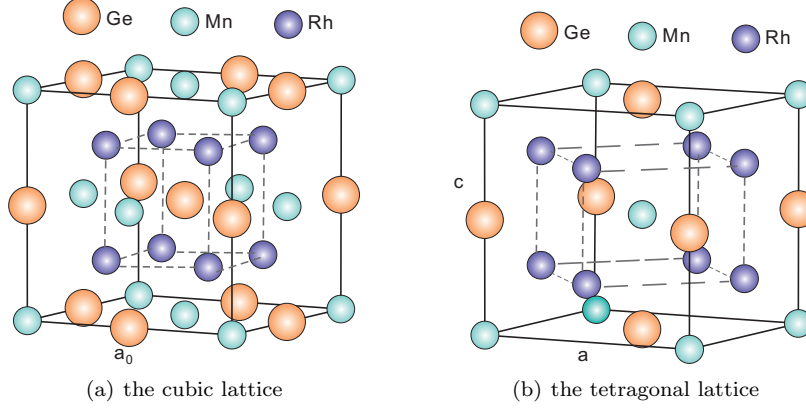


Figure 3.1: The conventional unit cell of Rh_2MnGe in a cubic (a) and a tetragonal (b) lattice. The tetragonal lattice is rotated by 45° around the vertical axis as compared to the cubic lattice.

Table 3.1: Comparison of the calculated lattice constant and magnetic moments of the cubic structure with experimental results and previous calculations of the cubic Rh_2MnGe compound. The chosen method and parameterization of the xc-potential is given in parenthesis.

	Present work FPLO (PW92)	Calculation [24] LMTO (vBH)	Experiments
$a_0(\text{\AA})$	5.97	6.102	5.99 [21], 6.030 [22]
$m_{tot}(\mu_B)$	4.51	4.47	4.30 [21], 4.62(4) [22]
$m_{Rh}(\mu_B)$	0.36	0.39	
$m_{Mn}(\mu_B)$	3.80	3.69	
$m_{Ge}(\mu_B)$	-0.016	0.004	

In this case, the tetragonal lattice constants (a , c) equal $(a_0/\sqrt{2}, a_0)$, where a_0 is the cubic lattice constant. The cubic and tetragonal structures are shown in Fig. 3.1 (a) and (b), respectively. The number of k-points in the irreducible part of the Brillouin zone (IBZ) is 67685 in the calculations. The basis is chosen as follows: Rh: 4sp/4d5sp+5d, Mn: 3sp/3d4sp+4d, Ge: 3spd/4spd. The local spin density approximation is applied and the parameterization of the exchange and correlation potential by Perdew and Wang [7] was chosen. The convergence of the self-consistent iterations is checked with respect to both the density (10^{-6} in code specific units) and the total energy (10^{-8} Hartree).

3.3 Main results of the calculations

3.3.1 The lattice constant and the magnetic moment of the cubic phase

The calculated lattice constant (a_0), total (m_{tot}) and local (m_{Rh} , m_{Mn} , and m_{Ge}) magnetic moments of the cubic structure at zero temperature are listed in Table 3.1 and compared with previous experimental and theoretical values.

The lattice constant is in good agreement with the experiments, especially with the measurement of Hames [21]. The difference is within 1% for both experiments. It is within the error bound of LSDA. The somewhat larger theoretical value reported in Ref. [24] is probably due to the less accurate numerical method (LMTO-ASA) that obviously yields an (over-shooting) error cancelation of the overbinding of LSDA.

The magnetic moments of the cubic structure show a relatively larger discrepancy. Theoretical result ($m_{tot} = 4.47\mu_B$) by Pugacheva [24] agrees better with ours. Nevertheless, our result is between the experiments. The differences between the atomic spin moments, which are not well defined both experimentally and theoretically, is probably due to different projections. There is a ferrimagnetic coupling between Ge and the other atoms. Similar results were also reported in other Heusler alloys by Kübler [28] and Fujii [29]. It is from the hybridization (covalent bonding) of the magnetic $3d$ states and the nonmagnetic $4sp$ states. This hybridization, because of the different energy of the $3d$ up and down spins, results in a spin split of the $4sp$ states, which couple ferrimagnetically with the $3d$ spin moment. This covalent bonding will be discussed in the next chapter.

3.3.2 Crystal structures at the ground state

In order to obtain the relative stability of the cubic and the tetragonal structures, we relaxed c/a ratios under different volumes under our consideration. We have the energy contour plotted as a function of the c/a and relative volume (V/V_0 , where V_0 is the volume per formula unit of the energy minimum of the cubic phase) shown in Figure 3.2. Two local minima that are denoted with “+” signs in the figure at $c/a=1.39$, volume = 105.54 \AA^3 and $c/a=1.60$, volume = 105.30 \AA^3 are obtained. Here and after, we refer to these two phases as tetI and tetII, respectively. When the relative volume is between 94% and 106% of the equilibrium volume of the cubic phase, the two energy minima are present, and the cubic structure gives a local maximum of $E(V)$. Typical energy variations with respect to the c/a ratio under a fixed volume are plotted in Figure 3.3. In Figure 3.3(a) the volume is 105.32 \AA^3 , we have two energy minima with $c/a=1.61$ and 1.38 . The cubic phase with $c/a=\sqrt{2}$ is a local maximum. At volumes smaller than 94% of the equilibrium volume of the cubic phase, the $c/a=\sqrt{2}$ is an inflexion point. Then only a global minimum with extended c -axis exists. As an example, the energy versus c/a curve at the volume of 100.10 \AA^3 are shown in Figure 3.3(b).

In the experiments, the cubic $L2_1$ phase was detected at elevated temperatures, while our calculation shows a local energy maximum for this cubic phase at zero temperature. Although the calculated energy differences are tiny and within the accuracy of the LSDA, there is no doubt a flat region and a tendency towards tetragonal distortions. Regarding to this, we propose a possible phase transition caused by temperature. The electronic origin of the predicted phase transition is the band Jahn-Teller effect which will be justified in detail in the following section. More detailed electronic structure discussions come right after the following pressure effect.

The volume dependence of total and local magnetic moments is shown in Figure 3.4. The total magnetic moment is contributed mainly from the $3d$ electrons of Mn. The decrease of the Mn magnetic moments with the decrease

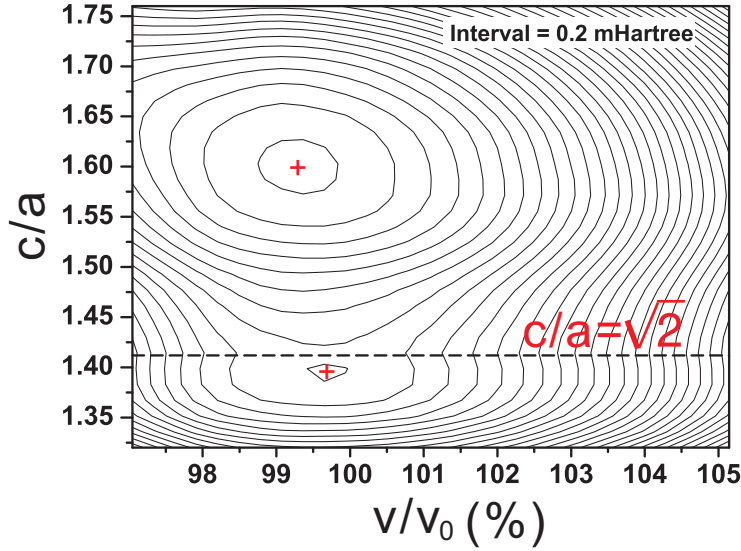
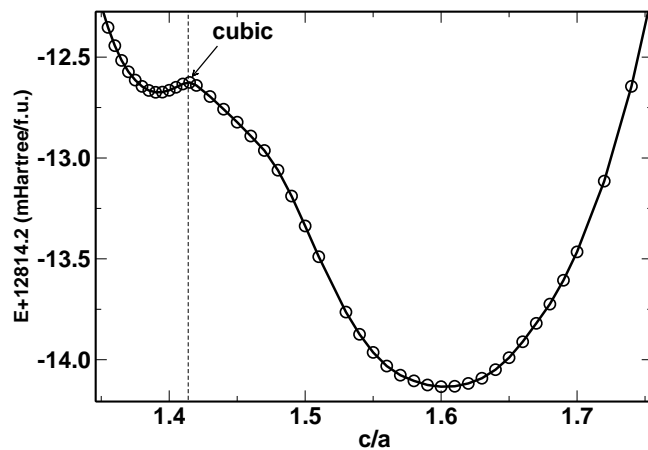


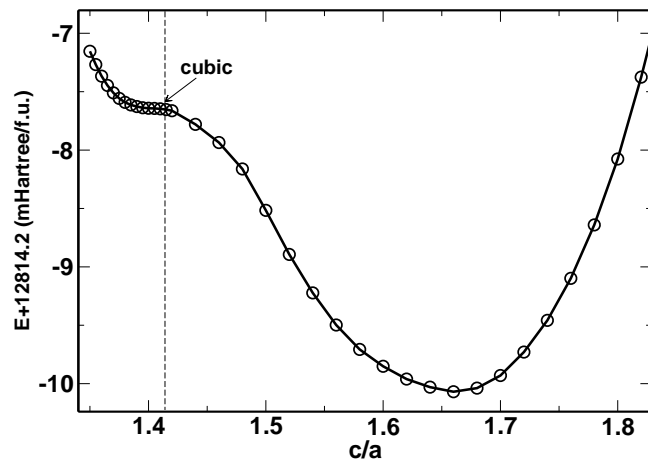
Figure 3.2: The contour plot of the energy with respect to relative volume and c/a . The dashed horizontal line with $c/a = \sqrt{2}$ indicates the cubic phase. The two crosses indicate the two local energy minima in the plot corresponding to the two tetragonal structures. $V_0 = 105.85 \text{ \AA}^3$ is the volume of the energy minimum of the cubic phase.

of volume is common for itinerant magnetism, as band broadening deteriorates the magnetism.

Comparing the spin moment of the cubic phase and the tetII phase at the same volume, the magnetic moment is reduced by about 10% as shown in Figure 3.4. The electronic reason of this reduction can be understood by checking the partial DOS of Mn at different c/a ratios. It is shown in Figure 3.5. Considering the conventional unit cell of the tetragonal phase in Figure 3.1 (b), it is found that the nearest neighbors of Mn are eight Rh atoms forming the vertices of tetragonal lattice. The next nearest neighbors are the apical and in-plane Ge atoms. Among the majority spin states there are strong bonding and antibonding states between $d_{x^2-y^2}$, d_{xz} , and d_{yz} orbitals of Mn and the d orbitals of the Rh. The d_{xy} and $d_{3z^2-r^2}$ orbitals form nonbonding states. In the cubic phase states formed by the first three orbitals are degenerate, and the latter two are also degenerate as shown in Figure 3.5(c). Under tetragonal distortion, the first three degenerate states split into $E_g(xz, yz)$ and $B_{1g}(x^2 - y^2)$ according to the irreducible representation of the point group ($4/mmm$) of Mn. Thus the antibonding E_g states of the majority spin move above the Fermi level under the distortion and the magnetic moment is reduced. With the increase of the c/a ratio, the crystal field splitting is enlarged as can be seen by comparing Figure 3.5(a) to (b), and the magnetic moment is decreased as shown in Figure 3.6, because of the more de-occupation of the majority spin states.



(a) Energy vs. c/a for the tetragonal structure with volume of 105.32 \AA^3 .



(b) Energy vs. c/a for the tetragonal structure with volume of 100.10 \AA^3 . The local minimum at smaller value of c/a is suppressed.

Figure 3.3: Energy versus c/a ratios for the tetragonal structure.

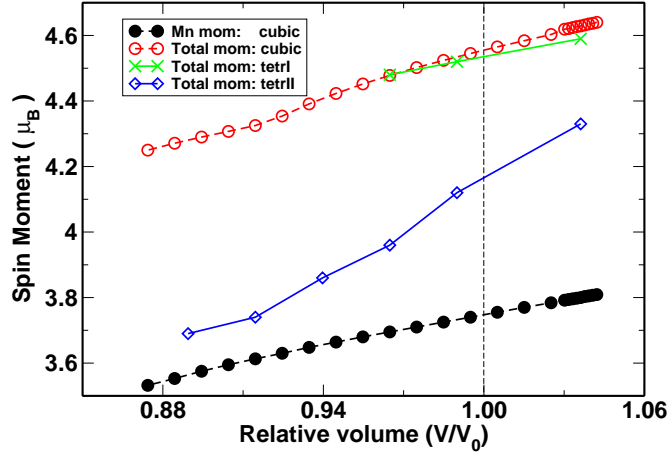


Figure 3.4: The magnetic moment versus relative volume of different phases. The reference volume (V_0) is taken to be the volume (105.85 \AA^3) of the energy minimum of the cubic phase.

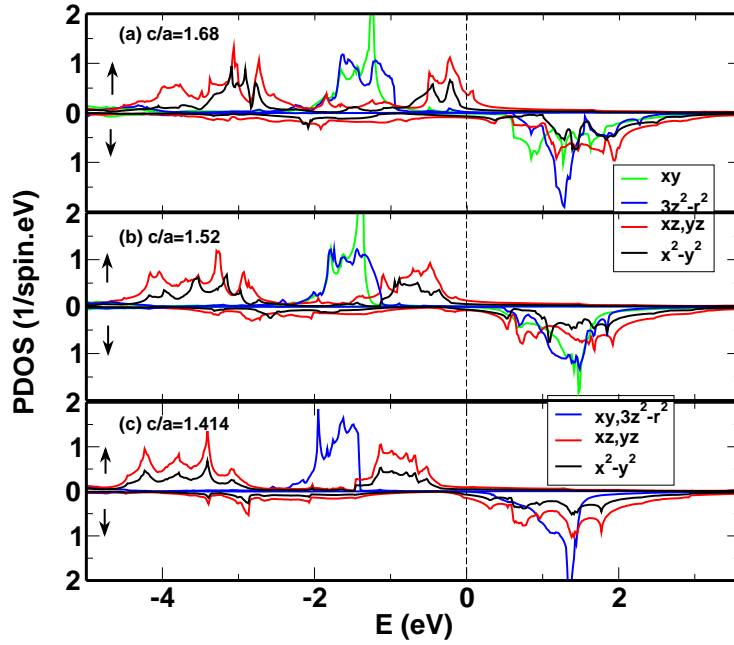


Figure 3.5: Partial DOS of the Mn-3d state resolved into real spherical harmonics contributions at different c/a ratios at the same volume. Figure (a) and (b) are from the tetragonal phase and share the same legend. (c) is from the cubic phase.

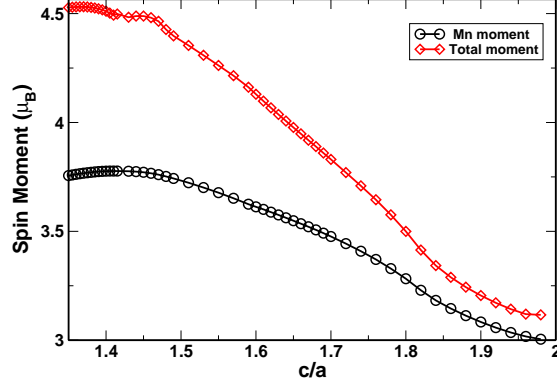


Figure 3.6: The total magnetic moment and the magnetic moment of Mn decrease with the increase of the c/a ratio at the constant volume.

3.3.3 Experimental evidences for the tetragonal phase at low temperature

In order to check the proposed low temperature tetragonal phases, a polycrystalline sample of Rh_2MnGe was synthesized by arc-melting¹. Subsequently, the sample was homogenized at 950 °C for five days in argon. The measurements [30] were performed using an X-ray diffractometer D5000 (Siemens AG) with monochronised $\text{Cu K}\alpha_{1,2}$ radiation ($\lambda_{1,2} = 1.54178 \text{ \AA}$) in Bragg-Brentano. The diffractometer was equipped with a low temperature chamber (APD Cryogenics). The Rh_2MnGe powder was mixed with Standard Silicon Powder 640c (NIST) as an intrinsic line position reference material.

Diffraction patterns in the angle range of $2\theta = 25^\circ$ to 80° with a step width of $\Delta(2\theta) = 0.02^\circ$ and a recording time of $t = 10 \text{ s}$ per step were recorded in the temperature range from 20 to 340 K. In Figure 3.7, the split of the peak around $2\theta = 42^\circ$ corresponding to a cubic to tetragonal phase transition is observed when the temperature is lowered.

From the Rietveld refinement the temperature dependent lattice parameters were obtained and are shown in Figure 3.8. Above a temperature of 180 K the diffraction patterns can be described by the cubic Heusler structure $L2_1$ (space group 225, $Fm\bar{3}m$). Below, a phase transition occurs, becoming visible by a splitting of various peaks in the diffraction patterns (see Figure 3.7). The phase transition is characterized by a symmetry reduction from a cubic to a tetragonal lattice with space group symmetry $I4/mmm$ (No. 139). The phase transition at around 180 K (circle) can clearly be seen. Below the transition temperature the lattice parameter a_0 of the cubic phase splits into the tetragonal parameters a and c . The temperature dependence of c/a points to a second order transition. The largest c/a ratio of the tetragonal phase could be determined to be 1.423 at a temperature of 20 K. This ratio is considerably smaller than the predicted splitting (~ 1.60). However, the calculated energy difference ΔE between the two phases tetI and tetII is below $k_B \cdot 20K$, and imperfections like chemical disorder might be responsible for this difference, as they tend to broad the

¹Experiments in this section were done by my cooperators S. Nils (sample preparations) and Z. Manuel (XRD measurements).

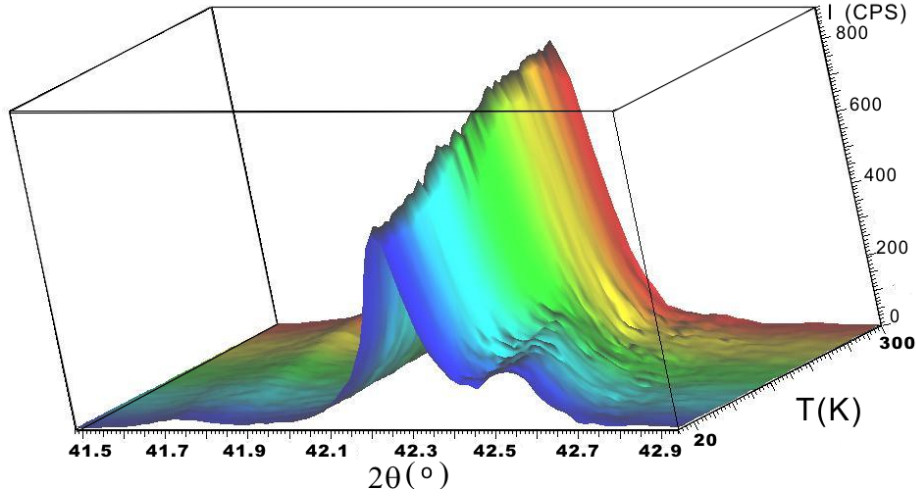


Figure 3.7: Diffraction pattern collected at different temperatures from $T = 20$ K to 340 K around $2\theta = 42^\circ$ [30].

DOS.

3.3.4 An interpretation as the band Jahn-Teller effect

The tetragonal distortion in Rh_2MnGe has been predicted by our calculation and verified by our preliminary experiments. The discovered structural phase transition can be understood by the band Jahn-Teller effect. The general Jahn-Teller theorem [9] asserts that if an ion is at a crystal site of such high symmetry that its ground-state degeneracy is not the Kramers minimum, then it will be energetically favorable for the crystal to distort such that the degeneracy is lifted. The band Jahn-Teller effect is a special case of the theorem as explained in Chapter 2, Section 2.6. If there are degenerate bands very close to the Fermi level, and one allows for a slight distortion of the lattice lowering the symmetry of the crystal, this distortion will lead to a splitting of the degenerate bands, but does not change their center of gravity. Occupation of the lower branches of the split levels must therefore lead to a lower band energy. If the increase of the elastic energy does not exceed the decrease of the band energy, the distortion is favored. The competition between FCC and BCC phases in transition metals and alloys was extensively studied in the spirit of this band Jahn-Teller effect [17].

Full Heusler alloys form in an FCC Bravais lattice. When this lattice is distorted by elongating or shrinking the c axis, it transforms into body centered tetragonal (BCT) lattice. Then former equivalence of the x , y and z directions in the cubic structure is now lifted. Thus the Brillouin Zone (BZ) is also changed. The BZ of the BCT lattice are shown in Figure 3.9. The high symmetric points $X(\frac{2\pi}{\sqrt{2}a}, \frac{2\pi}{\sqrt{2}a}, 0)$ and $Z(0, 0, \frac{2\pi}{c})$ in the BZ of BCT structure are equivalent if the BZ is of FCC lattice ($c = \sqrt{2}a$). The direction $Z - \Gamma_3$ and $X - P$ are also equivalent directions in the latter case. But if the tetragonal distortion is exerted, the points Z and X are no longer equivalent.

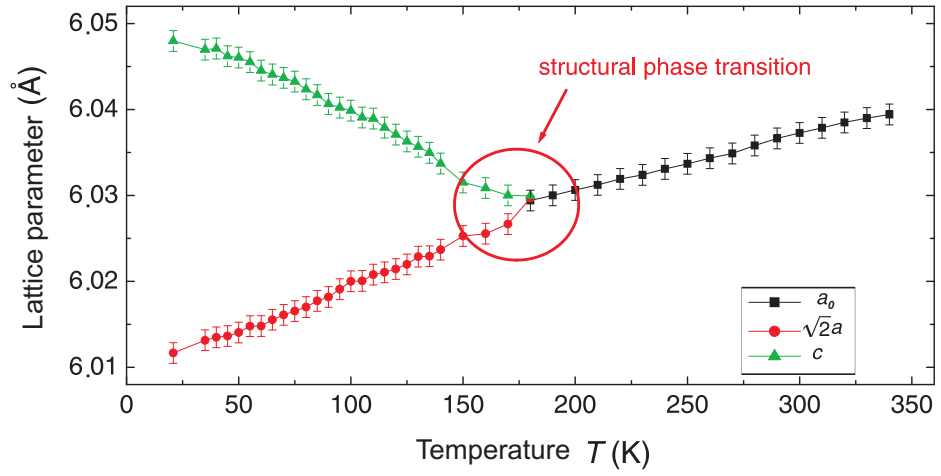


Figure 3.8: Temperature dependence of the lattice parameters in the cubic and tetragonal phases. The phase transition at around 180 K (circle) can clearly be seen. The lattice parameter a_0 of the cubic phase splits into the tetragonal parameters (a, c).

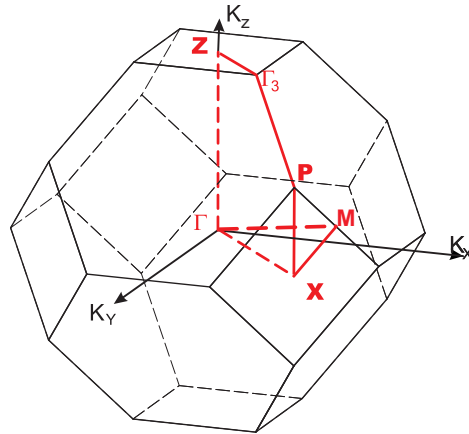


Figure 3.9: The high symmetry points in the BCT Brillouin Zone.

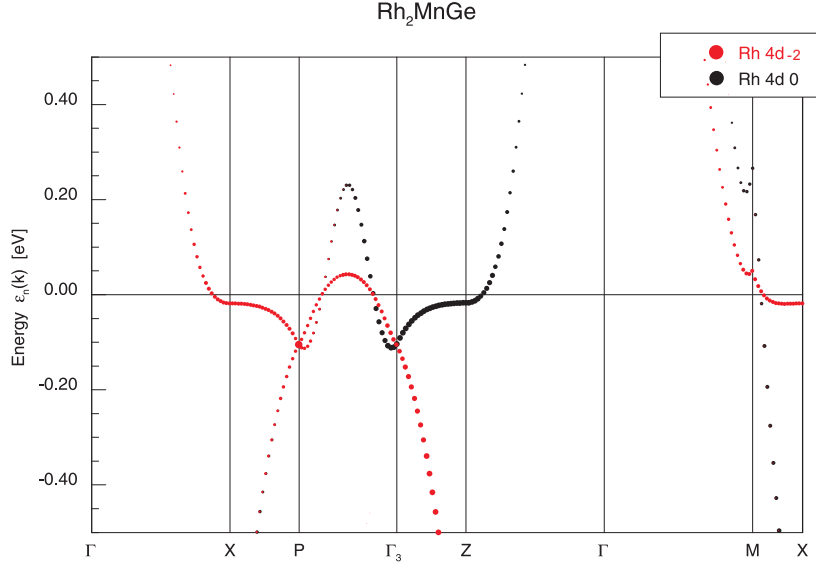


Figure 3.10: Angular and magnetic quantum number resolved bands (majority spin channel) of the cubic phase. The symmetry lines correspond to tetragonal notation as shown in Figure 3.9.

The reduction of symmetry will influence the electronic structures. To see this, firstly the “fat” bands ² of the cubic phase in the BCT BZ are shown in Figure 3.10. In this figure only the bands of Rh with $m_l = -2$ and $m_l = 0$ of the $4d$ orbitals are shown, because it is the main contribution to the majority DOS peak around the Fermi level which will be relevant to our discussion. We see that the eigen energies at X and Z are degenerate in the cubic phase. Also, the dispersions along $X - P$ and $\Gamma_3 - Z$ are the same because of the equivalence of these directions.

When we compress the c -axis, the eigenvalue at X is shifted downwards, while the eigenvalue at Z is shifted upwards because of the antibonding nature of the d_{z^2} electrons. The degeneracy of the bands is lifted. An elongation of the c -axis produces a shift of the eigenvalues in the opposite direction. Both situations are shown in Figure 3.11. The lift of the band degeneracy can also be observed in the density of states, where a splitting of the van Hove singularity close to the Fermi level occurs as shown in Figure 3.12(a). Because the main contribution of the DOS near the Fermi level is from Rh atoms, only the DOS of Rh majority spin channel near the Fermi level for different c/a values is shown in the Figure 3.12 (b) which is a zoomed-in plot of (a). It is clear that there is a high peak in the vicinity of the Fermi level in the cubic phase. Under tetragonal distortions, the peak is split into two with different heights due to the difference of X and Z points. Thus, compression leads to an asymmetric DOS with respect to elongation. In particular, the elongation shifts the higher peak above the Fermi level which decrease the energy more than the compression. The split increases under the larger compression or extension in the c -direction.

The van Hove singularities show a square-root divergency which is the char-

²Energy dispersions weighted by occupations of states.

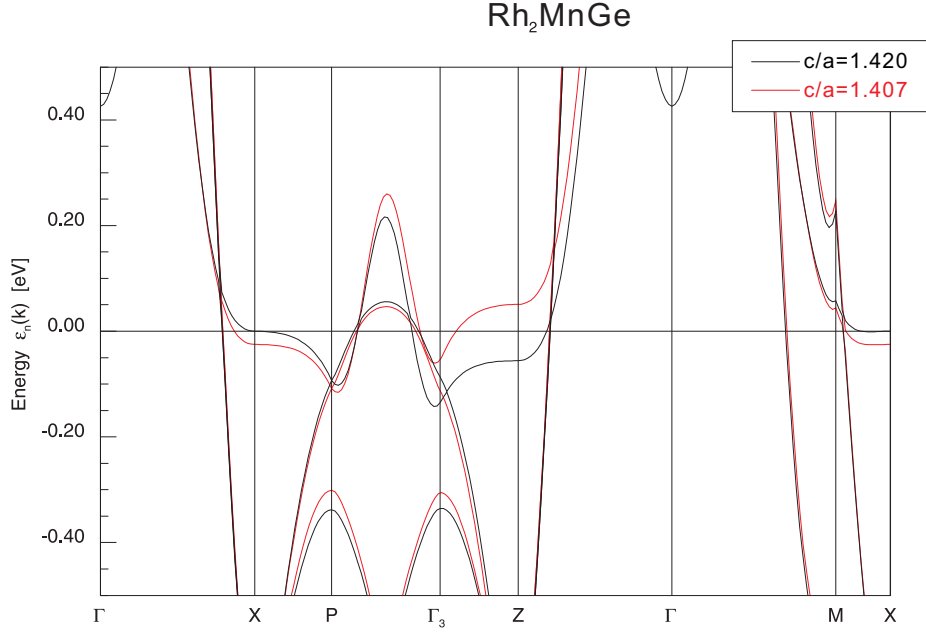
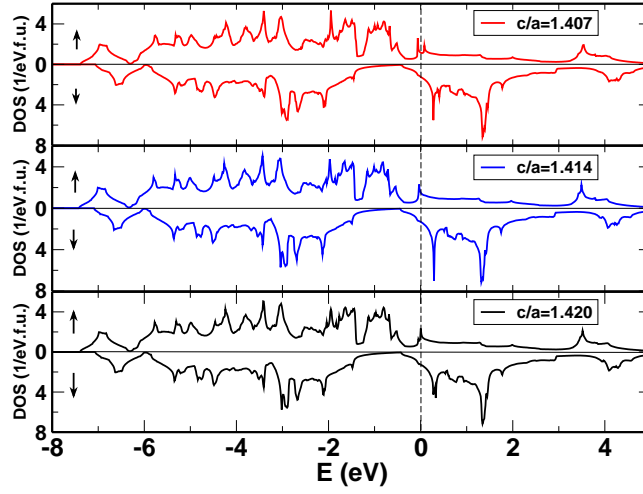


Figure 3.11: Band structure of the elongated (black, $c/a=1.420$) and compressed (red, $c/a=1.407$) tetragonal structure. Only bands from the majority spin channel are shown.

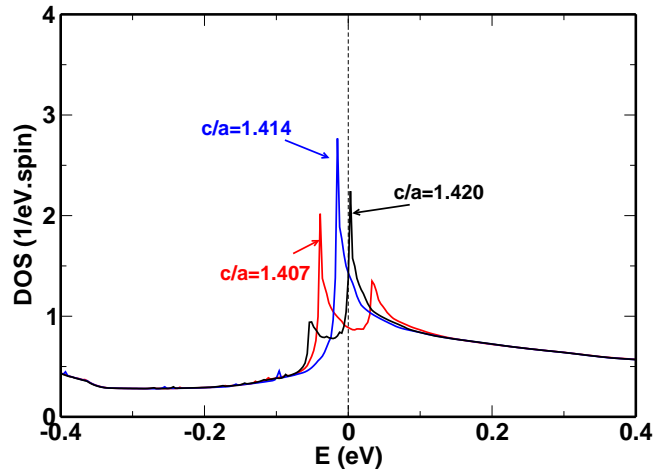
acteristic of one dimensional electronic state. This means the bands in the other two dimensions are non-dispersive. This can be clearly observed in the band in the plane of X-M-P. We can see that in both Figures 3.10 and 3.11 along X-P, and X-M, there are large portions of the bands which are flat.

Here we see that the band Jahn-Teller effect produces a stabilization of the tetragonal ground state. One remark should be added here: whether or not the band Jahn-Teller effect lowers the energy depends on the position of the degenerate bands, namely, whether the Jahn-Teller active bands are near the Fermi level or not. If they are far away from the Fermi level, the distortion still lifts the degeneracy, but does not lower the energy. The position of the bands are largely dependent on the chemical composition of the compound or the band filling. On the other hand, the degeneracy of the Jahn-Teller active orbitals is of course dependent on the crystal field. It is also very sensitive to magnetic polarization. It is the magnetic exchange that put the van Hove singularity of the majority spin near the Fermi level. Atomic disorder, atomic substitutions, or spin disorder will destroy the local symmetry, which will suppress this effect. This might be the reason that the distortion in our experiments is much smaller than the theoretical prediction. We strongly propose that more experiments should be done in samples with better quality to investigate the properties of this compound.

There are other Heusler compounds showing a tetragonal ground state as mentioned in the first section of this chapter. The mechanism for the distortion from the cubic structure may be different. For example, the lattice instabilities in Ni_2MnGa [19] are attributed to the Fermi surface nesting, which leads to a complete softening of the TA_2 transverse acoustic phonon branch along $\langle 110 \rangle$.



(a) The total DOS of Rh_2MnGe for different c/a ratios: 1.407, 1.414, and 1.420.



(b) DOS from the majority spin state of Rh near the Fermi level.

Figure 3.12: Total DOS and DOS of Rh near the Fermi level for different c/a ratios: 1.407, 1.414, and 1.420 at a volume of 105.85 \AA^3 .

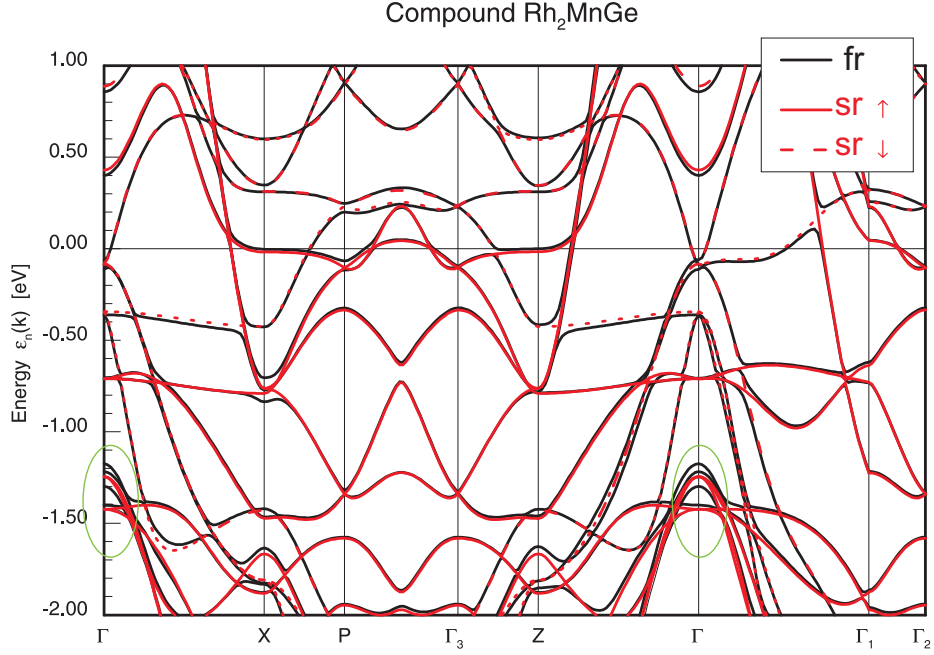


Figure 3.13: Scalar-relativistic (sr) and fully relativistic (fr) band structure of the cubic phase at $V_0=105.85 \text{ \AA}^3$.

On the other hand, Fujii [29] argued that the band Jahn-Teller effect cause the lattice transformation in Ni_2MnGa and Co_2NbSn by comparing the DOS of the cubic and tetragonal structure. In our case, the tetragonal distortion is clearly driven by the band Jahn-Teller effect.

3.3.5 Relativistic effects

We have seen that the band Jahn-Teller effect can explain the instability of the cubic phase versus the tetragonal one. Can the spin-orbital coupling also split the degeneracy? We have checked this point by performing a full relativistic calculation of the cubic phase. The bands from scalar relativistic and fully relativistic calculations at the equilibrium volume, $V_0=105.85 \text{ \AA}^3$ are shown in Figure 3.13. The quantization axis of spin in the full relativistic calculation points along the z-direction. It is clear that the degeneracy at X and Z is still there. The spin-orbit coupling, which is small in our compound, lifts some degeneracy of the d -orbitals at Γ point, which is highlighted by the green ellipsoids in the figure. Thus we can conclude that a split of the DOS peak around the Fermi level can solely arise from a structural distortion.

The magnetic crystalline anisotropy, defined as $E_{[100]} - E_{[001]}$, amounts about $5 \mu\text{Hartree/f.u.}$ when $c/a=1.61$ at the equilibrium volume.

The fully relativistic calculation also yields an orbital contribution to the magnetic moment. The calculated total orbital moment and spin moment are $0.037 \mu_B$ and $4.503 \mu_B$, respectively, giving a total moment of $4.545 \mu_B/\text{f.u.}$ in the cubic phase, when the spin quantization axis is in $[001]$ direction. The orbital moment comes mainly from Mn atoms ($0.030 \mu_B$). The tetragonal distortion

increases the orbital moment because of the reduction of the symmetry. At $c/a=1.61$, the total orbital moment is $0.046 \mu_B$, of which $0.043 \mu_B$ is contributed by the Mn atoms.

Chapter 4

Magnetic properties of AFe_2 ($A=Y, Zr, Lu, Hf$) under pressure

4.1 Introduction

In 1898, Charles Edouard Guillaume discovered that the thermal expansion coefficient of Fe-Ni alloys exhibits a sharp minimum with atomic concentration of Ni at around 35 at.%. This particular alloy is called “Invar” alloy because its length is invariant with temperature within a certain temperature region. Guillaume was awarded the Nobel Prize for physics in 1920, “in recognition of the service he has rendered to precision measurements in Physics by his discovery of anomalies in nickel steel alloys”. The Invar effect was proposed to be connected with magnetism because the plateau of the volume expansion starts almost at the Curie temperature below which ordered magnetic moments are established. The reason for the almost zero volume expansion is that the Invar alloy has a spontaneous volume magnetostriction large enough to compensate normal thermal expansions due to lattice vibrations.

It has been found that quite a number of alloys and compounds show large spontaneous volume magnetostriction. The most famous ones are $Fe_{65}Ni_{35}$ and $Fe_{72}Pt_{28}$. These are both Fe-rich ferromagnetic FCC iron alloys. Some of the Laves phase intermetallic compounds of transition metals such as AFe_2 and ACo_2 also show large spontaneous volume magnetostriction. Shiga [31] reported for the first time experimental evidences of the Invar effect in some of the Laves phase intermetallic compounds. The spontaneous volume magnetostriction ω_s in $HfFe_2$ was reported to be 8×10^{-3} , in $ZrFe_2$ 10×10^{-3} , and in YFe_2 to be small and negative. Here the ω_s is defined in terms of the ratio of the equilibrium volumes in the ferromagnetic (FM) and the paramagnetic (PM) state ¹

$$\omega_s = \frac{V(FM) - V(PM)}{V(PM)}. \quad (4.1)$$

¹In experiment the volume of PM states is obtained by extrapolating volume versus temperature curves from high temperatures down to low temperatures ($T=0$).

Table 4.1: The experimental values of the lattice constant (a), magnetic moment (m_s), and Curie temperature (T_c) of AFe_2 ($A=Y, Zr, Hf$, and Lu) compounds.

AFe_2	a (\AA)	m_s (at 4.2K) ($\mu_B/\text{f.u.}$)	T_c (K)
YFe_2	7.363	2.90	545
$ZrFe_2$	7.060	3.14-3.46	625
$HfFe_2$	7.020	3.36	~ 612
$LuFe_2$	7.217	2.97	610

A large spontaneous volume magnetostriction means that the magnetic moment and the lattice constants are strongly coupled. Experimentally this coupling can be clearly seen by measurements, such as hyperfine field measurements [32], X-ray magnetic circular dichroism (XMCD) [33], and nuclear forward scattering (NFS) [34] under pressure.

As proposed to be in the family of Invar, AFe_2 was extensively investigated both experimentally and theoretically. The reported lattice constants, saturation magnetization and Curie temperatures for the four compounds in the C15 Laves phase are listed in Table 4.1. No other stable AFe_2 compounds in the C15 Laves phase at $T = 0$ were reported. Wortmann [35] showed that the hyperfine field decreases to zero at about 40 GPa ($d_{Fe-Fe} \sim 2.37 \text{\AA}$) in $LuFe_2$, and 50 GPa ($d_{Fe-Fe} \sim 2.40 \text{\AA}$) in YFe_2 at room temperature by NFS. At low temperature, the loss of magnetic moments in YFe_2 took place at about 90 GPa ($d_{Fe-Fe} \sim 2.30 \text{\AA}$). The pressure dependence of the hyperfine field (H_0) of YFe_2 and $ZrFe_2$ was measured up to 0.8 GPa by Dumelow [36] by Mössbauer spectroscopy. The values of $d \ln H_0 / dP$ were $-4.2 \pm 0.2 \times 10^{-4} \text{ kbar}^{-1}$ and $-7.3 \pm 0.1 \times 10^{-4} \text{ kbar}^{-1}$ at 4.2 K, respectively, while at room temperature, it is $-8.5 \times 10^{-4} \text{ kbar}^{-1}$ in YFe_2 , as reported by Riedi [37]. It agrees with the calculated values [36] of -8.96 and $-4.88 \times 10^{-4} \text{ kbar}^{-1}$, respectively for these compounds where only the Fermi contact term has been taken into account in the calculation.

Kai [38] measured the magnetic moment of several groups of Fe compounds in the Laves phase, including C14 and C15 phases: group I: TFe_2 , $T=Sc, Ti, Zr, Hf$; group II: RFe_2 , $R=Lu, Tm, Er, Ho, Dy, Tb, Gd$; and group III: M' , $M'Fe_2=Ta, Nb, U, Pu, Ce$ and Sm . A linear relationship between the Fe-Fe distance and the magnetic moment was found in each group. The magnetic moment decreases with the reduction of the Fe-Fe distance. The magnetic moment behavior under pressures of these compounds was reported by Armitage [39]. The pressure dependent magnetization $\frac{\partial \ln \sigma}{\partial P}$ was obtained by the thermodynamic relationship from the measured forced volume magnetostriction $\frac{\partial \ln V}{\partial B}$:

$$\frac{\partial \ln \sigma}{\partial P} = \frac{-40\pi}{\mu_0 M} \left(\frac{\partial \ln V}{\partial B} \right),$$

where σ is the magnetization per unit mass, P is the pressure, V is the volume of the sample, B is the magnetic field, and $\mu_0 M$ is the magnetization per unit volume. The values at $T = 4.2 \text{ K}$ are -8.2 ± 0.4 and $-6.3 \pm 0.3 \times 10^{-4} \text{ kbar}^{-1}$ for YFe_2 and $ZrFe_2$, respectively. This is quite agreeable with the hyperfine field measurements and calculation by Dumelow, which suggests that in these

compounds the hyperfine field at the Fe site is proportional to the magnetization of the compounds. The pressure dependence of the Curie temperature (T_c) of ZrFe₂ was measured by Brouha [40]. The negative dT_c/dP up to hydrostatic pressure of 35 kbar indicated the characteristics of itinerant ferromagnetism. All of these experiments suggest strong magneto-volume couplings in these compounds.

Theoretically, Asano [41] investigated the phase stability by comparing the total energies of different magnetic states (nonmagnetic, ferromagnetic, or antiferromagnetic states) of C14 or C15 Laves phases by LMTO, where the magnetic state refers to the spin arrangement of the iron atoms, and not to the coupling between iron and the other element. They concluded that the ground state of Y, Zr, and Hf compounds are the ferromagnetic C15 Laves phase, which is in agreement with experiments. Yamada [42] has calculated the high field susceptibility χ_{hf} by tight binding approximations. It was found that in ZrFe₂ $\chi_{hf} = 5.8 \times 10^{-4}$ emu/mol, and in YFe₂ $\chi_{hf} = 5.57 \times 10^{-4}$ emu/mol which agree with the experimental values of 6.1×10^{-4} emu/mol, and 1.55×10^{-4} emu/mol in the order of magnitudes. Klein *et al.* [43] discussed the electronic structure, superconductivity, and magnetism in the C15 compounds ZrX₂ (X=V, Fe, and Co). Their results showed that the simplified Stoner theory, which is basically a rigid band model, is quantitatively inaccurate in describing the magnetic properties in stoichiometric and non-stoichiometric compounds because of a significant covalent bonding. This binding mechanism in ZrFe₂ was first proposed by Mohn [44]. The consequence of this binding is that the weights of DOS of the majority and minority electrons changes, rather than only a rigid shift of the two spin subbands as assumed in the Stoner model. Thus reliable conclusions can only be available by full self-consistent calculations. The similar total energy of paramagnetic and ferrimagnetic state, where the magnetic moments of Fe and Zr are antiparallel but do not compensate, at small lattice parameter in the calculation by Mohn [44] indicated that the magnetic moment would collapse in ZrFe₂ under pressure, but no detailed information about the magnetic transition was given there.

In the previous twenty years, a lot of work has been spent on clarifying the magnetic structure of these compounds. One of the main questions is whether the A atom carries a magnetic moment or not. All theoretical calculations gave the same answer that the A atom has a small induced antiparallel magnetic moment because of covalence with iron [44, 45]. But the magnetic form factor of the A atoms might be too small to be detected by scattering methods. Later on, neutron scattering experiments of YFe₂ by Ritter [46] confirmed the theoretical prediction that the Yttrium carries a negative magnetic moment, but no reports about the other compounds.

However, theoretical calculations based on the density functional theory (DFT) to study the pressure effect in these compounds in detail are still not reported according to our best knowledge. The experimental evidence that under high pressures the magnetic moment of YFe₂, HfFe₂, and LuFe₂ collapses, has been reported by Wortmann, as we have mentioned. For ZrFe₂, if we compare the three isostructural compounds: YCo₂, ZrFe₂, and YFe₂, which have 93, 92, and 91 electrons, respectively, YFe₂ is ferromagnetic with magnetic moments about $2.90 \mu_B/f.u.$, while YCo₂ is metamagnetic. If we assume that their electronic structures are similar, it can be expected that the middle compound shows a magnetic deterioration under moderate pressures. Collecting the direct

and indirect magnetic moment information under pressure we may expect to obtain a magnetic transition under pressure in all these four compounds.

The deterioration of the magnetic moment in itinerant systems is universal and can be qualitatively understood with the help of the Stoner model as explained before: In a simplified version of this model, a magnetic state is stable if $IN(E_F) > 1$, where I is the Stoner parameter, which is only weakly dependent on the interatomic distance, while $N(E_F)$, the density of states at the Fermi level, decreases as the band width increases under pressure. Taking Heine's [47] general result that the width of d bands (W) is proportional to R^{-5} , where R is the nearest neighbor atomic distance, the $N(E_F)$ should accordingly decrease with R if we take the rectangular DOS model. At a certain pressure, the Stoner criterion is no longer satisfied, then the system becomes nonmagnetic.

In this chapter, the magnetic moment behavior of the four ordered stoichiometric compounds (YFe_2 , ZrFe_2 , LuFe_2 , and HfFe_2) in the cubic Laves phase are investigated by density functional calculations. The main problems we are going to address are the order of the quantum magnetic phase transition at high pressures and the related Invar effect. Two of them (ZrFe_2 and HfFe_2) were reported to show Invar anomaly, while the other two were not. A natural question would be: What is the difference between them? Partial answers to these questions are provided by our density functional calculations. Additionally, non-stoichiometric compounds of $\text{Zr}_x\text{Fe}_{1-x}$ is studied in order to understand the volume and magnetic moment trend with respect to doping in the homogenous region.

4.2 Computational parameters

The space group of the cubic Laves phase is $\text{Fd}\bar{3}\text{m}$ (C15 phase). It consists of two formula units in the conventional unit cell (u.c.). The A atom occupies the Wyckoff position 8a: $(\frac{1}{8}, \frac{1}{8}, \frac{1}{8})$, and Fe is at 16d: $(\frac{1}{2}, \frac{1}{2}, \frac{1}{2})$, as shown in Figure 4.1. The LSDA exchange correlation functional chosen is parameterized

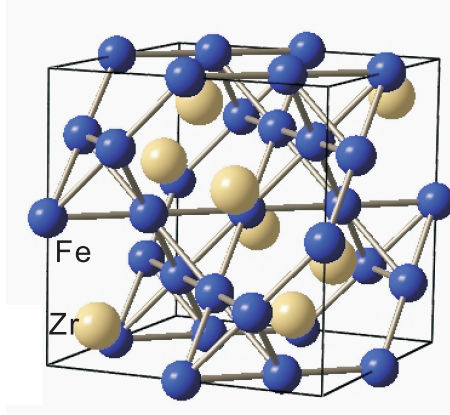


Figure 4.1: The unit cell of the cubic Laves phase (C15). The Fe atoms form a pyrochlore sublattice as shown by the bonds between Fe's.

by Perdew and Wang [7]. The number of k-points in the irreducible part of the

Brillouin zone (IBZ) is 897 if not specified in the context. The valence basis states are Fe: $3sp/3d4sp + 4d$, Zr and Y: $3d4sp/4d5sp$, Lu: $4f4d5sp/5d6sp$ and Hf: $4d5sp/5d6sp$, respectively.

4.3 Fixed spin moment schemes

In order to probe possible local minima of the total energy with respect to the spin moment, a fixed spin moment (FSM) scheme was proposed by Schwarz and Mohn [48]. In this scheme, the total spin moment M is fixed. In general, the number of valence electrons Z_{val} and the spin moment M per unit cell are given by:

$$Z_{val} = N^{\uparrow} + N^{\downarrow} = \int_{-\infty}^{E_F^{\uparrow}} D^{\uparrow}(E) dE + \int_{-\infty}^{E_F^{\downarrow}} D^{\downarrow}(E) dE \quad (4.2)$$

$$M = N^{\uparrow} - N^{\downarrow} = \int_{-\infty}^{E_F^{\uparrow}} D^{\uparrow}(E) dE - \int_{-\infty}^{E_F^{\downarrow}} D^{\downarrow}(E) dE \quad (4.3)$$

where the $D^{\uparrow}(E)$ and $D^{\downarrow}(E)$ are the densities of states for majority and minority spins, respectively. The variable $N^{\uparrow(\downarrow)}$ is the total number of spin up (down) electrons. We can take the M as a parameter. Then the Fermi levels of the up and down spins $E_F^{\uparrow(\downarrow)}$ are determined by the equations above. Their difference corresponds to the Zeeman energy with respect to a fictitious applied magnetic field. By this constraint search, we are able to evaluate the total energy (E) of the ground state as a function of M together with some other thermodynamic variables such as V (volume): $E = E(M, V, \dots)$. In reality, for a fixed volume, we might obtain several energy minima as a function of M . As a function of volumes, the local minimum might change its positions, disappear or appear. This gives complicate magnetic behaviors of the system under pressure [12]. In summary, the FSM scheme provides us an additional freedom to explore the phase space. Interesting physics such as metamagnetism can be discussed on the basis of this scheme [49].

4.4 Ground state properties of AFe₂

Although the magnetic moments of A and Fe are ferrimagnetically coupled, we still use the terminology FM to indicate the state where the Fe sublattice has a finite parallel spin moment. The calculated lattice constants in FM (a_{FM}) and NM (a_{NM}) states, total spin moment (m_0) at the theoretical equilibrium lattice constant (a_{FM}) and that (m_{exp}) at the experimental lattice constant are listed in Table 4.2. Comparing with the experimental parameters shown in Table 4.1, we can state that the results are in good agreement with the experiments within the error bar of the LSDA. The use of LSDA results in an underestimation of the lattice constants by about 3% for $3d$ transition metals. The relatively large underestimation of the magnetic spin moment if we use the theoretical equilibrium lattice parameter results from the sensitivity of the moment with respect to the lattice constant as we will see in the following discussions.

4.4.1 Common features of the electronic structure

The DOS of the four compounds, evaluated at the respective theoretical equilibrium lattice constants (a_{FM} in Table 4.2), are shown in Figure 4.2. Common

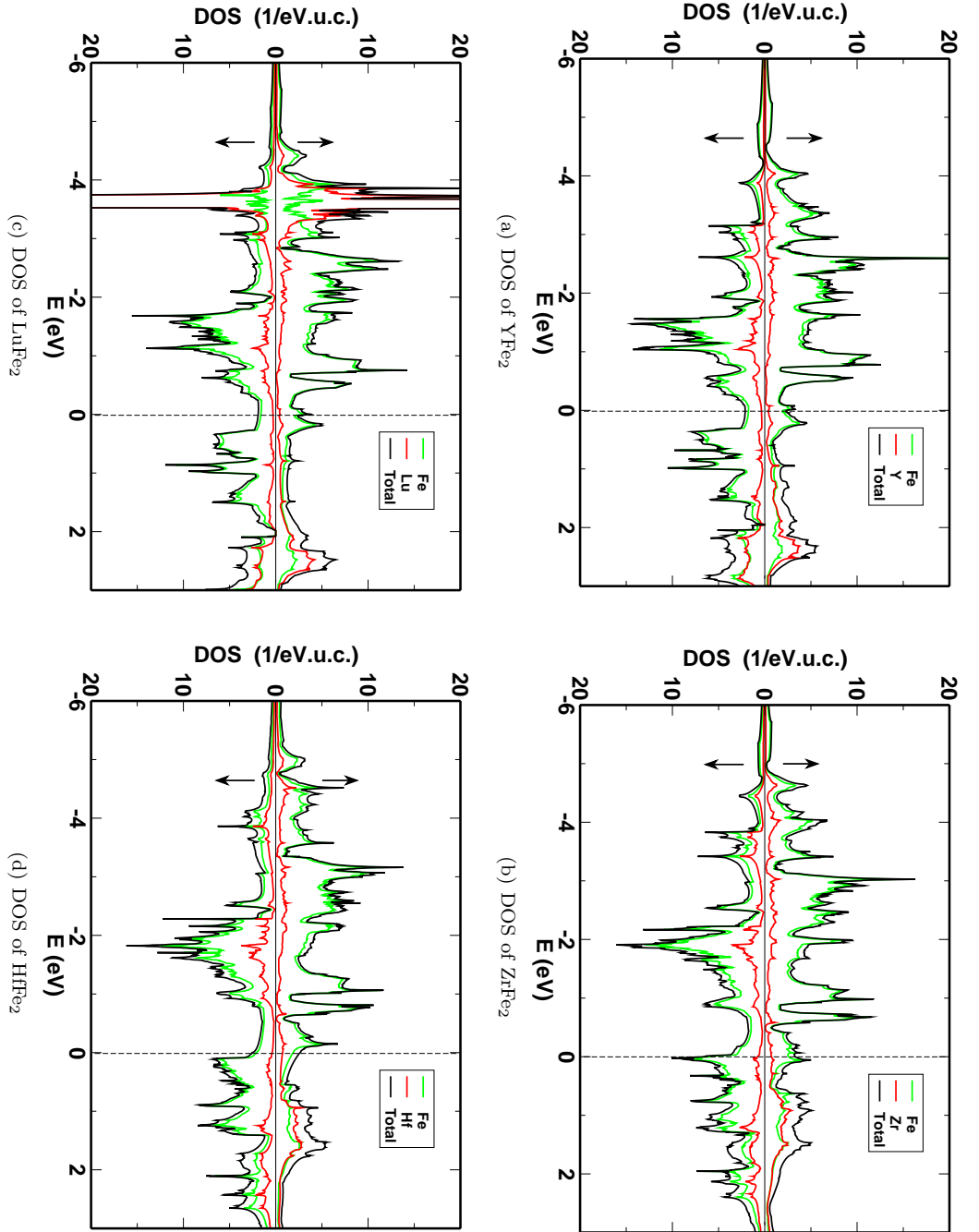


Figure 4.2: DOS of $A\text{Fe}_2$ ($A=\text{Y}$, Zr , Hf , and Lu) at the respective equilibrium volumes. The vertical dashed lines indicate the Fermi level.

Table 4.2: The calculated lattice constants a_{FM} in FM state and a_{NM} in NM state, total spin magnetic moments (m_0) at a_{FM} and that (m_{exp}) at experimental lattice constants of the four compounds. The numerical accuracy of the lattice constant is within ± 0.002 Å.

AFe ₂	a_{FM} (Å)	a_{NM} (Å)	m_0 (μ_B /f.u.)	m_{exp} (μ_B /f.u.)
YFe ₂	7.040	6.927	2.57	3.10
ZrFe ₂	6.838	6.771	2.38	3.14
HfFe ₂	6.824	6.746	2.86	3.17
LuFe ₂	6.931	6.874	2.53	2.95

features of these DOS are quite obvious: they are highly peaked although the distance between the nearest neighbors of irons is small, for example $d_{Fe-Fe} \sim 4.56$ a.u. in the ZrFe₂ compared with $d_{Fe-Fe} \sim 4.69$ a.u. in BCC Fe. Just above the Fermi energy, there is a relatively high DOS in the minority spin channel. This feature is dominated by anti-bonding $3d$ states of Fe. The bonding and antibonding states of the minority spin channel are separated by a deep and wide valley with a width of about 1 eV. The zoomed-in band structure and the DOS of the minority states in ZrFe₂ are shown in Figure 4.3. The peak in the minority states just above the Fermi level comes from almost non-dispersive states. This energy range is highlighted by the rectangular block with height of 0.06 eV. The high DOS around the peak stems from the narrow bands in the directions along $W-K$ and $W-U$. Because of the similarity of the electronic

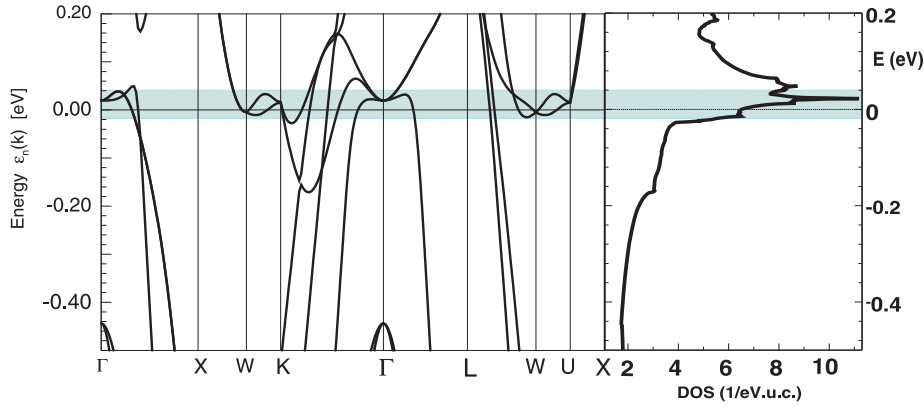


Figure 4.3: The band structure and the DOS of the minority spin channel of ZrFe₂ at the theoretical equilibrium lattice constant. The rectangular block with height of 0.06 eV indicates the energy window around the pronounced DOS.

structure in these four compounds only the bands and the DOS of ZrFe₂ are shown here.

The van Hove singularity just above the Fermi level in the spin down channel is closely related to the magnetic properties which we are going to discuss, so we explore the origin of it here. It was long realized that the Fe atoms in the C15 Laves phase form a so-called pyrochlore structure with corner shared

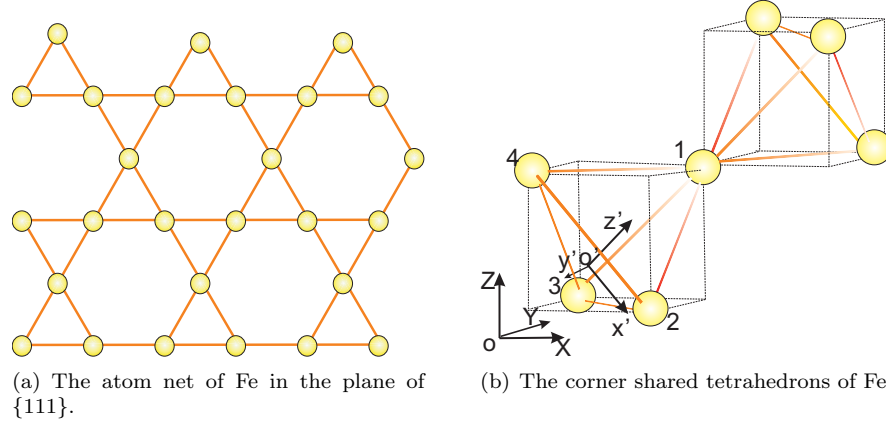


Figure 4.4: The Kagomé net of Fe (a) and the corner shared tetrahedrons (b) of the Pyrochlore net. The O-XYZ is the global coordinate system, and $o' - x'y'z'$ is the local coordinate system used to project the partial DOS in a trigonal lattice.

tetrahedrons as shown in Figure 4.1. If we look at the net in the $\{111\}$ layer, it is a Kagomé net with alternatingly connected triangles and hexagons as shown in Figure 4.4(a). As already shown by Johnston and Hoffmann [50], the high peaks in the DOS in a Kagomé net of iron atoms come from narrow bands with $d - \pi$ character. One band tight binding model calculation by Isoda [51] discovers two non-dispersive degenerated states along the $X - W$ line. Further, there are two additional non-dispersive degenerated antibonding states along all high symmetry directions. These results indicate that the spiking DOS is closely related to the topology of the nets.

If we plot the m_l -resolved “fat” band and the partial DOS (PDOS) of Fe as shown in Figure 4.5, it is clear that at Γ -point the states with $m_l=0$ (d_{z^2}) and 2 ($d_{x^2-y^2}$) are degenerate and $m_l=-2$ (d_{xy}), -1 (d_{yz}), and 1 (d_{xz}) are also degenerate. These two groups are denoted by “ E_g ”, and “ T_{2g} ”, respectively. But they are not the irreducible representation of the cubic symmetry, because the site symmetry of Fe is D_{3d} . It can be shown that the PDOS is divided into two catalogues: One is the three d orbitals ($m_l=-2, -1$, and 1) and the other is two d orbitals ($m_l=0, 2$) if we choose the coordinates as in Figure 4.4, but the dispersions are different. It is shown that the strongest van Hove singularity in the PDOS just above the Fermi level of the minority spin state is solely from the “ T_{2g} ” states. From the “fat” band, it can be observed that the states at the Γ point are mainly contributed from the “ T_{2g} ” state. It is quite understandable because the “ T_{2g} ” states form quite strong π binding states along each atomic chain with nearest neighbor interactions. For example, the d_{xy} orbitals from Fe_1^2 and Fe_4 , or Fe_2 and Fe_3 form π -orbitals. The antibonding state of these π orbitals is the source of the quite spiking feature of the DOS in the cubic Laves phase compounds as analyzed by Johnston and Hoffman [50]. From another point of view, if we rotate the coordinates and put the z-direction to the diagonal direction of the cube as shown in Figure 4.4 (b), then the lattice

²Atoms are numbered as in Figure 4.4(b).

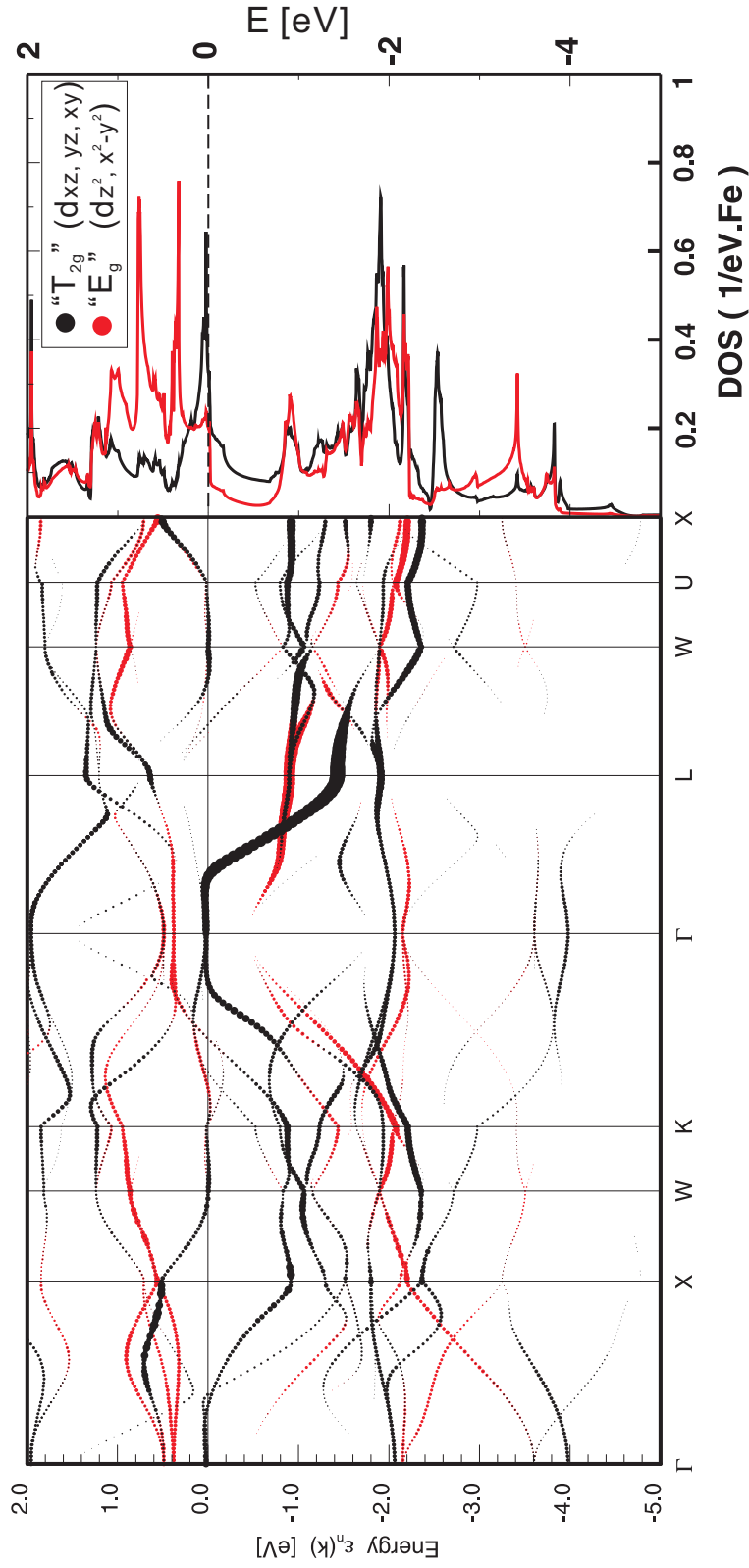


Figure 4.5: The “fat” band and PDOS of the minority d-state of Fe in ZrFe_2 . The “ T_{2g} ” states are from states with $m_l = -2, -1$ and 1 , while the “ E_g ” states are from $m_l = 0$ and 2 .

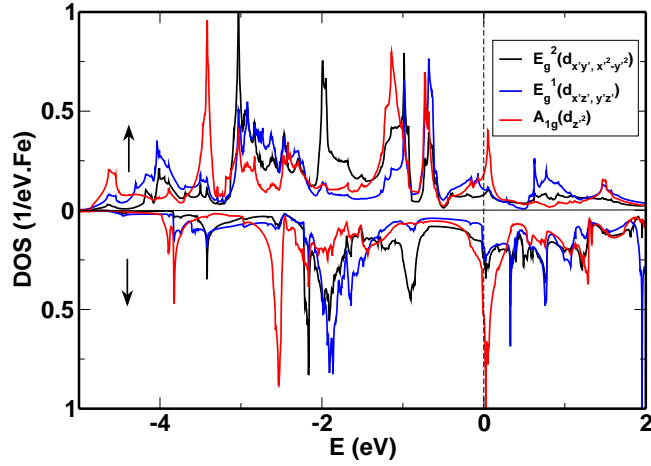


Figure 4.6: PDOS of Fe resolved into the irreducible representation (A_{1g} and $E_g^{1,2}$) of the point group D_{3d} .

can be described by a trigonal lattice. The point group of the atom on the new z -axis (Fe_1) is D_{3d} . There is a one dimensional irreducible representation A_{1g} with basis of d_{z^2} . It turns out that the d_{z^2} orbital comes solely from the “ T_{2g} ” orbitals. As discussed by Isoda [51] by single orbital tight binding calculations, which is a one dimensional representation, the antibonding orbitals are non-dispersive in all high symmetric directions of the BZ. This implies that the one dimensional representation with d_{z^2} orbitals as its basis should give also quite spiking feature in the DOS. This is evident if we plot the PDOS resolved into the irreducible representation of D_{3d} as shown in Figure 4.6.

Hybridization between the states of the Fe and A atoms in this cubic Laves phase was extensively studied by several authors, e.g. Kübler [28], and Brooks [45]. The covalent bonding scenario was generally accepted in order to explain the ferrimagnetic coupling between the iron atom and the A atoms. The model density of states shown in Figure 4.7 depicts this process. The atomic iron d states are spin polarized and the A atoms are not. The split $3d$ states are much lower in energy than the $4d$ or $5d$ of the A atoms (The atomic eigenenergy of the d states are $\epsilon_d^{Fe} \sim -16.54$ eV, $\epsilon_d^Y \sim -6.80$ eV, $\epsilon_d^{Zr} \sim -8.46$ eV, $\epsilon_d^{Lu} \sim -6.63$ eV and $\epsilon_d^{Hf} \sim -8.14$ eV) [52]. When they form a bond, because the energy of the majority $3d$ states is about 2 eV lower than that of the minority $3d$ states by the exchange splitting, the hybridization between the $3d$ and $4(5)d$ majority states is weaker than between the minority states. By covalency charges transfer more from the majority spin state of A atom to Fe than from the minority spin state. Thus the minority $4(5)d$ states become more occupied than the majority states. In this way the magnetic moments of the A atoms are antiparallel to the Fe. This covalent interaction between A and Fe explains the antiparallel coupling between the spin moments of the two elements in the compounds.

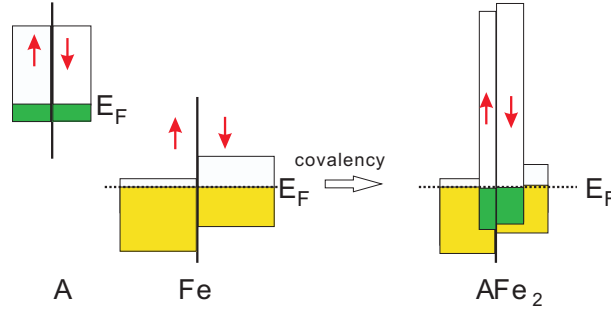


Figure 4.7: Model DOS of the d states of A and Fe before and after hybridization. The green blocks show the occupied states of the A atoms while the yellow is of the Fe . The red arrows (up and down) indicate the majority and minority spin of the electrons.

4.4.2 Specific electronic structures and magnetic moment behavior

Because of the differences of the A atoms, we can naturally expect some differences among these compounds. Firstly the lattice constants of these materials are more or less determined by the atomic volume of A . Taking the atomic volume, defined by (atomic weight/mass density), of the elements: $Y=19.89$, $Zr=14.06$, $Lu=17.78$, and $Hf=13.41$ (cm^3/mol), respectively [53], we can see that the lattice constants in Table 4.2 follows the same tendency.

Secondly their magnetic moments have different behaviors under pressure. The dependence of the magnetic moment on lattice parameters are shown in Figure 4.8. The corresponding hydrostatic pressures are shown on the upper abscissas. Obviously all of them show a decrease of the magnetic moment with the decrease of the lattice constant as expected from the itinerant electron magnetism, but the Hf and Zr compounds show a more rapid decrease of the moment at a lattice constant around 6.8 \AA (in the vicinity of the equilibrium lattice constant), while the other two show a gradual decrease at this low pressure. At high pressure, all four compounds show at least one first order transition to a lower or zero spin state. The differences are quite understandable by examining the differences of the electron numbers of the compounds under the assumption that the electronic structure is not so much influenced by the difference of the A atoms. YFe_2 , $ZrFe_2$, $HfFe_2$, and $LuFe_2$ show basically similar DOS as discussed before. The difference of the electron number shifts the Fermi level in these systems. $Zr(4d^2)$ and $Hf(5d^2)$ have one more d -electron than $Y(4d^1)$ and $Lu(5d^1)$, so the Fermi levels of the former are shifted towards higher energy, situating closer to the pronounced peak of the minority spin DOS as shown in Figure 4.2. This accounts for the low pressure instability of the moment.

The four compounds show multi-step magnetic transitions. This process can be understood by the particular DOS of these compounds. Taking $ZrFe_2$ as an example, the DOS at different lattice constants are shown in Figure 4.9 (a~d). The lattice constants of each figure are indicated by the arrows in Figure 4.8(b) with the corresponding labels of (a), (b), (c), and (d). From the Figure 4.9(a), it is obvious that at the experimental lattice constant the DOS of the up spin, contributed mainly from the iron, has a gradual increase below the Fermi level,

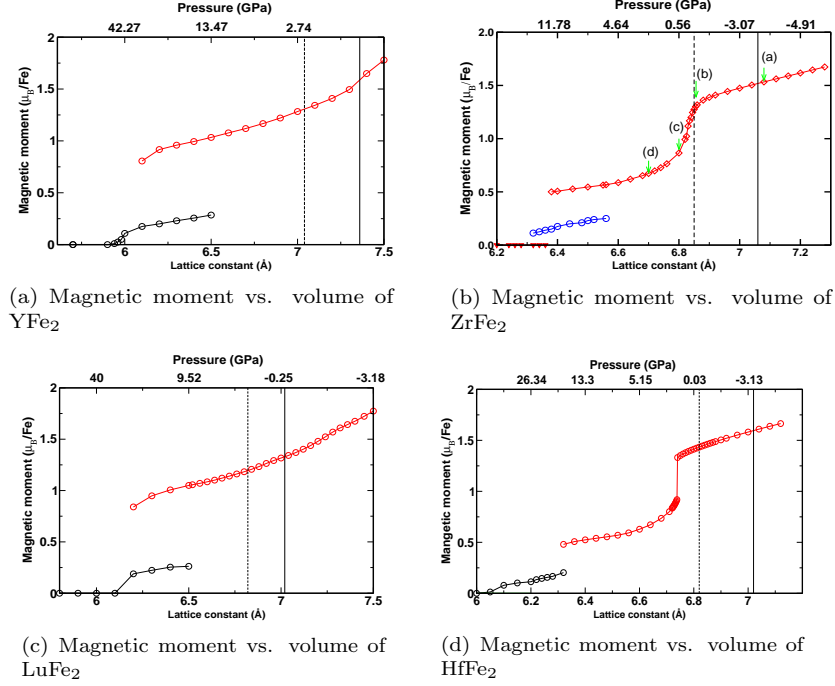


Figure 4.8: Magnetic moment behaviors of AFe_2 ($\text{A}=\text{Y}, \text{Zr}, \text{Lu}, \text{Hf}$) under hydrostatic pressures. The experimental and the theoretical equilibrium lattice constants are shown by the solid and dotted vertical lines respectively. The pressure at the corresponding lattice parameters is shown on the upper abscissas of each figures. These theoretical pressures are obtained from the high spin state. The labels (a), (b), (c), and (d) in figure (b) marks the positions where we show the DOS in Figure 4.9.

while the DOS of the down spin has a wide (~ 0.8 eV) dip below and a sharp increase just above E_F . Applying pressure will broaden the band and reduce the width of the dip and decrease the magnetic moment. Thus the exchange splitting is reduced. The DOS of the up spin and down spin moves towards each other. This gradual decrease of the magnetic moment is shown in Figure 4.8(b) between the arrows (a) and (b). The gradual decrease of the magnetic moment continues until the Fermi level passes through the high DOS peak of the minority spins, see Figure 4.9(b) and (c). Then the magnetic moment is rapidly reduced, as shown in Figure 4.8(b) when the lattice constant is between 6.85 (arrow (b)) and 6.80 (arrow (c)) Å. If we take the rigid band model [54, 55] and assume that the band width W and the interatomic distance R follow Heine's model $W \times R^5 = \text{constant}$ [47], the magnetic moment variation under the change of volumes is directly related to the averaged DOS at the Fermi level by

$$\frac{V}{M} \left[\frac{\partial M}{\partial V} \right]_{H=0} = \frac{5}{3} \frac{I}{N_{eff}^{-1} - I}, \quad (4.4)$$

where

$$N_{eff}^{-1} = \frac{1}{2} (1/N_+ + 1/N_-), \quad (4.5)$$

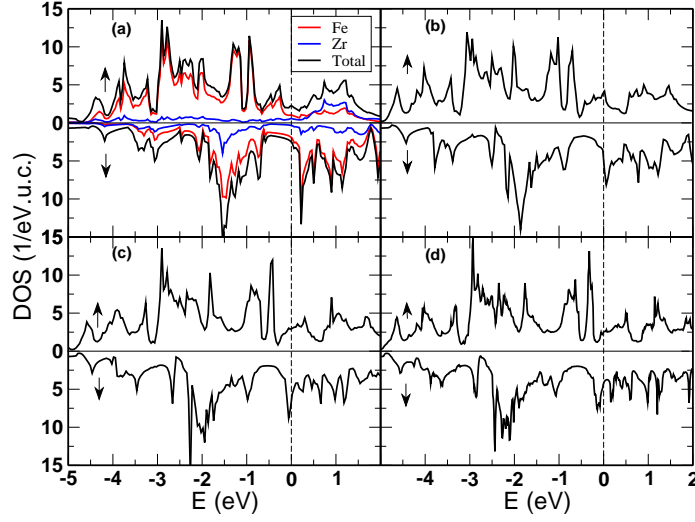


Figure 4.9: The total DOS and partial DOS of ZrFe_2 at different lattice constants. From (a) to (d), the lattice constants are 7.08, 6.85, 6.80, and 6.70 Å, respectively. In (a), the partial DOS of Fe and Zr are also shown. The Fermi level is indicated by the dashed vertical line at $E=0$ eV.

and I is the Stoner parameter, $N_{+(-)}$ is the DOS at Fermi level of the spin up (down), and M , V are the magnetic moment and the volume of the sample respectively. From this, we can see, the larger the average DOS (the Fermi level around the peaks), the more rapidly the magnetic moment varies.

The occurrence of an intermediate magnetic solution in ZrFe_2 at lattice constant between 6.32 and 6.58 Å is due to the details of the DOS. It is impossible to give an argument without calculations, but one thing is essential: narrow peaks form around the Fermi level, so that multiple magnetic solutions can exist [56], and this has been discussed in our previous introduction to the Stoner model. In this range of lattice parameters, the material becomes weakly ferromagnetic, with rather small magnetic moments: $0.25 \mu_B/\text{Fe}$. Further compression will suppress the magnetism. A question arises whether the transition is first order or second order. This transition can also be induced by doping. For example, in a recent experiment on $\text{Hf}(\text{Fe}_{1-x}\text{Co}_x)_2$ by Amako [57] a collapse of the ferromagnetic moment has been observed between $x=0.6$ and 0.65 . Further, the doping can tune the pressure dependence of the Curie temperature (T_c), and induce a transition from the ferromagnetic state to the metamagnetic state. We postpone the detailed discussions to the following section. From the experimental point of view, the interesting point here is that the transition pressure is in the laboratory accessible range (tens of GPa), see Figure 4.8.

4.4.3 The order of the magnetic transition under high pressure

We can see from the previous figures (Figure 4.8) that under moderate pressure (tens of GPa), there is a finite small magnetic moment in these compounds. With further increase of pressure, the magnetic moment eventually becomes

zero. The transition of the magnetic moment can be either a first order (a discontinuous transition) or a second order (a continuous transition). The free energy (E) landscape at $T = 0$ of first and second order phase transition is schematically illustrated in Figure 4.10. This different behavior when approach-

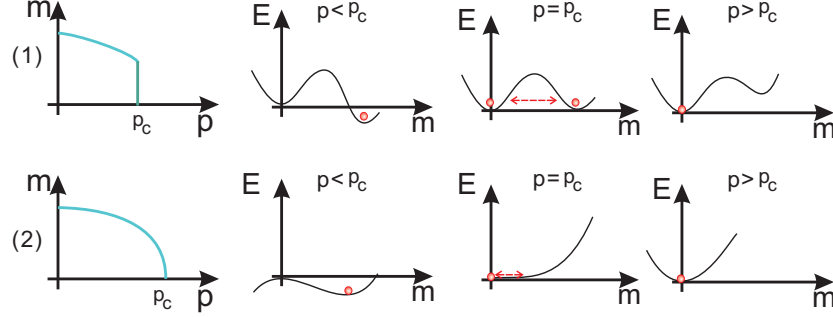


Figure 4.10: Qualitative illustration of first order (1) and second order (2) transitions of the magnetic moment (m) under pressures, and their corresponding free energy (E), respectively, adapted from Pfeleiderer [58].

ing the quantum phase transition can be of interest both experimentally and theoretically. For the second order phase transition, the effect of fluctuation was shown to lead to novel electronic ground states in magnetic metals such as magnetically mediated superconductivity, partial or quadrupolar order and non-Fermi liquid phases. For the first order phase transition, as summarized by Pfeleiderer [58], it is interesting for a number of reasons: It can drive novel electronic states, novel types of low lying excitations, or signal the existence of subtle quantum correlation effects. In general, peaks of DOS (van Hove singularities) near the Fermi level in all real materials result in a ragged free energy landscape. The topology of the DOS thus has a connection with the order of the quantum phase transition. It is necessary to give some hints about the order of the transition based on our calculations of electronic structures. Take the simplified Stoner model, the magnetic free energy of the system in the rigid band model is expressed by [59]

$$E(m) = \int_0^m \Delta\xi(m') dm' - \frac{1}{4} I m^2, \quad (4.6)$$

where $\Delta\xi(m)$ is exchange splitting as a function of magnetic moments m , and I is the Stoner parameter. The $\Delta\xi(m)$ can be expanded as a power series of m :

$$\Delta\xi(m) = a_1 m + a_3 m^3 + a_5 m^5 \dots \quad (4.7)$$

where

$$a_1 = \frac{1}{2} \bar{N}_1^{-1} \quad (4.8)$$

$$a_3 = \frac{1}{3} (3 \bar{N}_2^2 \bar{N}_1^{-5} - \bar{N}_3 \bar{N}_1^{-4}) \quad (4.9)$$

$$a_5 = \frac{2}{5!} (105 \bar{N}_2^4 \bar{N}_1^{-9} - 105 \bar{N}_3 \bar{N}_2^2 \bar{N}_1^{-8} + 10 \bar{N}_3^2 \bar{N}_1^{-7} + 15 \bar{N}_4 \bar{N}_2 \bar{N}_1^{-7} - \bar{N}_5 \bar{N}_1^{-6}). \quad (4.10)$$

\bar{N}_i is defined as the $(i - 1)$ -th order derivative of the density of states at the Fermi level with respect to the energy ³.

Then the free energy is

$$E(m) = \frac{1}{2}(a_1 - \frac{I}{2})m^2 + \frac{1}{4}a_3m^4 + \frac{1}{6}a_5m^6 \dots \quad (4.11)$$

The stability of the phase can be discussed in line with Landau's theory of second order phase transitions. Magnetic instability is necessarily given by the condition that $a'_1 = a_1 - \frac{I}{2} \leq 0$, which is equivalent to the Stoner criterion $IN(E_F) \geq 1$ by considering Equ. (4.8).

The necessary condition to have a first order transition is $a_1 - I > 0$, $a_3 < 0$, and $a_5 > 0$ ⁴ if higher order terms than m^5 are neglected in Equation (4.11). This means the DOS at the Fermi level should be sufficiently small (the Stoner criterion is not fully satisfied) and the curvature of the DOS at E_F is positive and large, so that \bar{N}_3 is positive and large enough to give negative a_3 , otherwise, if $\bar{N}_3 < 0$, a_3 is definitely positive. These first two conditions require that the Fermi level is at a narrow valley of the DOS.

Let us replace this qualitative analysis by direct FSM calculation results and the corresponding DOS to analyze the transition. The first example is ZrFe₂, which shows a first order transition to the non-magnetic state. The FSM energy curves are shown in Figure 4.11 at lattice constants around the transition point. The $E(m)$ curve at $a=6.30$ Å is enlarged in the inset. It clearly shows two energy

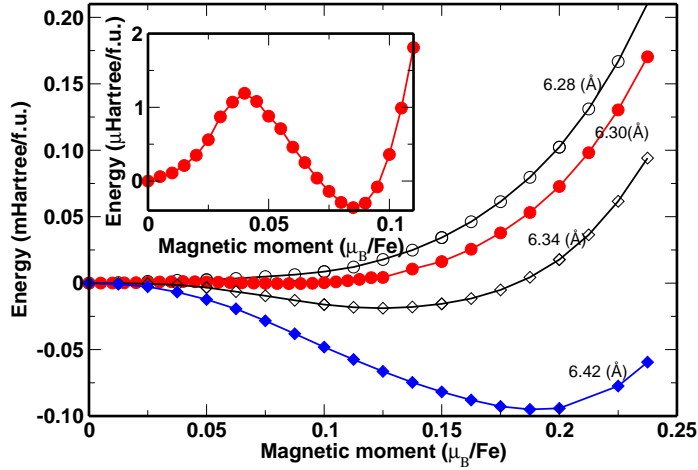


Figure 4.11: The FSM curves of ZrFe₂ at the lattice constants around 6.30 Å. The inset shows the enlarged curve at the lattice constant $a=6.30$ Å. It clearly shows that magnetic and nonmagnetic solutions coexist at this lattice constant. The data in this figure are obtained with 3107 k-points in the IBZ.

minima at $m=0$ and $m=0.085 \mu_B/\text{Fe}$. The DOS of the related nonmagnetic and magnetic solutions is shown in Figure 4.12. It is clear that the Fermi level (the

³This is just the Taylor's expansion of Equation (2.53) in Chapter 2. This analytic description breaks down if the van Hove singularity crosses the Fermi level.

⁴ a_5 or some higher a_n should always be positive in order to have a finite moment solution, although it is difficult to determine the sign of it by the topology of the DOS.

dashed vertical line in the figure) is at a dip (between two peaks marked by two ellipses) of the nonmagnetic DOS. In the magnetic solution, the two subbands are shifted against each other as shown by the dashed horizontal arrows.

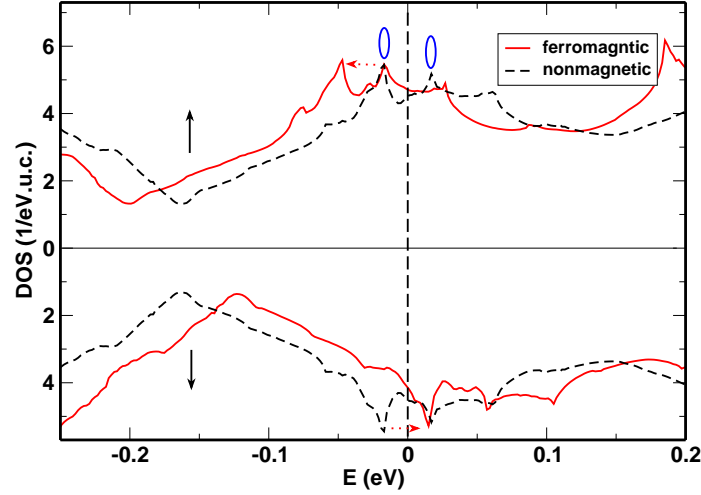


Figure 4.12: The DOS of nonmagnetic state (dashed lines) and ferromagnetic state (red lines) of ZrFe_2 at $a=6.30$ Å. The horizontal dashed arrows show the relative shift of the DOS of the up and down spin subbands. The two ellipses indicate the two peaks around the Fermi level which cause the first order magnetic transition.

The other example is YFe_2 where the magnetic transition is of second order. The FSM curves are shown in Figure 4.13. The energy minimum moves to zero when compressing the lattice as shown in the figure. The energy curve at $a=5.99$ Å is zoomed in and shown in the inset. The FSM energy difference for small magnetic moments reaches the accuracy limit guaranteed by the code. This is the reason that we should resort to the DOS in order to discuss the possible magnetic solutions. The DOS of nonmagnetic and ferromagnetic states are shown in Figure 4.14. It is clear that the “valley” character around the Fermi level is missing compared with Figure 4.12. Rather, E_F is situated at a plateau which can not have more than one magnetic solutions. The other two compounds, LuFe_2 and HfFe_2 show a similar second order transition.

Thus in the Y, Hf and Lu compounds, we obtain a second order quantum phase transition (QPT), but in the Zr compound, we obtain a first order QPT. It will be quite interesting for the experimentalist to perform high pressure (tens of GPa) measurements, comparing the magnetic and transport properties in this series of compounds. It can help to reveal the analogies and differences in the QPT.

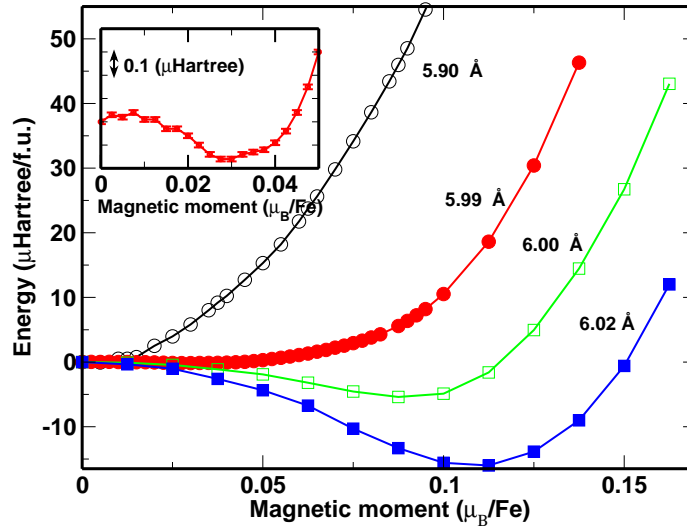


Figure 4.13: The FSM energy of YFe_2 at lattice constants around $a=6.00$ Å. The inset shows the zoomed-in curve at the lattice constant of 5.99 Å with an error bar of 0.01 $\mu\text{Hartree}$. The data in this figure are obtained with 8797 k-points in the IBZ.

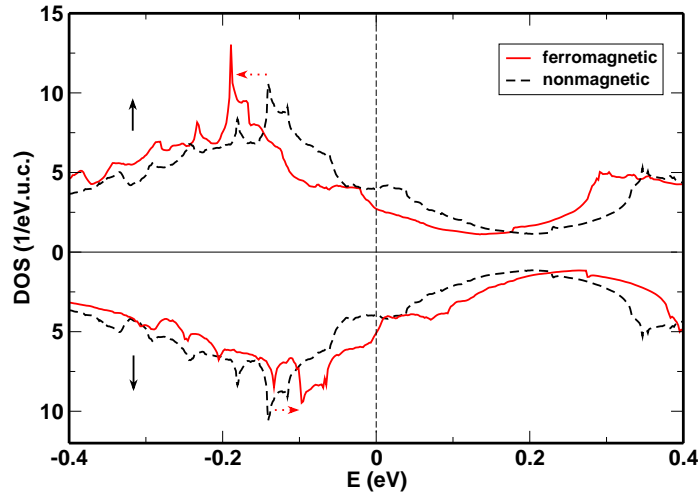


Figure 4.14: The DOS of the nonmagnetic state (dashed lines) and the ferromagnetic state (solid lines) of YFe_2 at $a=5.99$ Å. The horizontal dashed arrows show the relative shift of the DOS of the up and down spin subbands. The Fermi level is shown by the vertical dashed line.

4.5 Relationship between Invar behavior and magnetic transitions

Invar alloys have their importance in modern industry, especially in precise instruments. The inventor Ch. E. Guillaume was awarded the Nobel prize in

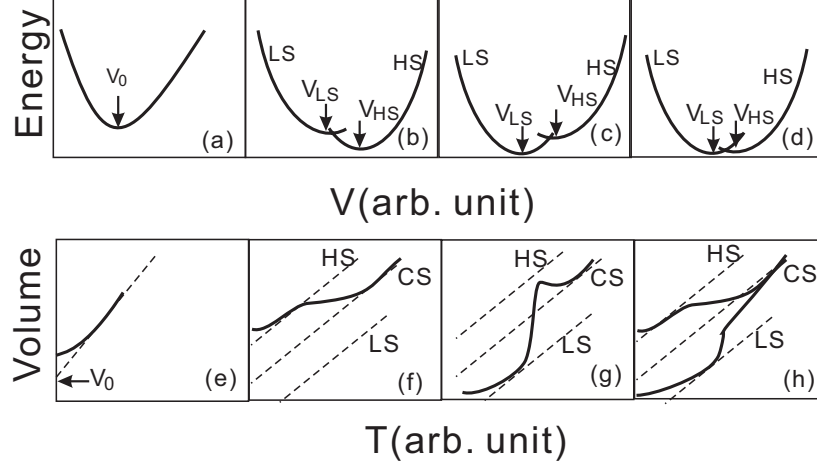


Figure 4.15: A schematic illustration of the 2γ -model. (a) is for simple metal, (b) an Invar system, (c) an anti-Invar system, and (d) a spin glass state. The corresponding volume vs. temperature behaviors are shown in (e), (f), (g), and (h). V_0 , $V_{LS, (HS)}$ denote the equilibrium volume for normal metal, LS (HS) states. CS refers to the composite LS and HS behaviors. This figure is adapted from Moruzzi [61].

physics in 1920. Understanding the Invar effect, however, has been a problem for a half of the century. More than twenty different models have been published in the past 50 years for the explanation of the Invar effect. A general review about the Invar effect can be found, for example, in handbooks edited by Buschow and Wohlfarth [56], and references therein. One model called 2γ -model [60] is based on the hypothesis of Weiss that there exist two separated energy minima with different volumes and magnetic states: HS-high-volume and LS-low-volume states. Here we introduce this model qualitatively and extend this model a little bit to include all possible relative energy minima of the two states. The binding curves of the two states are schematically shown in the upper panel in Figure 4.15 together with the corresponding thermal expansion curves in the lower panel. In Figure 4.15(a) nonmagnetic metal binding curves in a rigid lattice is shown. When the temperature dependent lattice vibration is included, we have the volume versus temperature curve in (e). At high temperatures, the thermal volume expansion coefficient is a constant. When extrapolating to $T = 0$, it derives from linearity. When there are two magnetic states (HS and LS) in the binding curves, with slightly different energy minima, we can expect Invar or anti-Invar effect depending on which brunch is lower in energy. If the energy minimum of the LS state is slightly higher than that of the HS state as in (b), we have the volume versus temperature curve like (f). At low temperature, the HS state with larger volume is the ground state. Increase of the temperature will excite the state into LS state. Because this state has a lower volume, the thermal expansion of the volume is compensated. Thus a plateau in the volume versus temperature curve is developed. This is the Invar effect in the Weiss' 2γ - model. The energy difference was found to be 0.0355 eV for $\gamma - Fe$ [60]. If the HS state and LS state have the binding curves with reversed energy minima

order like (c), the thermal expansion is expected to be enhanced as shown in (g). This is called anti-Invar. If the minima of the energy in the LS and HS are degenerate, the system then consists of a matrix of droplets with very different magnetic behaviors and with large internal stresses at the droplet boundaries. Such a system might show a spin-glass behavior.

First principle calculations for Fe₃Ni by Entel [62] and other authors supported the 2 γ -model. Entel argued that the special position of the Fermi level in the minority band, being at the crossover between nonbonding and antibonding states, is responsible for the tendency of most Invar systems to undergo a martensitic phase transition. Two minima binding curves should lead to some discontinuity (a first order transition) in the pressure dependence of some physical properties, such as volume, magnetic moment *etc.*, but this kind of discontinuity has never been observed in Invar alloys. This gives an obstacle in applying the 2 γ -model to explain the Invar effect.

The HS-LS transition can also be continuous and it is in the Invar alloy like ZrFe₂ and HfFe₂ as in Figure 4.8, according to our LSDA calculation. This point can be illustrated by our FSM calculations. In the FSM energy curves, the energy minimum shifts to the lower magnetic moments as the lattice constant is decreased as in Figure 4.16. Here the FSM energy curves of ZrFe₂ is taken as an example. The quite flat FSM energy curves, which means a large spin susceptibility, near the transition region are because that the average DOS at the Fermi level, defined in Equ. (4.5), is large. The reciprocal susceptibility, $\chi_M^{-1} = E''(M)$, is given by a simple formula [49]

$$\chi_M^{-1} = \mu_B^{-2}(2N_{eff}^{-1} - I), \quad (4.12)$$

where I is the Stoner parameter. Thermal excitations cause loss of the magnetic

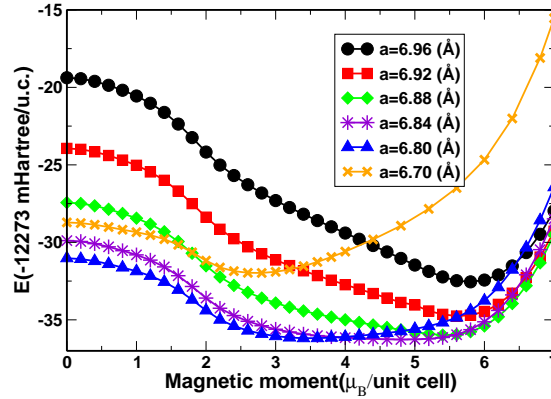


Figure 4.16: The FSM energy curves of ZrFe₂ near the HS-LS transition regions.

moment leading to a magnetic transition from the HS state to the LS state. Therefore, increasing the temperature leads to a gradual loss of the spontaneous volume expansion associated with the ferromagnetic state. This gradual process, contrary to the two states (HS and LS) in some Invar alloy (e.g. Fe₃Ni), will not cause any discontinuity in the pressure dependence of physical properties.

The spontaneous volume magnetostriction is calculated by Equation (4.1). The volumes of different magnetic states are provided in Table 4.2. The results

are listed in Table 4.3, together with the experimental data available [31]. The theoretical values agree with the experimental ones in the sense that they are at the same order. The overshooting of the spontaneous volume magnetostriction

Table 4.3: The spontaneous volume magnetostriction from our LSDA calculations (ω_s) and experiments (ω_s^{exp}).

AFe ₂	ω_s (10 ⁻³)	ω_s^{exp} (10 ⁻³)
YFe ₂	27	-
ZrFe ₂	31	10
HfFe ₂	35	8
LuFe ₂	25	-

(ω_s) can partly be from the non-vanishing local magnetic moment above the transition temperature in the experiments, while in our model it is in a Pauli paramagnetic state where the spin moment is zero. The cure for this problem requires a more realistic treatment of the paramagnetic phase. It has been shown that a noncollinear [63] or a disordered local moment (DLM) [64, 65] model gives a better agreement with the experiments. Nevertheless, the results presented here show the major characteristics of Invar alloy: Compared with the compounds where no Invar anomaly is observed, the ω_s is larger. In typical Invar alloy, such as Ni₃₅Fe₆₅ and Fe₇₂Pt₂₈, $\omega_s(10^{-3}) = 18$ and 14.4 [31], respectively. But this is not the full story. We see that the values of ω_s of YFe₂ and LuFe₂ are also large. Why do they not show Invar anomalies? In order to show the Invar anomaly, the rapid decrease of the magnetic moment should be near the equilibrium lattice constant at ambient conditions. This requirement excludes the Y, Lu compounds to be Invar alloy. In our compounds ZrFe₂ and HfFe₂ the gradual decrease of the magnetic moment is the essential difference, compared with the discontinuity present in a typical Invar system as Fe₃Ni. How to develop an unified Invar theory to include the differences of the Invar alloys is still an open question.

4.6 Doping effects

Doping in ferromagnetic compounds can introduce interesting phenomena, such as metamagnetism or suppressions of ferromagnetism. Concerning doping into ZrFe₂ there was a long-standing problem, namely, the presence of a homogeneity range of the ZrFe₂ Laves phase which was already pointed out some 40 years ago. Then, a certain scatter in the properties was reported, caused by uncertainties in compositions. Reports on the binary Fe-Zr phase diagram also exhibit discrepancies with respect to the phases formed as well as to the extension of homogeneity ranges. In order to clarify this problem, experiments [66] were carried out recently. The main experimental results show that the homogeneity regime extends to ~ 74 at.% Fe content without formation of a secondary phase or a structure change. The substitution takes place at the Zr site: by doping with Fe, the Zr is partially substituted. The magnetic moment per Fe and also

the ferromagnetic Curie temperature increase with the increase of Fe content, on the other hand, the lattice constant decreases.

In order to understand these behaviors within the homogeneity region, we performed LSDA calculations where the atomic substitution has been modeled by Coherent Potential Approximations (CPA). The general idea of the CPA approach is to formulate an effective (or coherent) potential which, when placed on every site of the alloy lattice, will mimic the electronic properties of the actual alloy. Detailed implementation of CPA in FPLO can be found in the paper by Koepernik *et al.* [67]. The valence basis sets comprised $3sp/3d4sp$ states for iron and $3d4sp/4d5sp$ states for zirconium. The local spin density approximation (LSDA) in the parameterization of Perdew and Wang 92 [7] was used in all calculations. The Fe is at 16d site, and Zr and the doped Fe are both at 8a site with the corresponding concentrations according to the CPA setups. The number of k-points in the irreducible wedge of the Brillouin zone was set to 200. Energy convergence at the level of 10^{-7} Hartree was achieved during the self-consistent iterations.

The calculated lattice constants and the experimental ones are listed in the Table 4.4. It is quite obvious from Table 4.4 that doping with irons results in a

Table 4.4: The experimental (a_0^{exp}) and theoretical lattice constants (a_0^{LDA}) of Zr_xFe_{100-x} . The experimental values are taken at room temperature.

Zr_xFe_{100-x}	$a_0^{exp}(\text{\AA})$	$a_0^{LDA}(\text{\AA})$
$Zr_{33}Fe_{67}$	7.0757	6.85
$Zr_{30}Fe_{70}$	7.0570	6.82
$Zr_{28}Fe_{72}$	7.0342	6.77

decrease of the lattice constant. This can be explained by the fact that Fe has a smaller atomic radius than Zr. As we discussed before, the lattice constant of this compound is determined by the volume of the A atom. Doping atoms with a smaller volume decrease the average atomic volume at the A site, so the lattice constant is decreased.

In the stoichiometric compound $ZrFe_2$, the calculated moments amount to $1.65 \mu_B$ for Fe^I atoms at 16d sites and $-0.50 \mu_B$ for the Zr^{II} atoms at 8a sites, respectively. In the non-stoichiometric compounds, the excess Fe^{II} atoms at the 8a sites exhibit an enhanced magnetic moment which increases further with the Fe content as shown in Figure 4.17. The magnetic moment of Fe^{II} is close to that of the BCC Fe ($\sim 2.2 \mu_B$). The related site-resolved density of states shows the characteristics of strong ferromagnetism in the Fe^{II} sublattice (fully occupied majority subband, see Figure 4.18). It has no humps at the Fermi level and only a small tail above it. The nearest neighbor of Zr in the C15 phase is Fe^I and the second nearest neighbor is the doped Fe^{II} . This leads to a stronger hybridization between the nonmagnetic Zr and Fe^I than that between Zr and Fe^{II} , which is quite visible in the DOS shown in Figure 4.18. The DOS of Zr resonates mostly with that of Fe^I instead of Fe^{II} . Moreover, the nearest neighbors of the doped Fe^{II} atoms are Fe^I atoms with a distance larger than the distance between Fe^I and its neighboring Fe^I . Thus the atomic volume of Fe^{II} is larger than that of Fe^I and the related bands are narrower. Both facts

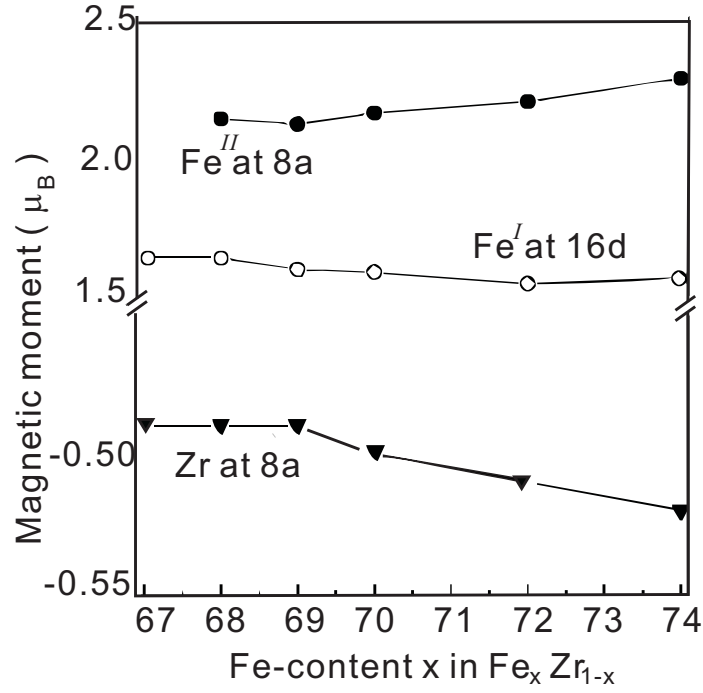


Figure 4.17: The magnetic moments of Fe^I , Fe^{II} and Zr versus the atomic concentration of Fe. The results are obtained at the experimental lattice constants.

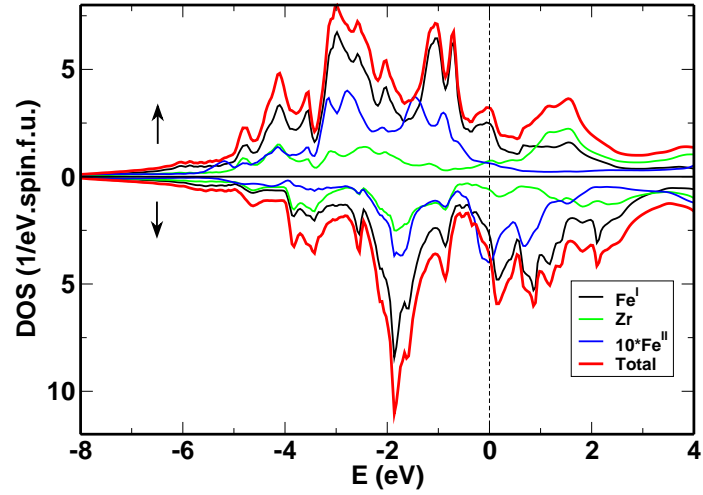


Figure 4.18: The total DOS and the partial DOS of the doped compounds with composition $\text{Zr}_{0.9}\text{Fe}_{2.1}$ at the lattice constant $a = 6.825 \text{ \AA}$.

provide a reason for the larger spin moment on the Fe^{II} sites in comparison with the Fe^I sites, as in Figure 4.17. The averaged total magnetic moments per iron atom calculated at the respective experimental lattice constants are shown in Figure 4.19 in comparison with the data measured at 5 K and 300 K. The

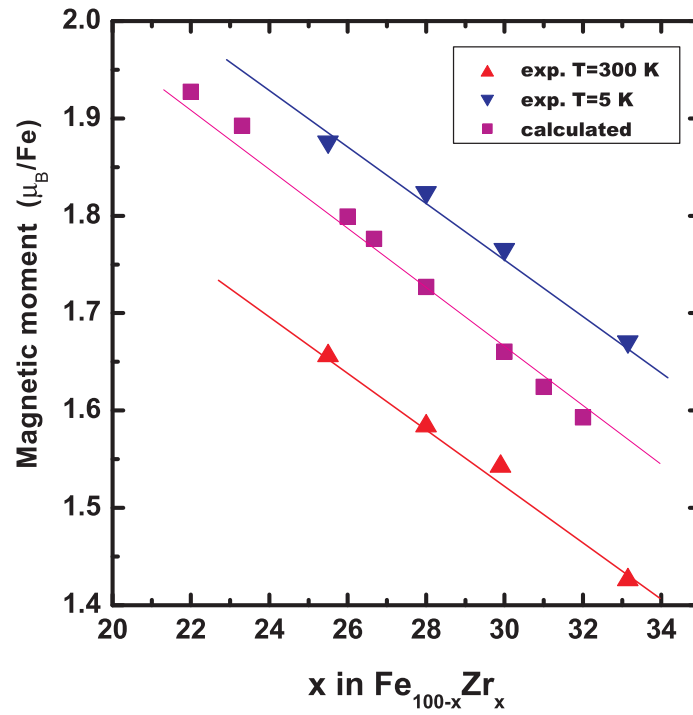


Figure 4.19: The measured and calculated magnetic moments per Fe versus the atomic concentration of Zr. The lines are for guiding the eyes. The results are obtained at the experimental lattice constant.

deviations in the absolute values are within 5% and the LSDA underestimates the magnetic moment. About half of this difference can be attributed to the neglect of the orbital moments in the present scalar relativistic calculations. The linear composition dependence of the magnetic moment is in a good agreement with the experimental data showing almost the same slopes.

Chapter 5

Magnetic transitions in CoO under high pressure

5.1 Introduction

Behavior of transitional metal monoxides has attracted a lot of experimental and theoretical interest. As a property of ground states, band gaps and positions of the Fermi level should be reproduced by DFT. The band gap opening due to strong electron correlations which is not properly reproduced by LDA was partly remedied by combination of LDA and model approaches, namely the LDA+ U . Some other functionals were also invented to treat correlation effects in solids, such as self-interaction corrections (SIC), hybrid functionals, *etc.* This development has proven to be quite successful in exploring and explaining interesting physics in strongly correlated systems. For a review on these aspects, see Ref. [68] by Anisimov *et al.*

Pressure plays a unique role in tuning correlation effects in solids. The importance of the electron correlation is measured, to some extent, by the ratio U/W , where U is the correlation energy of the localized orbitals and W is the related band width. Generally, W is increased when the pressure becomes enhanced because of the increased hopping probability of the electrons due to larger orbital overlap. So the ratio U/W becomes smaller under pressure. On the other hand, pressure can lead to structural phase transitions, because it alters the bonding character. Thus the local environment, especially the crystal field or ligand field is changed. All of these changes will impact on magnetism. How the magnetic moment changes under pressure is an important feature of magnetic systems. We have already seen that the magnetic moment can behave differently in itinerant electron systems. The transition to a nonmagnetic state can be of a first or a second order. There are at least two reasons for such a transition. On one hand, it can arise because the bands broaden, so that the Stoner criterion is no longer satisfied. On the other hand, it can arise because of structural transitions, so that the local environment is changed.

The magnetic moment behavior under pressure of a Mott insulator, the transition metal monoxides, can be yet more interesting and complicate. Considering the parameters which influence the properties, the electron correlation energy U , the electron band width W , the spin pairing energy J , the ligand field

strength Δ_l , and the $p-d$ charge transfer energy Δ_{pd} , all of these parameters are of the same order and enter the model Hamiltonian to describe electronic properties. Especially, the last four parameters are very susceptible to pressure. Because of this complex situation, quite a lot of work has already been done. MnO and FeO under high pressure were studied by Fang *et al.* [69] using GGA and supplemented by LDA+ U . Three spin configurations, nonmagnetic (NM), ferromagnetic (FM), and antiferromagnetic (AFM) were investigated and the crystal structures were optimized. It was found that, at high pressure, MnO should take the NiAs (nB8) structure being either FM or AFM, and in the intermediate pressure range, the NM rhombohedrally distorted B1 (rB1) phase with a stretched distortion can be realized. For FeO under high pressures it was predicted to have an inverse NiAs (iB8) structure. It transfers from a Mott insulator to a band insulator under this high pressure. Recently, pressure-driven magnetic moment collapse in MnO was extensively studied by Kasinathan *et al.* It was found that the spin state transforms from $S=\frac{5}{2}$ to $S=\frac{1}{2}$ under high pressure [70]. The low spin state was obtained by a spin flip within the e_g states, producing a quite anisotropic spin density but a relatively isotropic charge density. The specific ground state is not only sensitively dependent on U which is the usual case, but also on J , which influences the gain in exchange energy from the anisotropic part of the spin density. The results from calculations using different functionals (LDA+ U , SIC, and hybrid functionals) [71] indicate that the high pressure state (metallic or insulating) and the phase transition pressures are quite sensitive to the functionals. Nevertheless all related calculations predicted a first order magnetic transition from HS ($S=\frac{5}{2}$) to LS ($S=\frac{1}{2}$) state.

In CoO the interactions between pressure, structure and magnetism are complicate, leading to different structural and magnetic phases under different pressures. The transition to a non-magnetic state shows a first order behavior. The basic phase diagram summarized from several recent experimental results is shown in Figure 5.1. At ambient conditions, CoO is a paramagnetic insulator

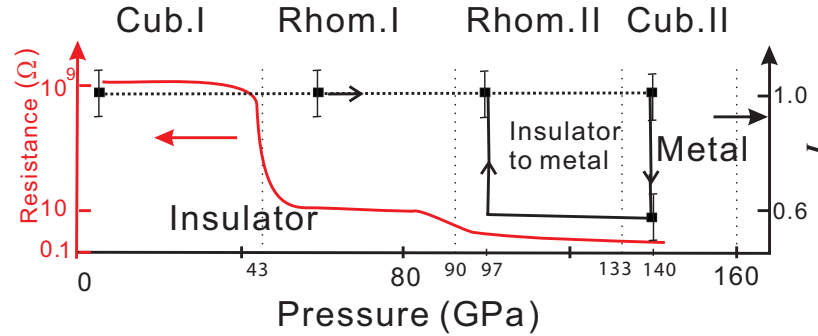


Figure 5.1: Electrical resistance, structure and magnetic transition under pressure as summarized from recent experiments [72, 73, 74, 75]. I is the satellite intensity of the X-ray emission spectra (XES).

with a rock salt structure. Below its Néel temperature ($T_N=290$ K), it orders antiferromagnetically along the $\langle 111 \rangle$ direction and preserves an insulating state. Accompanying the magnetic order, it distorts into a tetragonal structure with a small rhombohedral distortion. The magnetic structure [76] investigated

by synchrotron magnetic X-ray scattering reveals significant reflections by the magnetic moment propagating along the tetragonal as well as along the rhombohedral axis. Thus, the magnetic symmetry is monoclinic, in accordance with the distorted lattice symmetry which is also monoclinic. On applying hydrostatic pressure, the ambient temperature rock salt crystal transforms into a rhombohedral structure at about 43 GPa [72]. When the pressure is increased to 90 GPa, a sudden decrease of the volume by 2.7% is observed by highly precise synchrotron X-ray diffraction [73], which results in a transition to a denser rhombohedral phase (Rhom. II). Above a pressure as high as 133 GPa, the compound returns to its cubic crystal structure (Cub. II). The Néel temperature T_N is also increased under pressure. But the pressure induced structural phase transition cannot be so simply explained by the onset of magnetism with the increase of the Néel temperature, because of the lack of tetragonal distortion under pressure. Under pressure as high as about 140 GPa, a magnetic transition from high spin to low spin state takes place [74]. The magnetic moment persists with a lower value but not equal to zero which is evident from the non-vanishing intensity of K_β emission line ($3p \rightarrow 1s$) from the transitional metal atom. The change of the intensity of the X-ray emission spectroscopy (XES) under pressure is shown in Figure 5.1, where the intensity of the satellite line drops to 60% of the intensity at ambient pressure. The existence of the satellite lines indicates that the magnetic moment does not totally collapse. On releasing the pressure the magnetic HS state recovers at a pressure of about 97 GPa. The magnetic moment transition shows hysteresis.

The collapse of the magnetic moment was proposed to be related with a re-occupation from an E_g majority spin state to a T_{2g} minority spin state, i.e., from a HS state with spin $S = \frac{3}{2}$ ($T_{2g}^5 E_g^2$) to a LS state with $S = \frac{1}{2}$ ($T_{2g}^6 E_g^1$). Recent electrical resistance measurements at room temperature [75] show that under pressure above 133 GPa, the material shows metallic behaviors (increase of the resistance under increase of the temperature). Below that, the material shows a transition state between insulators and metals. There is a drastic decrease of the resistance at a pressure of about 43 GPa, as shown in Figure 5.1, which corresponds to the structural phase transition from the Cub. I phase to the Rhom. I phase, but the electronic reason is unrevealed.

Summarizing the results, the experiments show that the crystal structure and the magnetic structure under pressure are complicate. There are several successive structural, magnetic and electronic phase transitions, which are related to each other. With the hope to elucidate the behavior of CoO under pressure we resort to the theoretical description.

Early theoretical calculations for CoO were mainly concentrated on its electronic structure at ambient condition. LSDA+ U was first used by Anisimov [77] to study the band gap opening problem in this material due to the on-site correlation. Lattice dynamics of CoO was studied by LSDA+ U [78] where a sensitive U dependence of the lattice dynamics was found. The acoustic branches of the phonon dispersion agree well with the experiments. Recently, hybrid exchange-correlation energy functionals were used and proved to be quite successful in this compound as an alternative to LSDA+ U to study strongly correlated electrons [79]. LSDA (GGA) calculations by Cohen *et al.* [80] show that under a pressure of about 18 (88) GPa, the magnetic moment collapses to zero, which does not agree with recent experiments. At some intermediate pressures, they found that there exists a low spin solution with $m \sim 0.3 \mu_B/\text{Co}$ obtained from a

generalized Stoner theory, but the details of the electronic structure of this phase and how it is developed were not shown. Of course the insulating behavior at ambient pressure and moderate pressures was not reproduced by LSDA (GGA). Thus, the LSDA might also fail to describe the magnetic behavior, especially the processes of this transition.

In this chapter, the LSDA+ U functional is used to investigate the magnetic moment behavior in this strongly correlated electron compound CoO. The results reveal that ligand field splits of the 3d electrons play an important role in the magnetic moment transition at variance with the discussions based on the LSDA results of Cohen *et al.* [80].

5.2 A brief introduction to LSDA+U

In order to improve the treatment of strongly correlated systems, the combination of the LSDA and many body theory (mainly the Hubbard model) was proposed by Anisimov [77, 81]. The energy functional is generally expressed by

$$E^{LSDA+U} = E^{LSDA} + E^{int} - E^{dc}, \quad (5.1)$$

where E^{LSDA} is the LSDA functional, E^{int} is the Coulombic interaction between the correlated local orbitals, and E^{dc} is the double counting term which excludes the energy already included in the LSDA. Depending on the treatment of E^{dc} , there are two main versions of the functionals, namely the “around the mean field” (AMF) version invented by Anisimov himself and the “atomic limit” (AL) introduced by Czyżyk and Sawatzky [82]. The latter version roughly shifts the energy of the unoccupied orbitals upwards by $(U - J)/2$ and that of the occupied orbitals downwards by the same amount, while the former version gives nearly nothing for a half-filled fully spin polarized shell.

The U -functional is incorporated into the Kohn-Sham scheme through the orbital related K -part of the functional as explained in Section 2.3.

$$K = t + e^H + e^{U,AMF(AL)} \quad (5.2)$$

where

$$t + e^H = \sum_i n_i \langle \phi_i | \hat{t} | \phi_i \rangle + \sum_{ij} \frac{n_i n_j}{2} \langle \phi_i \phi_j | \tilde{w} | \phi_i \phi_j \rangle, \quad (5.3)$$

$$\begin{aligned} e^{U,AMF} &= \frac{1}{2} \sum_{\mathbf{R}\sigma\mu,\mu'} \{ (\mu\sigma, \mu'-\sigma | \tilde{w} | \mu\sigma, \mu'-\sigma) (\tilde{n}_{\mu\sigma} - \tilde{n}_\sigma) (\tilde{n}_{\mu'-\sigma} - \tilde{n}_{-\sigma}) + \\ &\quad [(\mu\sigma, \mu'\sigma | \tilde{w} | \mu\sigma, \mu'\sigma) - (\mu\sigma, \mu'\sigma | \tilde{w} | \mu'\sigma, \mu\sigma)] (\tilde{n}_{\mu\sigma} - \tilde{n}_\sigma) (\tilde{n}_{\mu'\sigma} - \tilde{n}_\sigma) \} \\ &= \frac{1}{2} \sum_{\mathbf{R}\sigma\mu\mu'} \{ (\mu\sigma, \mu'-\sigma | \tilde{w} | \mu\sigma, \mu'-\sigma) \tilde{n}_{\mu\sigma} \tilde{n}_{\mu'-\sigma} + \\ &\quad [(\mu\sigma, \mu'\sigma | \tilde{w} | \mu\sigma, \mu'\sigma) - (\mu\sigma, \mu'\sigma | \tilde{w} | \mu'\sigma, \mu\sigma)] \tilde{n}_{\mu\sigma} \tilde{n}_{\mu\sigma} \} \\ &\quad - \frac{1}{2} \sum_{\mathbf{R}\sigma} \{ U(N - \tilde{n}_\sigma) - J(N_\sigma - \tilde{n}_\sigma) \} N_\sigma, \end{aligned} \quad (5.4)$$

$$e^{U,AL} = e^{U,AMF} + \frac{1}{2} \sum_{\mathbf{R}\sigma} (U - J)(1 - \tilde{n}_\sigma) N_\sigma, \quad (5.5)$$

where \tilde{w} is the screened Coulombic interaction, and $|\mu\sigma\rangle$ indicates the correlated orbitals μ with spin σ . \mathbf{R} is the position of the correlated orbital. N is the number of electrons occupying the whole correlated shell, and N_σ is that for one spin sort. ϕ_i is the Kohn-Sham orbitals with an occupation number n_i . U and J are the correlation and exchange parameters which are input parameters in this scheme. They are used to evaluate the Coulombic integrals via their relationship with the Slater integrals F_l . In the above equations, the occupation matrix \tilde{n} of the correlated shells is to be determined from the Kohn-Sham orbitals and their occupation numbers:

$$\tilde{n}_{mm'\sigma} = \sum_i (m\sigma|\phi_i\rangle n_i \langle\phi_i|m'\sigma), \quad (5.6)$$

where $|m\sigma\rangle$ are the localized correlated orbitals used in the program. It can be diagonalized by a unitary transformation

$$\tilde{n}_{mm'\sigma} = \tilde{U}_{m\mu}^\sigma \tilde{n}_{\mu\sigma} \tilde{U}_{m\mu}^{\sigma*}, \quad (5.7)$$

where $\tilde{U}_{m\mu}^\sigma$ is an unitary matrix. The averages over correlated shells and spins read:

$$\tilde{n}_\sigma = \frac{1}{2l_c + 1} \sum_\mu \tilde{n}_{\mu\sigma}, \quad \tilde{n} = \frac{1}{2}(\tilde{n}_+ + \tilde{n}_-), \quad (5.8)$$

with $2l_c + 1$ the total number of the correlated orbitals.

With the functionals above, the U -potentials of the two versions are:

$$V_{\mu\sigma}^{AMF} = \frac{\partial e^{U,AMF}}{\partial \tilde{n}_{\mu\sigma}} = \sum_{\mu'} \{ (\mu\sigma, \mu'-\sigma | \tilde{w} | \mu\sigma, \mu'-\sigma) (\tilde{n}_{\mu'-\sigma} - \tilde{n}_{-\sigma}) + [(\mu\sigma, \mu'\sigma | \tilde{w} | \mu\sigma, \mu'\sigma) - (\mu\sigma, \mu'\sigma | \tilde{w} | \mu'\sigma, \mu\sigma)] (\tilde{n}_{\mu'\sigma} - \tilde{n}_\sigma) \} \quad (5.9)$$

and

$$V_{\mu\sigma}^{AL} = \frac{\partial e^{U,AL}}{\partial \tilde{n}_{\mu\sigma}} = V_{\mu\sigma}^{AMF} - (U - J)(\tilde{n}_\sigma - \frac{1}{2}). \quad (5.10)$$

Both these versions of the LSDA+ U were implemented into the current FPLO code. Technical details can be found in Reference [2] and [83].

5.3 A Category of insulators

Restrictions to zero temperature and small external fields allow us to identify two basic categories of insulators [84], namely,

- insulators due to the electron-ion interaction, and
- insulators due to the electron-electron interaction.

The first category subsumes all insulators which can be understood in terms of single-electron theory. The second one, which includes all the rest, is conceptually different. In this category we will have to deal with the *many-electron problem*. The Mott insulator is due to the electron-electron interaction. We have seen in the previous section that the strong electron correlation will split the half filled d band. This splitting is modeled by a parameter U in the Hubbard

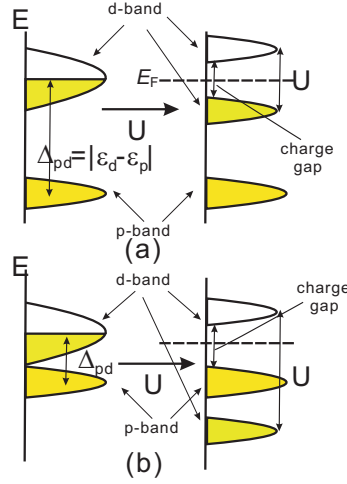


Figure 5.2: A schematic illustration of energy levels for (a) a Mott-Hubbard insulator and (b) a charge-transfer insulator generated by the Coulombic interactions of localized d-orbitals. This figure is adapted from Ref [85].

model or the related mean-field approximation, like LSDA+ U . The system is called a Mott-Hubbard insulator as long as U is smaller than energy splitting of the O-2p and 3d bands $\Delta_{pd} = |\epsilon_d - \epsilon_p|$. In this case, the energy gap is situated in the d band. In contrast, if Δ_{pd} is smaller than U , the gap is between the O-2p and the upper Hubbard part of the 3d band. Thus, any hole excitation goes into the O-2p shell. This type of compound is called a charge-transfer insulator. The energy levels for these two kinds of Mott insulators are schematically drawn in Figure 5.2.

5.4 Computational parameters

CoO crystalizes into the rock salt (B1) structure at room temperature. The magnetic moments of Co are ferromagnetically coupled in the $\{111\}$ planes and antiferromagnetically coupled between the planes. If we ignore the tetragonal distortion, we obtain a trigonal space group ($R\bar{3}m$). The two antiferromagnetically coupled Co atoms occupy the Wyckoff positions 1a (0, 0, 0) and 1b (1/2, 1/2, 1/2) respectively, while the O atoms occupy 2c (1/4, 1/4, 1/4). The conventional unit cell is shown in Figure 5.3. The exchange correlation functional is parameterized according to Perdew-Wang 92 [7]. The number of k-points in the irreducible wedge of the BZ is set to be 11076. The energy convergency criterion is set to be 10^{-8} Hartree. The atomic limit version of the U -functional is used with the orthogonal projection method. This choice of functional gives a better agreement with the experiments for the HS state compared with the “AMF” functional.

Before presenting the details of our calculation, we illustrate the related coordinates and the symmetry frequently used in the following discussions [71]. Because of the antiferromagnetic coupling between the $\{111\}$ layers of Co, the cubic crystalline symmetry is reduced to rhombohedral one if we leave out the

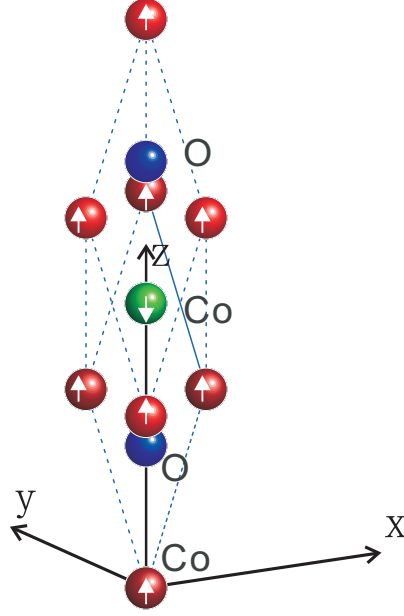


Figure 5.3: The conventional unit cell of CoO in the antiferromagnetic state. The red and green Co atoms are antiferromagnetically coupled. The Z axis is the diagonal axis in the cubic rock salt crystal.

lattice distortions. From now on we use capital letters (T_{2g} , E_g) to indicate the representations of the cubic symmetry, and lower cases ($e_{g,1}$, $e_{g,2}$, a_g) for the representation of the rhombohedral symmetry. In the cubic symmetry the Co 3d states split into irreducible representations (IR's) denoted by T_{2g} (threefold degenerate) and E_g (twofold degenerate). The rhombohedral site symmetry results in the three IR's a_g , $e_{g,1}$ and $e_{g,2}$ with the first one being one dimensional and the latter two being both twofold degenerate. In our calculation, the coordinates of the cubic lattice and the rhombohedral one (with superscript c and r, respectively) are related by:

$$\begin{pmatrix} x^r \\ y^r \\ z^r \end{pmatrix} = \begin{pmatrix} \frac{1}{\sqrt{6}} & \frac{1}{\sqrt{6}} & -\frac{\sqrt{2}}{\sqrt{3}} \\ -\frac{1}{\sqrt{2}} & \frac{1}{\sqrt{2}} & 0 \\ \frac{1}{\sqrt{3}} & \frac{1}{\sqrt{3}} & \frac{1}{\sqrt{3}} \end{pmatrix} \begin{pmatrix} x^c \\ y^c \\ z^c \end{pmatrix}. \quad (5.11)$$

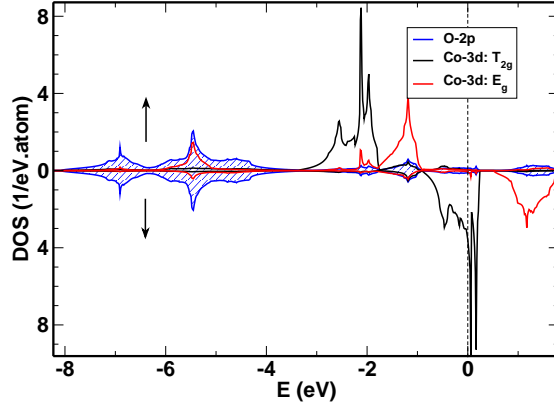


Figure 5.4: LSDA-DOS of the 3d states of Co and 2p states of O. The d states are resolved into the irreducible representations of the cubic symmetry. The Fermi level is shown by the dashed vertical line at $E=0$ eV.

Thus the 3d orbitals are transformed like:

$$d_{xy}^r = \frac{1}{\sqrt{3}}(d_{xy}^c - d_{yz}^c - d_{x^2-y^2}^c), \quad (5.12)$$

$$d_{yz}^r = \frac{1}{\sqrt{6}}(d_{yz}^c - d_{xz}^c) - \sqrt{\frac{2}{3}}d_{x^2-y^2}^c, \quad (5.13)$$

$$d_{xz}^r = \frac{\sqrt{2}}{3}d_{xy}^c - \frac{1}{3\sqrt{2}}(d_{xz}^c + d_{yz}^c) - \sqrt{\frac{2}{3}}d_{z^2}^c, \quad (5.14)$$

$$d_{x^2-y^2}^r = -\frac{1}{3}(d_{xz}^c + d_{yz}^c - 2d_{xy}^c) - \frac{1}{\sqrt{3}}d_{z^2}^c, \quad (5.15)$$

$$d_{z^2}^r = \frac{1}{\sqrt{3}}(d_{xy}^c + d_{yz}^c + d_{xz}^c). \quad (5.16)$$

The orbital quantum number is corresponding to the symmetrized d orbitals as shown in the Appendix: $|m_l| = 2 \leftrightarrow d_{xy}^r, d_{x^2-y^2}^r$, $|m_l| = 1 \leftrightarrow d_{xz}^r, d_{yz}^r$, and $m_l = 0 \leftrightarrow d_{z^2}^r$. Note that if there are components of the crystal field that are not diagonal in the $L=(2, m_l)$ basis, these states will be mixed. For example, the IR's $e_{g,1}$ and $e_{g,2}$ are a mixture of $|m_l| = 2$ and $|m_l| = 1$, while a_g contains only $m_l = 0$.

5.5 LSDA pictures

By LSDA, we obtain an equilibrium volume of 118.7 a.u. per formula unit (f.u.), which is much smaller (9%) than the experimental one (~ 130.5 a.u./f.u.). The density of states of the Co-3d and O-2p bands are presented in Figure 5.4 according to the irreducible representations of the site symmetry (E_g and T_{2g}). The calculation has been carried out at the LSDA equilibrium volume. It is quite clear that the ligand field separates the E_g and T_{2g} bands. This splitting amounts to about 1 eV. The exchange splitting is about 2.5 eV. A schematic plot of the 3d states is shown in Figure 5.5. In our LSDA calculations, all five

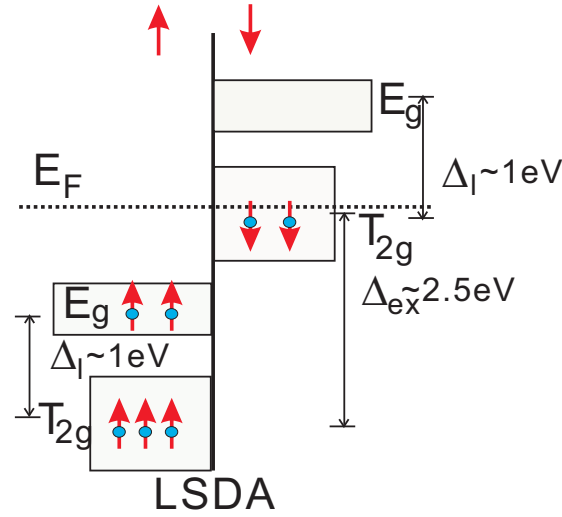


Figure 5.5: LSDA model DOS of the 3d states of Co in CoO

Co 3d states of the up spin channel are occupied, which is favorable by Hund's rule. The states from the O-2p and Co-3d are not so much hybridized. The O-2p states are located about 3 eV below Co-3d states.

Under hydrostatic pressure, the magnetic moment decreases, and at last vanishes under compression of the volume to about 80%. The magnetic moment under pressure is shown in Figure 5.6. Here we basically reproduce the LSDA (GGA) results by Cohen [80]. The collapse of the magnetic moment is because the Stoner criterion is no longer satisfied. With the increase of the bandwidth under compression, the exchange is suppressed as discussed in the Stoner model before. The magnetic moment jumps from a high value to zero.

As discussed by Terakura [86], the partially filled T_{2g} state gives rise to metallic behavior in the LSDA model. The exchange and crystal field splitting can produce an insulating state in MnO and NiO, but not in FeO and CoO. The Fermi level crosses the T_{2g} states, because there are two electrons and three available degenerate orbitals in the minority spin channel. Terakura proposed that the large orbital moment in these latter two compounds can induce a band gap, because the orbital and spin interaction will lead to a population imbalance in the three T_{2g} orbitals. A gap will open in the band when two of the states are occupied and one is empty. They concluded that the band gap problem is from the LSDA, not from the band picture of the solid. An electronic structure calculation by Norman [87], where orbital polarization and spin orbit coupling were included, confirmed this proposal. But the resulting total moment is too large and the band gap is too small. If the orbital moments were corrected to its experimental value (about 50% of the calculated value), it would be too small to open the gap. So Norman concluded that more sophisticated orbital polarization functionals were desired in order to correctly describe the insulating state.

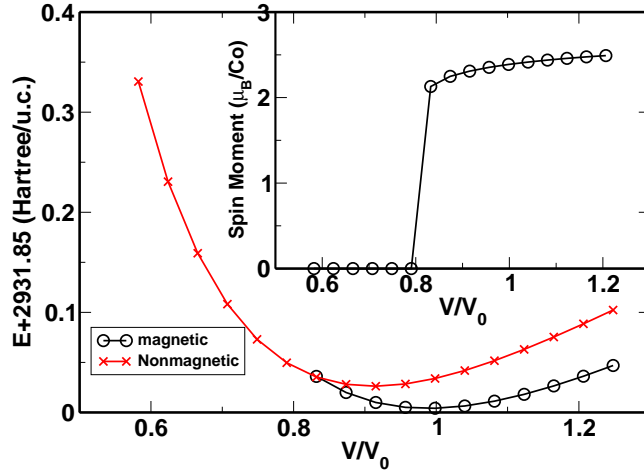


Figure 5.6: Magnetic moment of Co and total energy versus the relative volume. The reference volume $V_0=118.7$ a.u..

5.6 LSDA+ U pictures

Already the LSDA approach gives the HS to NM transition. Further, using LSDA in strongly correlated systems under high pressure has its justification: because of the increase of the hopping probability under pressure, the correlation plays now a less important role compared with the case of ambient pressure. As mentioned in the introduction, the importance of correlation is measured by U/W , where U is the correlation energy of the localized states (3d states of Co here) and W is the related bandwidth. Nevertheless, the physical picture of the moment collapse can be different if we treat the correlation differently (for example, by LSDA+ U). In our view, “less important” is different from “non-existing”. More importantly, the physical mechanism of the transition uncovered by the LSDA+ U approach may also be different from the LSDA picture.

Different view points on the behavior of CoO under pressure were taken in the literature. As discussed by Cohen [80], the physics underlying the magnetic collapse could be the Stoner model: the competition between the band energy and the exchange energy. As proposed by Ohnishi [88], the crystal-field splitting is another candidate for the HS-LS transition in some transitional metal complexes. As mentioned in the previous section, all parameters (U , W , J , Δ_l) are comparable and may play their role in determining the electronic state, so it is necessary to take as many as possible parameters into account in order to uncover the physics underlying different phenomena. Very recently, a two orbital model Hamiltonian involving U , J , Δ_l was solved by Millis *et al.* [89] showing that all of these parameters strongly influence the HS to LS transition.

5.6.1 Electronic structures of the ground state

The energy versus of CoO volume curves obtained by LSDA+ U calculations are shown in Figure 5.7(a), together with the spin moment of Co in the inset. The curves for different value of U (3 eV, 5 eV, and 7.8 eV) and the same $J=1$

eV are presented in order to get an impression how the value of U influences the results. The smaller the U is, the smaller the magnetic moment is and the faster the moment under pressure decreases as shown in the inset of Figure 5.7(a). Thus, the reduced screening stabilizes the moment.

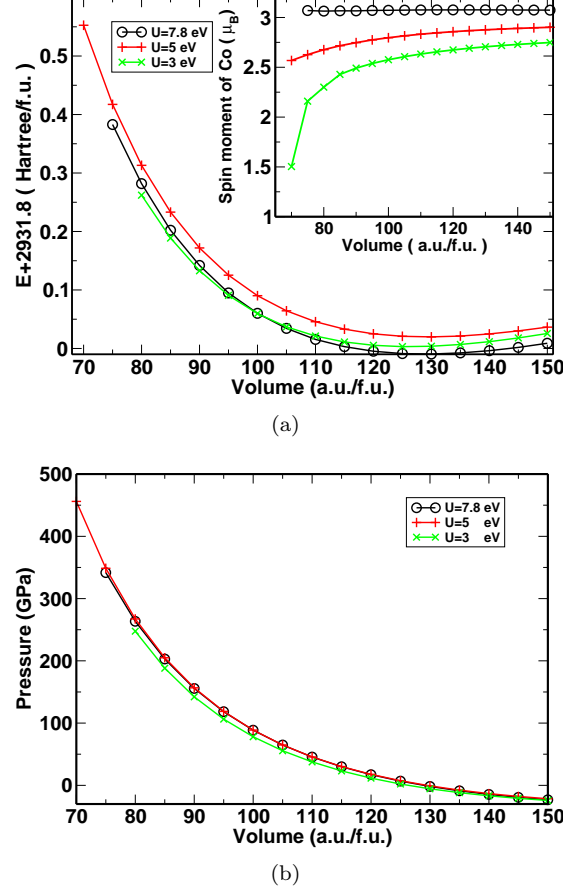


Figure 5.7: The total energy, spin moment (a) and hydrostatic pressures (b) under different volumes from LSDA+ U with different value of U (3, 5, and 7.8 eV respectively) and the same $J=1$ eV. The “AL” version of LSDA+ U is adopted in the calculations.

The energy versus volume curves are fitted to Birch’s EOS [90]:

$$E(V) = E_0 + \frac{9}{8}B_0V_0\left[\left(\frac{V_0}{V}\right)^{2/3} - 1\right]^2 + \frac{9}{16}B_0V_0(B'_0 - 4)V_0\left[\left(\frac{V_0}{V}\right)^{2/3} - 1\right]^3, \quad (5.17)$$

where V_0 and E_0 are the equilibrium volume and energy respectively, and B_0 and B'_0 are the bulk modulus and its pressure derivative respectively. The pressure dependence on volume is shown in Figure 5.7(b). The equilibrium volume, the bulk modulus and its derivatives obtained from different values of U are listed in Table 5.1, together with the experimental results in the lowest row. The LSDA+ U improves the equilibrium volume and the bulk modulus compared

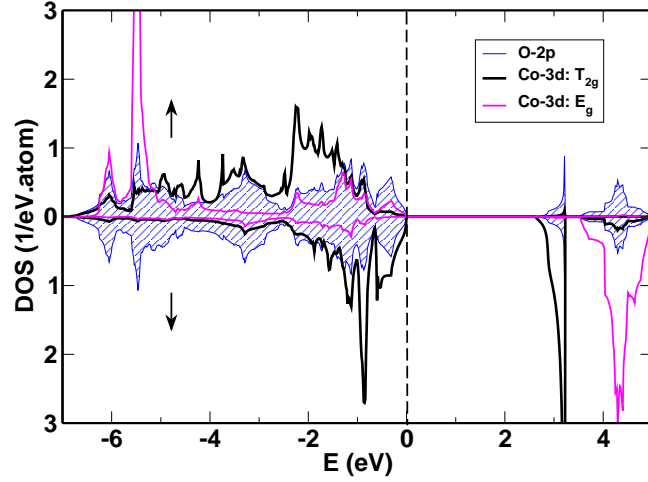


Figure 5.8: The Co-3d and O-2p DOS at the equilibrium lattice constant with $U=5$ eV. The Co-3d DOS is decomposed into T_{2g} and E_g representations. The O-2p DOS is shown by the area filled with slashes.

with the LSDA ($U = 0$). In our case $U=5$ eV reproduces the experiments best and this value will be used in further calculations unless specified explicitly. Because of the strong correlation between the 3d electrons, the occupied and unoccupied T_{2g} levels will be split by an amount of $U - J$ as expected in the “AL” version of LSDA+ U . An insulating state is obtained with a band gap about 2.6 eV at $U=5$ eV, which agrees relatively well with the optical band gap of about 2.4 eV [68].

Table 5.1: Ground state properties of CoO obtained by LSDA+ U calculations with different values of U . Experimental data are given in the last row.

U (eV)	V_0 (a.u./f.u.)	B_0 (GPa)	B'_0	Band gap (eV)
0	118.7	235	4.5	0
3	126.3	202	4.2	1.2
5	129.4	198	4.2	2.6
7.8	128.9	208	4.1	3.4
<i>exp</i>	130.5	180	3.8	2.4

The Co-3d DOS in the high spin state is shown in Figure 5.8. The ligand field split of the unoccupied T_{2g} orbitals and the E_g orbitals is estimated about 1.0 eV by evaluating the center of gravity of the unoccupied states as shown in Figure 5.16. Compare with the DOS obtained in the LSDA, Figure 5.4: In the LSDA, the O-2p states are situated well below (~ 3 eV) the 3d states, while in the LSDA+ U the O-2p states are spread from -7 eV up to 0 eV. The correlation energy U pushes the occupied d states downwards, thus hybridizations with the O-2p orbitals are much stronger. We observe that the states between -1 and 0 eV in the majority spin channel originate mainly from the oxygen p states.

This shows the charge transfer character of the compound. At the same time, the DOS of the minority d states is also present in the same energy region. So both of them can contribute to the optical excitations. Experimentally, detailed resonant photoemission spectroscopy (RPES) measurements [91] aimed at 2p and 3p core-levels confirms the charge transfer character of CoO. Recent soft X-ray scattering investigations show that the final state is $3d^8\bar{L}$, where \bar{L} means a hole in the O-2p shell. The charge transfer energy (Δ_{pd}) is determined to be 4.0 eV where the single impurity Anderson model was used to simulate the experimental spectroscopy [92], which is smaller than the value $U=5$ eV used in our calculations. This agrees with the condition of our schematic illustration of the charge transfer insulator ($\Delta_{pd} < U$).

5.6.2 Magnetic transitions in LSDA+ U

From the electronic structure calculations, the energy diagram of the 3d states of Co can be drawn as in Figure 5.9(a). In this and the following schematic drawings, we neglect the effect of hybridizations between the Co-3d and O-2p states. This is because, depending on U , the hybridization between O-2p and Co-3d states is different and this will cause noticeable charge transfer between Co and O. The charge transfer effect is orbital dependent. This difference of occupation numbers will change the distance between the relative centers of gravity of the occupied E_g and T_{2g} states because of U , while the unoccupied states are not influenced. The ligand field splitting of the occupied states is not so clear now, as can be seen in Figure 5.8. There is a high resonant E_g peak at an energy of -5.5 eV. This peak shifts the center of gravity of the E_g states significantly. But it is not from the symmetry reason. This is the reason that we use the distance between the unoccupied E_g and T_{2g} states to estimate the ligand field splitting in the forthcoming discussions.

Under ambient pressure, the electrons will take the occupation favored by Hund's first rule, because the ligand field splitting Δ_l between the E_g and T_{2g} levels is small (~ 1 eV). If we put the energy of the high spin states to zero, the flip of one spin in E_g state to T_{2g} state gives an energy contribution of $\Delta E = \Delta_{ex} - \Delta_l = 2J - \Delta_l$. If $\Delta_l < 2J$, the system will stay in the high spin state, otherwise, it will transform into a state with lower spin. Under pressure, the ligand field splitting Δ_l is enlarged because of stronger hybridization with the ligands, and the E_g and T_{2g} states are pushed further apart. The PDOS under pressure is shown in Figure 5.10. The model DOS of this situation is shown in Figure 5.9(b).

There are all together seven electrons in the atomic Co-3d shell. According to Hund's first rule, the spin up shell is fully occupied. The spin down channel is occupied with two electrons. The spin moment in the atomic ground state is $3 \mu_B$. In LSDA+ U , the DOS shows that the majority spin states are fully occupied as well. For the minority spins, we can see from Figure 5.8 that the E_g states are empty and the T_{2g} states are partially occupied. When switched into the IR of the rhombohedral lattice, for the minority spin state, the a_g ($m_l = 0$) states are unoccupied and one of the e_g bands is unoccupied, while the other is fully occupied. This occupation pattern results in a DOS as shown in Figure 5.11.

As shown by Korotin [93], the initial electronic occupation of the localized orbitals will influence the final occupation of the orbitals because of the orbital-

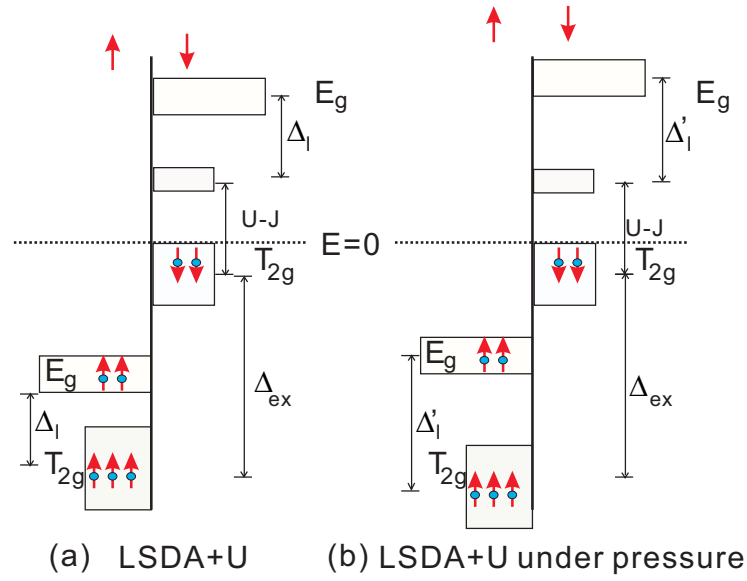


Figure 5.9: The LSDA+ U model DOS (a) and its variation under pressure (b).

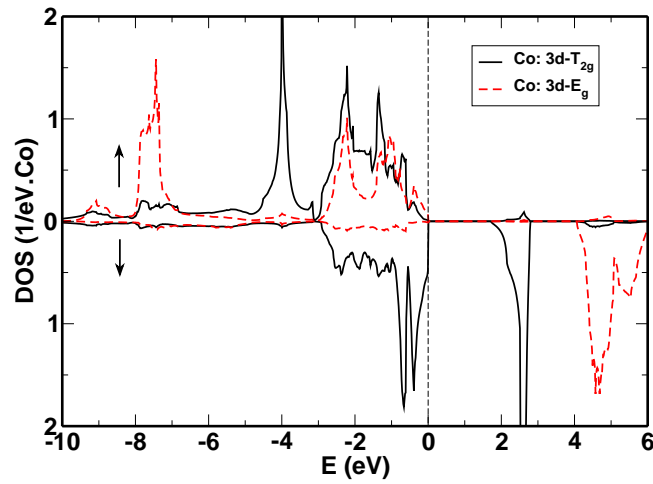


Figure 5.10: The LSDA+ U PDOS at a volume of 90 a.u./f.u., about 70% of the theoretical equilibrium volume.

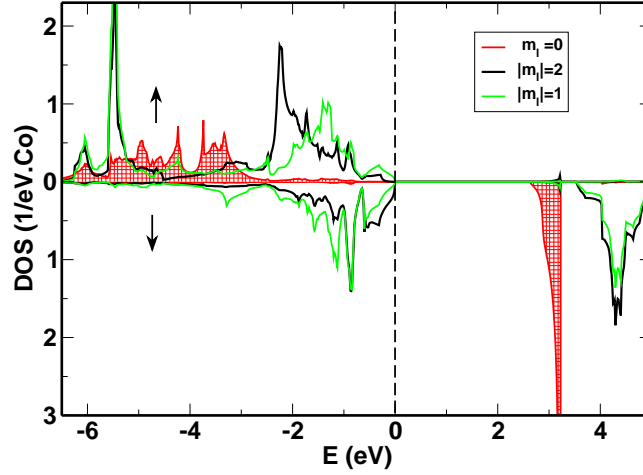


Figure 5.11: The Co-3d PDOS at the equilibrium lattice constant (the same calculation as Figure 5.8). It is resolved into different angular quantum number with respect to the rhombohedral lattice.

dependent potential in LSDA+ U . We obtain the possible solutions by giving the initial occupations at the very beginning. In order to explore the possible low spin solutions, we tried all the initial configurations. There are $3 \times 3 = 9$ possibilities if we flip one of the electrons in $e_{g,1(2)}$ or a_g state of the majority channel to the $e_{g,1(2)}$ or a_g state of the minority channel. After self-consistent iterations, the initial populations converge into the following two cases:

- A flip between $m_l = 0$ (a_g) (LS-I). If we just flip one a_g electron, then the original occupied a_g state in the up-spin channel will be un-occupied. Because just the a_g spin flips, the insulating state is unaffected. The energy is higher than the high spin states in all the volume region we considered as will be shown in Figure 5.15, which means that this kind of spin flip is energetically unfavorable. This is because that the exchange interaction is increased by an amount of $2J$, but there are no significant contributions to the decrease of the electronic static energy, for example, by decreasing the ligand field energy.
- A flip from $m_l \neq 0$ to $m_l = 0$ (LS-II). In this case, the singlet a_g spin down state will be totally occupied. The four $e_{g,1(2)}$ spin down states will be partially occupied by two electrons. Therefore, a metallic state is obtained and the Fermi level situates inside the admixture of the $e_{g,1}$ and $e_{g,2}$ states.

The Co-3d DOS of the LS-I and LS-II low spin solutions are shown in Figure 5.12 (a) and (b), respectively. It can be seen that the flip of the $e_{g,1(2)}$ state to the a_g state gives a metallic solution. After decomposing the PDOS according to the cubic symmetry, it turns out that the Fermi level crosses the E_g orbital and the T_{2g} states are totally occupied as shown in Figure 5.13. In this case we obtain the model DOS for the low spin solution as in Figure 5.14.

The magnetic moment and the energy versus the relative volume of different solutions are shown in Figure 5.15. It can be seen that with the increase of

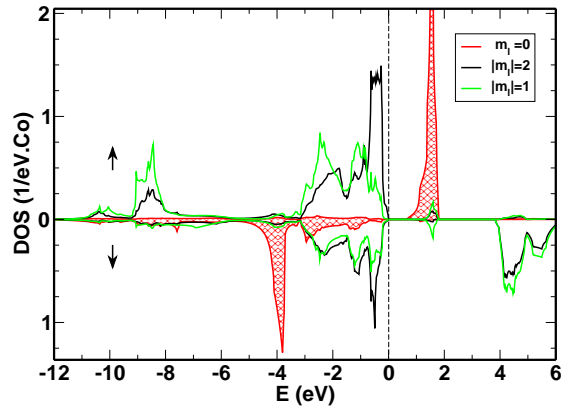
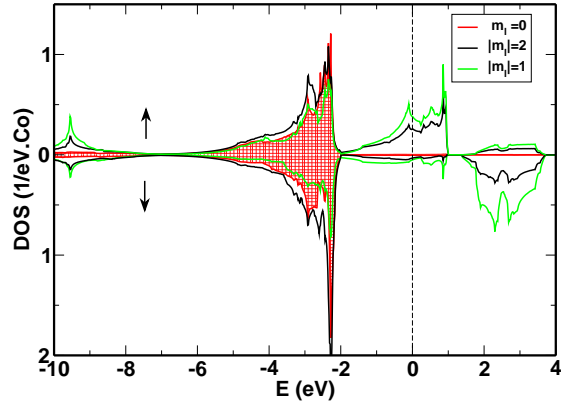
(a) The DOS of $a_g - a_g$ flips (LS-I).(b) The DOS of e_g flips (LS-II).

Figure 5.12: The Co-3d PDOS for the two possible low spin solutions. The filled curve is the PDOS with a_g symmetry.

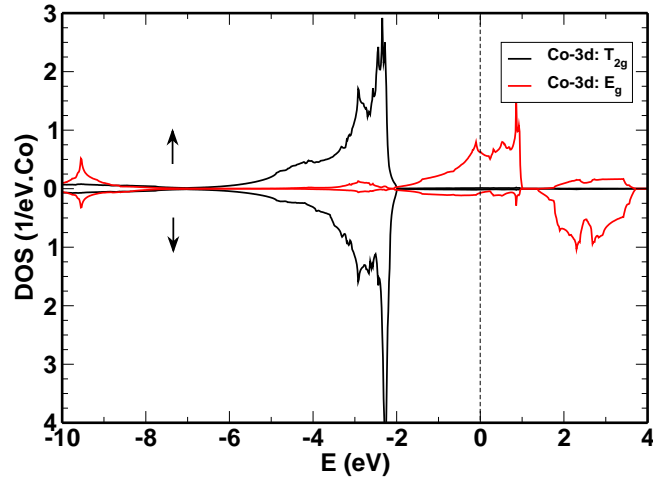


Figure 5.13: The PDOS after the electron with e_g symmetry flips its spin. It is the same as Figure 5.12(b), but decomposed according to the cubic symmetry.

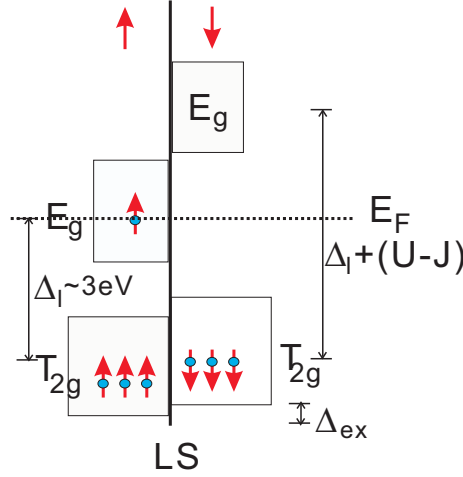


Figure 5.14: The LSDA+ U model DOS after the magnetic transition (LS-II).

compression, the magnetic moment of the high spin state decreases. The total energy of the HS state is the lowest until the volume reaches 60% of the equilibrium volume. Under further compression the low spin solution LS-II takes over. Because the low spin solution is metallic, the magnetic moment decreases to zero much faster than in the insulator. The transition pressure determined by the common tangent of the energy versus volume curves of the two cases is about 320 GPa. This pressure is much too high compared with the experiments. The pressure, however, is at least U dependent and we will discuss this later. The magnetic transition between HS and LS-II is a first order transition. The magnetic moment of Co jumps from $2.5\mu_B$ to $0.5\mu_B$ with a the volume collapse of about 6.5%.

5.7 The reason for the magnetic transition

Based on our calculation, the reason for the spin flip in CoO can be traced back to competitions between ligand field splitting and exchange interactions.

In the ligand field model, the spin state changes at the crossing point, i.e., the point at which Hund's first rule for the electronic ground state of the transition metal ion breaks down. The crossing point is given by

$$\Delta_l(V_c) = 2J, \quad (5.18)$$

where $\Delta_l(V_c)$ is the ligand field splitting between E_g and T_{2g} states at the critical volume V_c and J is the spin pair energy given by the Slater integrals. The ligand field splitting Δ_l increases as the volume is reduced because of the increasing interaction with the ligand anion, but J is less affected as it is an intra-atomic interaction.

Our self-consistent electronic structure calculation confirms the simple arguments above. The center of gravity (E_c) of a band is defined as

$$E_c = \frac{\int E D(E) dE}{\int D(E) dE}, \quad (5.19)$$

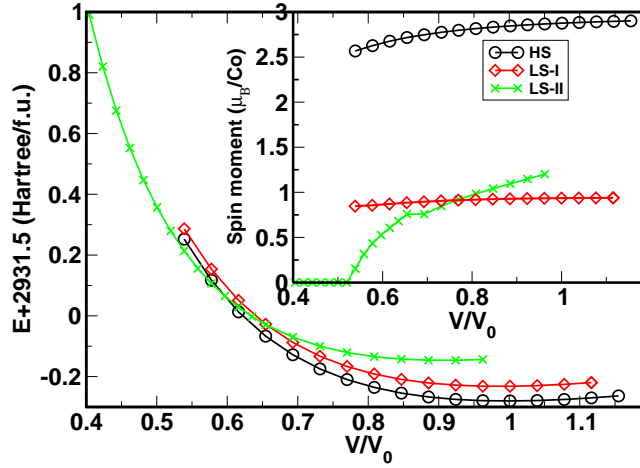


Figure 5.15: The total energy and the magnetic moment versus the relative volume with respect to $V_0=129.4$ a.u.. It can be seen that the low spin solution (LS-II) is energetic favorable under high pressures. The other low spin solution (LS-I) where the flip of the a_g electrons takes place is always above the curve of the high spin state.

where E is the energy and $D(E)$ is the related DOS. The center of gravity of the unoccupied E_g state ($E_c^{E_g}$ diamond lines) and T_{2g} state ($E_c^{T_{2g}}$ circle black line) are shown in Figure 5.16. It can be clearly observed that the splitting of the E_g and T_{2g} (cross red line) states is enlarged from ~ 1 eV to ~ 4 eV when the volume is shrunk to 50% while the average (the star red line) of the two is only slightly decreased. If we take $J = 1$ eV for Co, the 60% compression of the volume where the cross point appears in Figure 5.15 gives $\Delta_l = 3.1$ eV, satisfying the simple consideration $\Delta_l \geq 2J$ for the magnetic transition.

We notice that the PDOS in the range of $-3 \sim -1$ eV in our trigonal phase in Figure 5.11 is roughly split into two, namely $|m_l| = 2$ and $|m_l| = 1$. These states are the mixture of the cubic T_{2g} and E_g states. We note that the $e_{g,1}$ states have a larger portion of E_g , being $\frac{2}{3}E_g$ and only $\frac{1}{3}T_{2g}$. The E_g states in the cubic system have the strongest ($d\rho\sigma$) overlap with O ions, and thus are most affected by the pressure. So under pressure, the $e_{g,1}$ state flips its spin first. After self-consistency, the electrons are redistributed among the 3d shells resulting in the full occupation of T_{2g} state and the partial occupancy of the E_g state. This is favorable by the ligand field because the T_{2g} has the lower electrostatic interaction with the ligand O anion. The metallic solution comes from the strong overlapping of the orbitals, thus a wide band width under this large volume compression, although the unoccupied states and the occupied states are separated by $U - J$.

5.8 Discussions

In our calculation, the LSDA+ U is used, with $U=5$ eV given *ad hoc*. We choose U so as to reproduce the experimental results under ambient pressure, especially the lattice constant, the bulk modulus and the optical gap, reasonably well. This

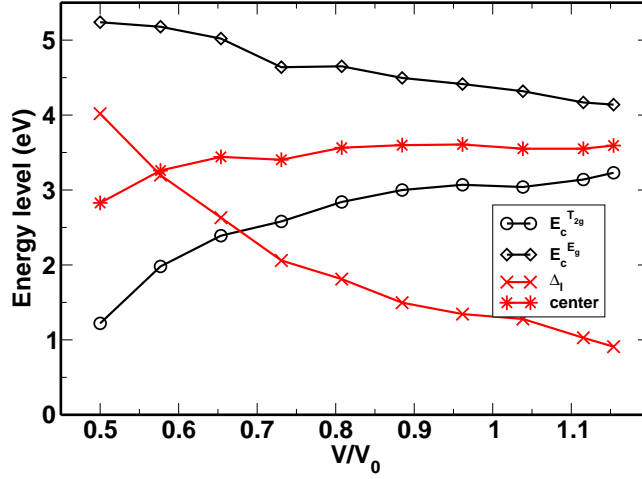


Figure 5.16: The evolution of the center of gravity of the unoccupied E_g state (diamonds) and T_{2g} state (circles) under relative volumes with respect to $V_0=129.4$ a.u./f.u.. The split of the two states Δ_l is shown by the crosses, while the average of them are shown by the stars. The lines are for guiding eyes.

U is also used when we apply high pressures. Although under high pressure, the occupation fluctuation effect will be enhanced, so that the U should not be the same, but the pressure dependence of U is not readily available. Our main results, the spin flip process, or the low spin configuration is not changed for different values of U . For example, we have results for $U=3, 5, 7.8$ eV. The self-consistent calculations give the same low spin state $T_{2g}^6 E_g^1$, but U is essential to stabilize the low spin solution. If we switch off the U , the solutions can only be reduced to LSDA nonmagnetic case, no matter what the initial density is. The transition pressure will be changed for different values of U of course because on one hand the energy versus volume curve is largely dependent on U . On the other hand also the position of the unoccupied states is largely dependent on U , so that the relative positions of the highest occupied states of the up spins and the lowest unoccupied down spin state is dependent on U . The gap is approximately $(U - J + \Delta_{ex} - \Delta_l)$, cf. Figure 5.9. At least from these two aspects, the value of U will influence the transition pressure. In Figure 5.17 the enthalpy variations with pressure of different states obtained by different values of U are shown. The transition pressure is reduced from 680 GPa to 130 GPa if U is decreased from 7.8 eV to 3 eV. We see that $U=3$ eV tunes the transition pressure to the vicinity of the experimental one (140 GPa in Figure 5.1).

In our calculation, no lattice distortion is taken into account. Experimentally, distortions are found both below the Néel temperature and under high pressures. Our calculations with the experimental distortions but without U does not give the insulating solutions which means that CoO is indeed not a band insulator. This distortion does not alter the electronic structure qualitatively if we compare the DOS from both. So we neglect the distortions when we discuss the spin flip processes.

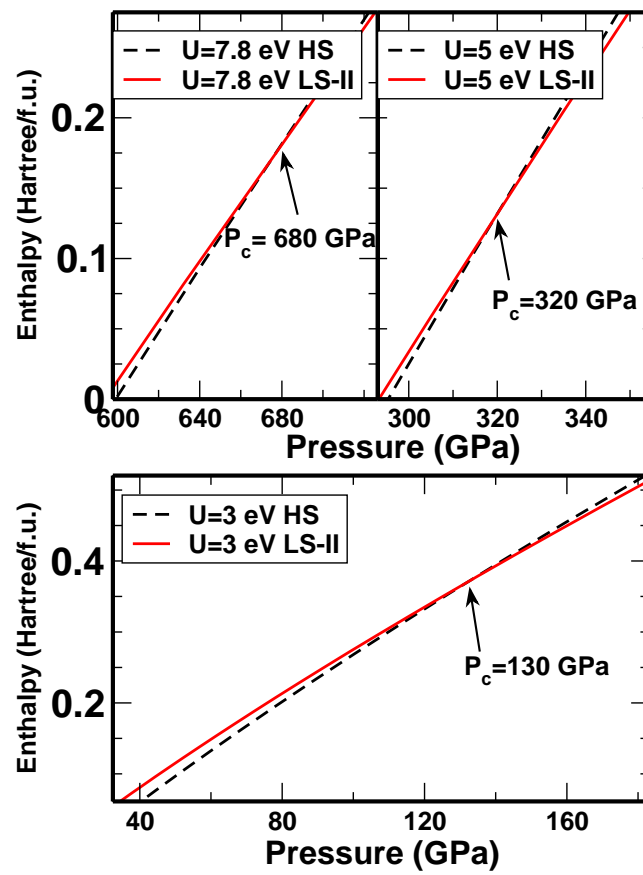


Figure 5.17: The enthalpy of CoO under pressure with different values of U . The point where the two lines cross is denoted by P_c . This is the pressure at which the magnetic transition happens.

Chapter 6

Summary and Outlook

In this thesis three kinds of compounds are investigated by density functional calculations in local spin density approximation.

The first one is the Heusler compound Rh_2MnGe . It is found that the cubic phase is not stable at $T = 0$. It may undergo tetragonal distortions by either extending or compressing the lattice in one direction. The electronic reason for this distortion is identified to be the band Jahn-Teller effect. The Jahn-Teller active states are found to be the 4d states of Rh placed at the Fermi level due to magnetic polarization. The tetragonal lattice distortion is clearly observed by recent low temperature XRD measurements. The phase transition from the high temperature cubic phase to lower temperature tetragonal phase is of second order, where the order parameter ($c/a - \sqrt{2}$) increases continuously from zero when the temperature is reduced below 180 K. However, the c/a ratio is much smaller from the experiment than our prediction. The reason may be a small LSDA error or disorder effects in experiments. In the proposed band Jahn-Teller scenario, the amount of energy that can be gained by the distortion is largely dependent on the height of the van Hove singularity near the Fermi level. Disorder will suppress the singularity, as well as the finite temperature in the experiments. Thus, the distortion is reduced. Improvement of the quality of samples of Rh_2MnGe is favorable to decrease the gap between theory and experiments. Up to now, we have only the frozen phonon calculation. What does the phonon dispersions in this compound look like? This will be done and after that, a more complete discussion about thermodynamics of structural phase transitions can be made.

The second kind consists of series of isostructural compounds in the cubic Laves phase: YFe_2 , ZrFe_2 , HfFe_2 , and LuFe_2 . The magnetic moment is found to decrease when the lattice constant is decreased, and finally disappears in all of these four compounds. Particularly, there exists a lattice constant range where the magnetic moment is rapidly reduced by decreasing the lattice constant. The magnetic moment behavior when approaching zero is categorized into first order (in ZrFe_2) and second order (in YFe_2 , HfFe_2 , and LuFe_2) phase transition. The difference is explained by the difference of the topology of DOS near the Fermi level and Landau's expansion of magnetic free energy. As shown by our calculation, the magnetism is suppressed under high pressures. The Invar anomaly in two of these compounds (ZrFe_2 and LuFe_2) is discussed, which show a high spin-low spin transition close to ambient pressure. As one of the major properties of

Invar alloys, the spontaneous volume magnetostriction (ω_s) is calculated and it is found to be comparable with the experiments. The compounds show different moment-volume behavior as compared with typical Invar alloy. In typical Invar alloy such as Fe_3Ni , there are double wells of HS and LS state in the binding curves, but in our Laves phase compounds a continuous transition from HS to LS is obtained. The lattice constant at which the transition takes place excludes the other two (YFe_2 and HfFe_2) from being Invar alloy. In the Laves phase compounds, the magnetic structure may be complicated due to the geometrically highly frustrated Fe sublattice. Especially when the magnetic moment is not ferromagnetically coupled, noncollinear magnetic moment arrangement is expected. Simulation of possible noncollinear magnetism in these compounds may improve our understanding of the properties, especially the Invar anomaly in these compounds.

Substitution of Zr by Fe in ZrFe_2 results in the decrease of the lattice constant and increase of the average magnetic moment per iron atom. The doped Fe takes the Zr site, and shows strong ferromagnetism, which is the reason for the increase of the average magnetic moment. The original problem of the homogenous region of Fe substitutions are going to be investigated theoretically.

At last the HS-LS transition under pressure in CoO is investigated by LSDA+ U . The collapse of the magnetic moment is discerned to be caused by the increase of the ligand field splitting under pressure. This increase of the ligand field splitting not only suppresses the intraatomic exchange, but also pushes the upper Hubbard band downwards (the band gap is decreased). This transition is of no surprise as it results from the competition between the ligand field split and the spin pairing energy. The results give a microscopic picture of the magnetic transition under the approximation of LSDA+ U . We obtained the metallic low spin state, which is in quite good agreement with recent experiments. The LSDA+ U , however, shows some uncertainty in the transition region from a strongly correlated system to a weakly correlated system under ultrahigh pressure, because the pressure dependent U is not available *ab initio*. This transition region is notoriously difficult in theory. Another parameter J , which enters the LSDA+ U , will have influence on the exchange energy. This parameter will surely influence the transition and the low spin solution. The effect will be investigated. How will other treatment of the correlation effect affect the HS-LS transitions? This point can be checked.

The interplay between structure and magnetism produces various states in itinerant systems as well as in strongly correlated systems. DFT calculations provide a way to understand the physics underlying them. In this thesis, only three interesting systems were investigated. Preliminary results show that the behavior can be explained by LSDA+(U). Investigations can be extended to the problems as mentioned above.

Bibliography

- [1] O. Madelung. *Introduction to Solid-State Theory*. Springer-Verlag, Reprinted by Beijing World Publishing Corporation, 2003.
- [2] H. Eschrig. *The Fundamentals of Density Functional Theory (2nd Edition)*. Edition am Gutenbergplatz Leipzig, 2003.
- [3] P. Hohenberg and W. Kohn. Inhomogeneous Electron Gas. *Phys. Rev.*, 136(3B):B864–B871, Nov. 1964.
- [4] E. H. Lieb. Density Functionals for Coulomb Systems. *Int. J. of Quant. Chem.*, 24(3):243–277, Mar. 1983.
- [5] W. Kohn and L. J. Sham. Self-Consistent Equations Including Exchange and Correlation Effects. *Phys. Rev.*, 140(4A):A1133–A1138, Nov 1965.
- [6] D. M. Ceperley and B. J. Alder. Ground State of the Electron Gas by a Stochastic Method. *Phys. Rev. Lett.*, 45(7):566–569, Aug. 1980.
- [7] John P. Perdew and Y. Wang. Accurate and Simple Analytic Representation of the Electron-gas Correlation Energy. *Phys. Rev. B*, 45(23):13244–13249, Jun. 1992.
- [8] K. Koepnik and H. Eschrig. Full-potential Nonorthogonal Local-orbital Minimum-basis Band-structure Scheme. *Phys. Rev. B*, 59(3):1743–1757, Jan. 1999.
- [9] N. W. Ashcroft and N. D. Mermin. *Solid State Physics*. Thomson Learning, Inc., reprinted by Beijing World Publishing Corporation, 1976.
- [10] E. C. Stoner. Collective Electron Ferromagnetism. *Proc. Roy. Soc. Lond. Series A*, 165(922):372–414, Apr. 1938.
- [11] H. Eschrig. Lecture notes on electronic structure of solid. unpublished, 2006.
- [12] V. L. Moruzzi. Singular Volume Dependence of Transition-Metal Magnetism. *Phys. Rev. Lett.*, 57(17):2211–2214, Oct. 1986.
- [13] D.-K. Seo. Density Functional Perturbational Orbital Theory of Spin Polarization in Electronic Systems. I. Formalism. *J. Chem. Phys.*, 125(15):154105, 2006.
- [14] G. Stollhoff, Andrzej M. Oleś, and V. Heine. Stoner Exchange Interaction in Transition Metals. *Phys. Rev. B*, 41(10):7028–7041, Apr. 1990.

- [15] H. A. Jahn and E. Teller. Stability of Polyatomic Molecules in Degenerate Electronic States. I. Orbital Degeneracy . *Proc. R. Soc. London A*, 161(905):220–235, Jul. 1937.
- [16] Sir R. Peierls. *Selected scientific Papers of Sir Rudolf Peierls with Commentary*, volume 19. World Scientific, 1997.
- [17] S. Lee and R. Hoffmann. Bcc and Fcc Transition Metals and Alloys: A Central Role for the Jahn-Teller Effect in Explaining Their Ideal and Distorted Structures. *J. Am. Chem. Soc.*, 124(17):4811–4823, Apr. 2002.
- [18] A. Ayuela, J. Enkvaara, K. Ullakko, and R.M. Nieminen. Structural properties of magnetic Heusler alloys. *J.Phys.: Cond. Matt.*, 11:2017–2026, 1999.
- [19] C. Bungaro, K. M. Rabe, and A. Dal Corso. First-Principles Study of Lattice Instabilities in Ferromagnetic Ni_2MnGa . *Phys. Rev. B*, 68(13):134104, Oct. 2003.
- [20] P. Dowben. Half Metallic Ferromagnets. *J. Phys.: Cond. Matt.*, 19(31):310301(1p), 2007.
- [21] F. A. Hames and J. Crangle. Ferromagnetism in Heusler-Type Alloys Based on Platinum-Group or Palladium-Group Metals. *J. Appl. Phys.*, 42(4):1336–1338, 1971.
- [22] J. C. Suits. New magnetic compounds with Heusler and Heusler-related structures. *Phys. Rev. B*, 14(9):4131–4135, 1976.
- [23] R.A. Dunlap, S. Jha, and G.M. Julian. Sn hyperfine field systematics in Rh_2MnZ Heusler alloys. *Can. J. Phys.*, 62:396–399, 1984.
- [24] M. Pugacheva and A. Jezierski. Dependence of the Magnetic Moment on the Local Atomic Order in Rh_2MnX Heusler Alloys . *J. Magn. Magn. Mat.*, 151:202–206, 1995.
- [25] I. Galanakis, P. H. Dederichs, and N. Papanikolaou. Slater-Pauling Behavior and Origin of the Half-metallicity of the Full-Heusler Alloys. *Phys. Rev. B*, 66(17):174429, Nov 2002.
- [26] Y. Adachi, H. Morita, T. Kanomata, A. Sato, H. Yoshida, T. Kaneko, and H. Nishihara. Pressure Effect on the Curie Temperature of the Heusler Alloys Rh_2MnZ ($\text{Z}=\text{Sn}, \text{Ge}$) . *J. Alloy. Comp.*, 383:37–39, 2004.
- [27] A. T. Zayak, P. Entel, K. M. Rabe, W. A. Adeagbo, and M. Acet. Anomalous Vibrational Effects in Nonmagnetic and Magnetic Heusler Alloys. *Phys. Rev. B*, 72(5):054113, 2005.
- [28] J. Kübler, A. R. Williams, and C.B. Sommers. Formation and Coupling of Magnetic Moments in Heusler Alloys. *Phys. Rev.B*, 28:1745–1755, 1983.
- [29] S. Fujii, S. Ishida, and S. Asano. Electronic Structure and Lattice Transformation in Ni_2MnGa and Co_2MnSn . *J. Phys. Soc. Jap.*, 58:3657–3665, 1989.

- [30] Z. Manuel. Aufklärung magnetisch und thermisch induzierter Strukturänderungen mittels Röntgenmethoden. Master's thesis, Technische Universität Dresden, 2007.
- [31] M. Shiga, Y. Muraoka, and Y. Nakamura. Invar Effects of Laves Phase Intermetallic Compounds . *J. Magn. Magn. Mat.*, 10:280–287, 1979.
- [32] M. P. Pasternak, R. D. Taylor, R. Jeanloz, X. Li, J. H. Nguyen, and C. A. McCammon. High Pressure Collapse of Magnetism in $\text{Fe}_{0.94}\text{O}$: Mössbauer Spectroscopy Beyond 100 GPa. *Phys. Rev. Lett.*, 79(25):5046–5049, Dec. 1997.
- [33] E. Duman, M. Acet, and E.F. Wassermann *et al.* Magnetic Instabilities in Fe_3C Cementite Particles Observed with Fe K -edge X-ray Circular Dichroism Under Pressure . *Phys. Rev. Lett.*, 94:075502, 2005.
- [34] I. A. Troyan, A. G. Gavrilyuk, and V. A. Sarkisyan *et al.* Transition from the Antiferromagnetic to a Nonmagnetic State in FeBO_3 under High Pressure. *JETP Letters*, 74:24–27, 2001.
- [35] G. Wortmann, K. Rupprecht, and H. Giefers. High-pressure Studies of Magnetism and Lattice Dynamics by Nuclear Resonant Scattering of Synchrotron Radiation. *Hyperfine interactions*, 114/115:103–117, 2002.
- [36] T. Dumelow, P. C. Riedi, P. Mohn, K. Schwarz, and Y. Yamada. Pressure Dependence of the Hyperfine Field of YFe_2 and ZrFe_2 . *J. Magn. Magn. Mater.*, 54-57:1081–1082, 1986.
- [37] P. C. Riedi and G. D. Webber. Pressure and Temperature Dependence of the Hyperfine Fields of YFe_2 , YFe_3 and YIG. *J. Phys. F: Metal Phys.*, 13(5):1057–1069, 1983.
- [38] K. Kai and T. Nakamichi. Magnetic Moment of the Iron Atom in the Laves Phase Compounds. *J. Phys. Soc. Japan*, 30:1755, 1971.
- [39] J. G. M. Armitage, T. Dumelow, R. H. Mitchell, P. C. Riedi, J. S. Abell, P. Mohn, and K. Schwarz. Pressure Dependence of the Magnetisation of YFe_2 and ZrFe_2 : Computation and Experiment. *J. Phys. F: Metal Phys.*, 16(7):L141–L144, 1986.
- [40] M. Brouha and K. H. J. Buschow. Pressure Dependence of the Curie Temperature of Intermetallic Compounds of Iron and Rare-earth Elements, Th, and Zr. *J. Appl. Phys.*, 44(4):1813–1816, 1973.
- [41] S. Asano and S. Ishida. Competition of Magnetism in Iron Laves Phase Compounds. *J. Phys.: Cond. Matt.*, 1(44):8501–8508, 1989.
- [42] H. Yamada and M Shimizu. Electronic Structure and Magnetic Properties of the Cubic Laves Phase Transition Metal Compounds . *Physica B*, 149:390–402, 1988.
- [43] B.M. Klein, W.E. Pickett, D.A. Papaconstantopoulos, and L.L. Boyer. Electronic Structure, Superconductivity, and Magnetism in the C15 Compounds ZrV_2 , ZrFe_2 , and ZrCo_2 . *Phys. Rev. B*, 27:6721–6731, 1982.

- [44] P. Mohn and K. Schwarz. Binding Mechanism and Itinerant Magnetism of ZrFe_2 and YFe_2 . *Physica*, 130B:26–28, 1985.
- [45] M. S. S. Brooks, O. Eriksson, and B. Johansson. 3d-5d Band Magnetism in Rare Earth Transition Metal Intermetallics: LuFe_2 . *J. Phys.: Cond. Matt.*, 1(34):5861–5874, 1989.
- [46] C. Ritter. Polarised Neutron Study of Magnetic Ordering in the Simple Alloy YF_2 . *J. Phys.: Cond. Matt.*, 01:2765–2769, 1989.
- [47] V. Heine. $s - d$ Interaction in Transition Metals. *Phys. Rev.*, 153(3):673–682, Jan. 1967.
- [48] K Schwarz and P Mohn. Itinerant Metamagnetism in YCo_2 . *J. Phys. F: Metal Physics*, 14(7):L129–L134, 1984.
- [49] J. Kübler. *Theory of Itinerant Electron Magnetism*. Oxford science publications, 2000.
- [50] Roy L. Johnston and R. Hoffmann. Structure-bonding Relationships in the Laves Phases. *Z. Anorg. Allg. Chem.*, 616:105–120, 1992.
- [51] M. Isoda and S. Mori. Magnetic Correlation and Breakdown of Fermi Liquid Picture in Frustrated Itinerant Electron Magnet. *J. Phys. Soc. Japan*, 69(5):1509–1516, 2000.
- [52] Walter. A. Harrison. *Elementary Electronic Structure (Revised Edition)*. World Scientific, 2004.
- [53] David R. Lide (editor-in chief). *CRC handbook of chemistry and physics, 84th edition*. CRC Press, 2003.
- [54] J. Mathon. Pressure Dependence of the Magnetization in the Itinerant Electron Model of Ferromagnetism. *J. Phys. F: Metal Phys.*, 2(1):159–168, 1972.
- [55] R. Coehoorn. Calculated Electronic Structure And Magnetic Properties of Y-Fe Compounds. *Phys. Rev. B*, 39(18):13072–13085, Jun 1989.
- [56] Wasserman. *Ferromagnetic Materials, a Handbook on the Properties of Magnetically Ordered Substances, edited by K.H.J. Buschow and E.P. Wohlfarth*, volume 5. Elsevier Science Publishers, 1990.
- [57] Y. Amako, H. Nagai, Yokoyama T., Yamada H., and Naka T. *et al.* Pressure Dependence of the Curie Temperature and the Spontaneous Magnetization in Ferromagnetic $\text{Hf}(\text{Fe}, \text{Co})_2$. *Physica B*, 382(1-2):189–192, June 2006.
- [58] C. Pfleiderer. Why First Order Quantum Phase Transitions Are Interesting. *J. Phys.: Cond. Matt.*, 17(11):S987–S997, 2005.
- [59] M. Shimizu. On the Conditions of Ferromagnetism by the Band Model: II. *Proc. Phys. Soc.*, 86:147–157, 1965.
- [60] R. J. Weiss. The Origin of the ‘Invar’ Effect. *Proc. Phys. Soc.*, 82(2):281–288, 1963.

- [61] V. L. Moruzzi. High-spin and Low-spin States in Invar and Related Alloys. *Phys. Rev. B*, 41(10):6939–6946, Apr. 1990.
- [62] P. Entel, E. Hoffmann, P. Mohn, K. Schwarz, and V. L. Moruzzi. First-principles Calculations of the Instability Leading to the Invar Effect. *Phys. Rev. B*, 47(14):8706–8720, Apr. 1993.
- [63] M. van Schilfgaarde, I.A. Abrikosov, and B. Johansson. Origin of the Invar Effect in Iron-nickel Alloys. *Nature*, 400:46–49, Jul. 1999.
- [64] V. Crisan, P. Entel, H. Ebert, H. Akai, D. D. Johnson, and J. B. Staunton. Magnetochemical Origin for Invar Anomalies in Iron-nickel Alloys. *Phys. Rev. B*, 66(1):014416, Jul. 2002.
- [65] S. Khmelevskiy, I. Turek, and P. Mohn. Large Negative Magnetic Contribution to the Thermal Expansion in Iron-Platinum Alloys: Quantitative Theory of the Invar Effect. *Phys. Rev. Lett.*, 91(3):037201, Jul. 2003.
- [66] N. Mattern, W. X. Zhang, S. Roth, H. Reuther, C. Baetz, and M. Richter. Structural and magnetic properties of non-stoichiometric Fe_2Zr . *J. Phys.: Cond. Matt.*, 19(37):376202 (8pp), 2007.
- [67] K. Koepnik, B. Velický, R. Hayn, and H. Eschrig. Self-consistent LCAO-CPA Method for Disordered Alloys. *Phys. Rev. B*, 55(9):5717–5729, Mar. 1997.
- [68] V. I. Anisimov, F. Aryasetiawan, and A. I. Lichtenstein. First-principles Calculations of the Electronic Structure and Spectra of Strongly Correlated Systems: the LDA+U method. *J. Phys.: Cond. Matt.*, 9(4):767–808, 1997.
- [69] Z. Fang, I. V. Solovyev, H. Sawada, and K. Terakura. First-principles Study on Electronic Structures and Phase Stability of MnO and FeO under High Pressure. *Phys. Rev. B*, 59(2):762–774, Jan. 1999.
- [70] D. Kasinathan, K. Koepnik, and W. E. Pickett. Pressure-driven magnetic moment collapse in the ground state of MnO. *New J. Phys.*, 9(7):235, 2007.
- [71] D. Kasinathan, J. Kunes, K. Koepnik, C. V. Diaconu, R. L. Martin, I. D. Prodan, G. E. Scuseria, N. Spaldin, L. Petit, T. C. Schulthess, and W. E. Pickett. Mott Transition of MnO under Pressure: A Comparison of Correlated Band Theories. *Phys. Rev. B*, 74(19):195110, 2006.
- [72] D. Yang, R. Yang, C. Paul, J. Zhang, S. C. Vogel, B. Winkler, J. Xu, Y. Zhao, and H.-K. Mao. Pressure-induced Long-range Magnetic Ordering in Cobalt Oxide. *Phys. Rev. B*, 74(14):144101, 2006.
- [73] Q.Z. Guo, H.-K. Mao, J.Z. Hu, J.F. Shu, and R. J. Hemley. The Phase Transitions of CoO under Static Pressure to 104 GPa. *J. Phys.: Cond. Matt.*, 14(44):11369–11374, 2002.
- [74] J-P Rueff, A. Mattila, J. Badro, G. Vankó, and A. Shukla. Electronic Properties of Transition-metal Oxides under High Pressure Revealed by X-ray Emission Spectroscopy. *J. Phys.: Cond. Matt.*, 17(11):S717–S726, 2005.

-
- [75] T. Atou, M. Kawasaki, and S. Nakajima. Electronic Transition of Cobalt Monoxide under High-Pressure. *Jap. J. Appl. Phys.*, 43(10A):L1281–L1283, 2004.
- [76] K. Tomiyasu, T. Inami, and N. Ikeda. Magnetic Structure of CoO Studied by Neutron and Synchrotron X-Ray Diffraction. *Phys. Rev. B*, 70(18):184411, 2004.
- [77] V. I. Anisimov, J. Zaanen, and O. K. Andersen. Band Theory and Mott Insulators: Hubbard U Instead of Stoner I. *Phys. Rev. B*, 44(3):943–954, Jul. 1991.
- [78] U. D. Wdowik and K. Parlinski. Lattice Dynamics of CoO from First Principles. *Phys. Rev. B*, 75(10):104306, 2007.
- [79] F. Tran, P. Blaha, K. Schwarz, and P. Novak. Hybrid Exchange-Correlation Energy Functionals for Strongly Correlated Electrons: Applications to Transition-Metal Monoxides. *Phys. Rev. B*, 74(15):155108, 2006.
- [80] R. E. Cohen, I. I. Mazin, and D. G. Isaak. Magnetic Collapse in Transition Metal Oxides at High Pressure: Implications for the Earth. *Science*, 275:654–657, 1997.
- [81] V. I. Anisimov, I. V. Solovyev, M. A. Korotin, M. T. Czyżyk, and G. A. Sawatzky. Density-functional Theory and NiO Photoemission Spectra. *Phys. Rev. B*, 48(23):16929–16934, Dec. 1993.
- [82] M. T. Czyżyk and G. A. Sawatzky. Local-density Functional and On-Site Correlations: the Electronic Structure of La_2CuO_4 and $LaCuO_3$. *Phys. Rev. B*, 49(20):14211–14228, May 1994.
- [83] H. Eschrig, K. Koepnick, and I. Chaplyginne. Density Functional Application to Strongly Correlated Electron Systems. *J. of Solid State Chem.*, 176(2):482–495, Dec. 2003.
- [84] H. Gebhard. *The Mott Metal-Insulator Transition: Models and Methods*. Springer-Verlag Berlin Heidelberg, 1997.
- [85] M. Imada, A. Fujimori, and Y. Tokura. Metal-insulator transitions. *Rev. Mod. Phys.*, 70(4):1039–1263, Oct. 1998.
- [86] K. Terakura, A. R. Williams, T. Oguchi, and J. Kübler. Transition-Metal Monoxides: Band or Mott Insulators. *Phys. Rev. Lett.*, 52(20):1830–1833, May. 1984.
- [87] M. R. Norman. Orbital Polarization and the Insulating Gap in the Transition-Metal Oxides. *Phys. Rev. Lett.*, 64(10):1162–1165, Mar. 1990.
- [88] S. Ohnishi. A Theory of the Pressure-Induced High-Spin-Low-Spin Transition of Transition Metal Oxides. *Phys. Earth and Plan. Inter.*, 17(2):130–139, Sep. 1978.
- [89] P. Werner and A. J. Millis. High-spin to Low-Spin And Orbital Polarization Transitions in Mutiorbital Mott Systems. *Phys. Rev. Lett.*, 99(12):126405, Sept. 2007.

-
- [90] F. Birch. Finite Strain Isotherm and Velocities for Single-crystal and Polycrystalline NaCl at High Pressures and 300 K. *J. Geophys. Res.*, 83(B3):1257–1268, 1978.
- [91] Z.-X. Shen, C. K. Shih, O. Jepsen, W. E. Spicer, I. Lindau, and J. W. Allen. Aspects of the Correlation Effects, Antiferromagnetic Order, and Translational Symmetry of the Electronic Structure of NiO and CoO. *Phys. Rev. Lett.*, 64(20):2442–2445, May. 1990.
- [92] M. Magnuson, S. M. Butorin, J.-H. Guo, and J. Nordgren. Electronic Structure Investigation of CoO By Means of Soft X-Ray Scattering. *Phys. Rev. B*, 65(20):205106, Apr. 2002.
- [93] M. A. Korotin, S. Yu. Ezhov, I. V. Solovyev, V. I. Anisimov, D. I. Khomskii, and G. A. Sawatzky. Intermediate-spin State and Properties of LaCoO₃. *Phys. Rev. B*, 54(8):5309–5316, Aug 1996.

Appendix

The real spherical harmonics¹

The spherical harmonics of various authors differ by constant phase factors. We use the definition of

$$\begin{aligned} \mathcal{Y}_{lm}(\zeta, \varphi) = i^l \sqrt{\frac{2l+1}{4}} \frac{(-1)^{(|m|+m)/2} e^{im\varphi}}{\sqrt{(l+|m|)!(l-|m|)!}} (1-\zeta^2)^{|m|/2} \theta^{1-|m|} \\ * \sum_{p=0,2,\dots}^{l-|m|} \frac{(-1)^{p/2} (l-|m|)!(2l-1-p)!!}{(l-|m|-p)!p!} \zeta^{-p}, \end{aligned} \quad (6.1)$$

with $\zeta = z/r$, $\varphi = \arctan(y/x)$, $0 \leq \varphi \leq 2\pi$. The “real” spherical harmonics is defined by

$$Y_{lm} = \begin{cases} \frac{i}{\sqrt{2}}(\mathcal{Y}_{l-|m|} - (-1)^m \mathcal{Y}_{l-|m|}) & < \\ \mathcal{Y}_{l0} & = 0 \\ \frac{1}{\sqrt{2}}(\mathcal{Y}_{l-|m|} + (-1)^m \mathcal{Y}_{l-|m|}) & > \end{cases} \quad \text{for } m \quad (6.2)$$

The first harmonics in Equ. (6.2) are

$$\begin{aligned} Y_{00} &= \frac{1}{\sqrt{4\pi}}, \\ Y_{1-1} &= i\sqrt{\frac{3}{4\pi}} \frac{y}{r}, \quad Y_{10} = i\sqrt{\frac{3}{4\pi}} \frac{z}{r}, \quad Y_{11} = i\sqrt{\frac{3}{4\pi}} \frac{x}{r}, \\ Y_{2-2} &= -\sqrt{\frac{15}{4\pi}} \frac{xy}{r^2}, \quad Y_{2-1} = -\sqrt{\frac{15}{4\pi}} \frac{yz}{r^2}, \quad Y_{20} = -\sqrt{\frac{5}{16\pi}} (3\frac{z^2}{r^2} - 1), \\ Y_{21} &= -\sqrt{\frac{15}{4\pi}} \frac{xz}{r^2}, \quad Y_{22} = -\sqrt{\frac{15}{16\pi}} \frac{(x^2 - y^2)}{r^2}, \end{aligned}$$

¹H. Eschrig, *Optimized LCAO Method*, Akademie-Verlag Berlin 1989

Acknowledgment

At this point, I want to thank everyone who accompanied me during the last three years. During these three years, I have experienced a “second order” transition from doing experiments to doing theory. The driving force behind this transition is my personal interests in understanding something theoretically. A lot of people help me to survive this process and I would like to express my thanks to these loving people.

First I would like to thank my supervisor, Prof. Dr. Helmut Eschrig. I first thank him for setting up for me a model how a scientist should be like. In his words, “A scientist lives on his reputation”. His lectures are always enlightening. He carefully explained how a formula is understood by physical arguments, and at the same time, how physical ideas are formulated with mathematical precision.

The second thanks are given to my second supervisor PD. Dr. Manuel Richter. I thank him for all the helps, both scientific and nonscientific, during my stay in Dresden. I thank him for his very careful correction of my thesis, and a lot of critical suggestions of the physical ideas. He also corrected me some naïve, or sometimes error explanations of some results. His suggestions can always improve the quality of the thesis. His instructive, and impressive drawings always help me to understand complicate phenomena.

Special thanks are given to my cooperators: Mr. Z. Manuel at TU Dresden, and Mr. S. Nils at IFW for the experimental work on Rh_2MnGe , and Dr. N. Mattern at IFW for introducing me the Zr-Fe compounds and cooperations on the nonstoichiometric compounds.

Many thanks go to my dear colleagues in our theoretical group. Dr. Klaus Koepernick is always ready to answer any questions about FPLO. You are the fastest person in thinking and computing I have ever met. Ulrike Nitzsche is always willing to help on any problems about our workhorses, the clusters. Of course, discussions with Dr. Michael Kuzmin, Dr. Ingo Opahle, Dr. Ferenc Tasnadi, and Dr. Mahdi Sargolzaei are always helpful. I will also thank my German colleagues, Casten Neise, Stephan Schönecker and Mathias Beyer for providing my a lot of fun during the work. All my Chinese friends and colleagues in Dresden, especially Hongbin Zhang, Prof. Dr. Weimin Wang, Prof. Dr. Chongde Cao are acknowledged. It is you who make the study and work here much more harmonic. I cannot make a full list of the people should be thanked. Here I just mentioned several of them: PD. Dr. Anulf Möbius, Dr. Saad El Gazar, Maengsuk Kim, *etc.*

I would also like to take this opportunity to acknowledge my colleagues in China: Associate Prof. Wanli Zhang, Prof. Dr. Huaiwu Zhang, Prof. Dr. Shiqing Yang, Associate Prof. Dr. Hongchuan Jiang, Dr. Bin Peng, and Mr.

Rujun Tang, *et al.* for all their supports when I was in Dresden. Without your continuous support and help, I do not think that I can finish my thesis.

The last but not the least thanks go to my family. My wife, and dear parents take good care of the family when I am abroad. They always favor my decisions and encourage me. I hope my little lovely daughter, Lele, will excuse me for not being able to accompany her when she was young. As a father, I shall say that I am sorry. I will spend all my free time with you when I am back, my dear daughter.

Two years of financial support from Deutscher Akademischer Austausch Dienst (DAAD) is greatly acknowledged.

Versicherung

Hiermit versichere ich, dass ich die vorliegende Arbeit ohne unzulässige Hilfe Dritter und ohne Benutzung anderer als der angegebenen Hilfsmittel angefertigt habe; die aus fremden Quellen direkt oder indirekt übernommenen Gedanken sind als solche kenntlich gemacht. Die Arbeit wurde bisher weder im Inland noch im Ausland in gleicher oder ähnlicher Form einer anderen Prüfungsbehörde vorgelegt. Die Arbeit entstand mit wissenschaftlicher Betreuung durch Prof. Helmut Eschrig am Leibniz-Institut für Festkörper- und Werkstoffforschung Dresden.

Ich habe vorher kein anderes Promotionsverfahren eröffnet. Ich erkenne die Promotionsordnung der Fakultät Mathematik und Naturwissenschaften der Technischen Universität Dresden in der aktuell gültigen Fassung an.

Wenxu Zhang

Dresden, den 15. Nov. 2007

